LITHOLOGIC AND STRUCTURAL MAPPING OF NORTHEAST LAKE ZIWAY AREA, ETHIOPIAN RIFT USING LANDSAT DIGITAL DATA

A Thesis

Presented to the

School of Graduate Studies

Addis Ababa University

In Partial Fulfillment

of the Requirements for the Degree

Master of Science in Geology

by

Tesfaye Korme

September 1992

ABSTRACT

Studies of interactively enhanced Landsat thematic mapper (TM) imagery integrated with field survey and aerial-photo interpretations were carried out to map the lithology and structures of the study area located in the axial zone of the Main Ethiopian Rift. The Ethiopian Rift has been studied for decades using a variety of geological and geophysical techniques, but synoptic mapping of the lithology and structures and analysis of regional structural relationships have not been previously studied applying high resolution satellite digital data. By combining Landsat TM data with results from conventional method of geological mapping four major serieses of volcanic rocks have been identified, namely: 1. A lower series of pyroclastic deposits dominated by greyish green ignimbrite (Wedecha Series), 2. A basalt series of transitional to subalkaline basalts character (Anole Series), 3. Pyroclastic deposits of the Rift floor dominated by pumice and ash falls (Bora Series) and 4. Recent lava flows extruded through Wonji Fault Belt openings (Jano Series). In addition, four sets of structures were mapped: 1. Main marginal NE-SW striking normal faults, 2. E-W to NW-SE striking strike slip faults that have dextrally displaced the marginal faults, 3. NNW-SSE striking cross-rift lineaments and 4. the youngest and active NNE-SSW to N-S striking faults (Wonji Fault Belt). Using different techniques of enhancement most lithologic contacts and lineaments that had not been indicated in any existing geological and structural maps for the region were carefully mapped with better accuracy, minimum expense and shorter sorter field season. It has been observed that tectonism preceeds volcanism in time and the type of volcanic rocks assemblage and composition reflects the degree of rifting and intensity of tectonism that had initiated the volcanism.

C O N T E N T S

ILLUSTRATIONS

Page

I. List of Figures

II. List of Plates

III. List of Tables

ACKNOWLEDGMENTS

My thanks are due in the first place to Prof. Alberto Marini for his help in the field, as well as the petrographic and image processing laboratory works and Prof. Mauro Rosi for his help in petrographic identification and description of different types of volcanic rocks including their field relationships, and to Mrs. Neils (Univ. of Cagiliari) for her wise and patient assistance in further analyzing the digital data using advanced digital systems.

I am highly greatful to Prof. Getaneh Assefa (Head of the Department) who curiously followed the progress of the thesis work from the beginning to the final reading of the thesis. I also acknowledge Dr. Tilahun Mamo, Dr. Gezahegn Yirgu and W/t Aster Abebe for reading and constructively commenting the thesis.

I gratefully acknowledge the help given to me by Ato Tamiru and W/o Meaza from the Ethiopian Mapping Authority Department of Remote Sensing, and Ato Samson Tesfaye from Ethiopian Institute of Geological Survey, Regional Mapping Department for their technical assistance and advice while processing and interpreting the images. My acknowledgment also goes to Ato Alula Damte for his constructive comments on the lineaments and geological maps; Balemual Atnafu , Dereje Ayalew and Teshome Korme for general help they provided in

moulding the final shape of the thesis.

Finally I am highly indebted to the German Academic Exchange Service (DAAD) which has given part of the financial support for the very important expenses of the thesis work and Mrs Begel (the vice chancellor of the German Embassy in Ethiopia) for her patience and politeness in facilitatinig the long bureaucratic trend in receiving the in-country scholarship and research allowance.

1. INTRODUCTION

A large part of the vast and resourceful land of Ethiopia has remained geologically unexplored due to its rough topography ,climate, and other factors. To overcome some of these barriers and unravel the resource potential of the country the importance of mapping using Remote Sensing methods integrated with field survey is unquestionable. This work is, therefore, directed to apply the effectivness of the methods of Remote Sensing in mapping the lithology and structures of an inaccessible area located in the central part of the Main Ethiopian Rift with the aid of computer enhanced Landsat TM digital data analysis integrated with field survey and aerial-photo interpretation and comparing the methods and results with previous works.

Prior to the availability of satellite imageries, geologists relied on aerial photography to provide synoptic coverage of a study area. However, geologic interpretation of areial-photos is limitted by factors including poor spectral resolution, high geometrical distortion, limited scale to recognize large surface features and higher cost of flying over inaccessible areas. Landsat TM data partly avoids some of the drawbacks inherited to aerial-phtographs.

A number of image enhancements and transformations are performed on the TM imagery to improve the discriminability of geologic features using bands 2, 3, 4 and 5. Principal component analysis, band ratioing, filtering, classification, editing, geometric correction and rectification are the major image processing techniques applied to achieve the final results.

From this study, four major volcanic rock groups are revealed: 1. A lower series of pyroclastic deposits dominated by grey greenish ignimbrite (Wedecha Series), 2. A basalt series of transitional to subalkaline character (Anole Series), 3. Pyroclastic deposits of the Rift floor dominated by pumice and ash falls (Bora Series) and 4. Recent lava flows extruded through active rift faults and fissures (Jano Series). In addition, four sets of structures were mapped: 1. Main marginal NE-SW striking normal faults, 2. E-W to NW-SE striking strike slip faults that have dextrally displaced the marginal faults, 3. NNW-SSE striking cross-rift lineaments and 4. the youngest and active NNE-SSW to N-S striking faults (Wonji Fault Belt). Using different techniques of enhancement most lithologic contacts and lineaments that were not indicated in any existing geological and structural maps for the region are carefully mapped with better accuracy, minimum expense and shorter time. It has been noted that tectonism preceeds volcanism in time and the type of volcanic roks assembilage and composition reflects the stage of rifting and intensity of tectonism that had initiated the volcanism.

1.1. Location and Accessibility

The study area, covering about 125 sq.kms, lies within 38°45'-39°15'E. long.,and 8°00'-8°15'N.,lat (Figure 1.1). It is bounded to the east by the Nazreth-Asela and to the west by the Mojo-Ziway main roads. Its approximate location is 150km. SSE of Addis Ababa. The area is situated within the central sector of the main Ethiopian Rift characterized by active tectonism and related volcanism. This part of the Rift manifests faulted blocks with relatively steep scarps that form local horst-and-graben structures, and long and narrow open fissures, and cinder cones constituted the very rough topography. As a result the topography is rough and togethere with the hot and arid makes accessibility to some parts of the area rather difficult.

More than 40% of the area is almost not accessible neither by car nor on foot. Most of the area can be reached from two directions: from the east following the Addis Ababa-Nazreth-Asela and from the west Addis Ababa-Mojo-Awasa roads. Another dirt road that crosses the area runs from Kulumsa through Ogolcho to Meki. This road has been useful to arrive at important outcrop sections and passes through representative test areas for this study. Figure 1.1. shows location of the study area within the Main Ethiopian Rift .

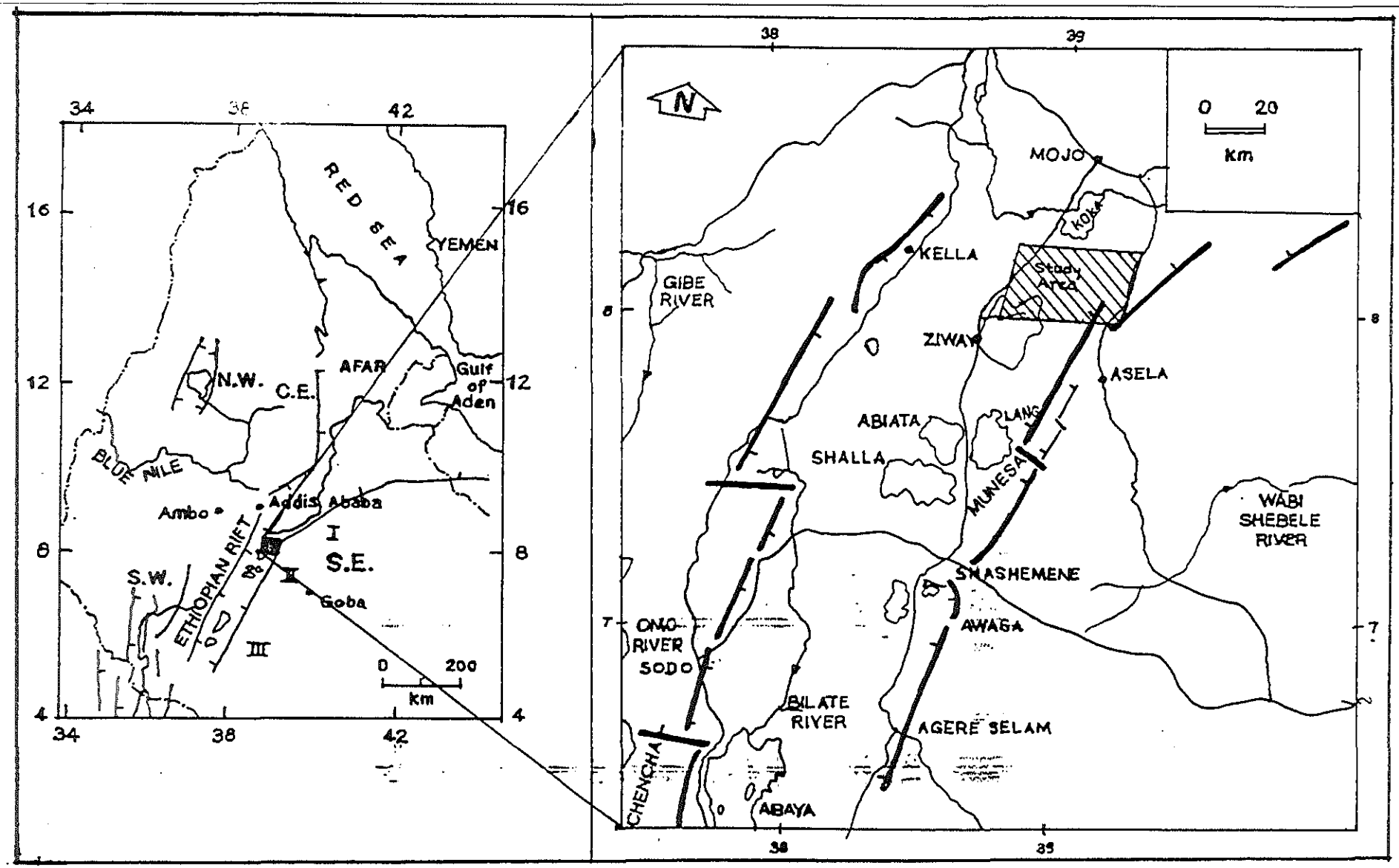

Fig.1.1 LOCATION MAP

1.2 Objectives

The objectives of the thesis project consist of two major intents:

1. The assessment of satellite digital data (TM) and digital image processing and classification for geological application in the study area.

2. The provision of geological information for the analysis of the regional studies.

Eventhough, many geological investigations have been made in studying the lithology and structures in the region using conventional methods, mapping with the aid of computer enhanced TM digital data integrated with field survey and aerial photography interpretation, and correlating the methods and results with previously produced maps is the first and primary objective of the research. Therefore, mapping the lithologies and structures in hostile and inaccssible parts of the region applying techniques of Remote Sensing, and reconstructing the possible inter-relationships among the major geological structures mainly lineaments in the rift from directionally filtered and enhanced TM images and finally, preparing geological and tectonic maps on a scale of 1:50,000 using computers, are the overall objectives of the research.

1.3. Previous Works

The area under study has rarely been included and mentioned in previous general geological studies; Geological descriptions of this area are found in the work of Mohr (1962; 1963; 1966; 1967; 1970), Di Paola (1972;1976), Juch (1975), Kazmin and Seife (1978), WeldeGabriel, Aronson, and Walter (1990). The Ethiopian Institute of Geological Surveys (EIGS) has also conducted general investigations in the western and northwestern part of the area before 1970, and recently the UNDP project for geothermal resource has produced a 1:50,000 geological map. Almost all geological investigations so far carried out in the region follow conventional methods of mapping except, Rothery and Seife (1987), Tesfaye (1988) and few other unpublished thesises which employed the method of interactive image processing for mapping the western Ethiopian Basement rocks and related geologic structures. Published reports on the study of soils and geomorphology on the basis of MSS band 5 and 7 interpretations are available at the Institute of Landuse and Planning. This thesis is the first of its kind for mapping the Ethiopian Rift structures and lithologies using computer enhanced Landsat TM digital data integrated with field observations.

1.4. Methods and Materials

Imagery processing was performed on an ERDAS based interactive digital image manipulation system at the Ethiopian Mapping Authority Regional center for Remote Sensing. Imagery analysis included contrast enhancement and filtration of individual TM bands and band ratioing, principal component analysis, false colour combination and both supervised and unsupervised classifications. Multivariate statistics were computed for the scene, providing correlation coefficients and comparison of spectral variance between bands.

Field work supported by conventional interpretation of aerial photographs was carried out in a number of selected areas to provide ground control for the TM data in supervised classification. The supervised classification, operating from the training samples selected over known rock units and structures, applies a maximum likelihood decision rule to all other pixels based on class covariance and mean vectors.

In the evaluation of sample statistics, several methods have been used to make sure that the selected samples are representatives of all the classes. Together with quick look and ellipse used to evaluate on the display and contigency matrix, statistics, divergent matrix, signature distance

(euclidiean) formed part of the activity at this stage.

Finally, the supervised and enhanced data were extrapolated to the remaining area under some controls from aerial-photo interpretation and field observations. Using film writer and tectronix ink jet colour printer, all images that provide best lithologic and structural informations and suitable for visual interpretation, are taken from the memory of the computer. The GIS image is simplified to geological map of the area at the scale of 1:50,000.

Materials and equipments used include:

i.Digital

-Digital data (landsat TM) acquired in 1989

-Digital image processing facility

-Hardware components

-Compaq desk pro-286 computer

-peripheral devices connected to the computer

-Magnetic tape reader

-Film writer

-Scanner

-Printers

-Software components

-ERDAS version 7.4

-Cipher menu

-Scanner

-QCR

ii. **Auxiliary Materials**

-Aerial photographs and mirror streoscops

-Topomaps of scale 1:50,000

-MSS band 4,5 and 7 analog images

-Thin-sections and mineralogical microscope

-Field equipments

-Slides and transparents

1.5. Climate and Vegetation

1.5.1. Climate

On the basis of the meteorological data collected from the mteorological stations at Ziway, Kulumsa and Awash Melkasa towns for 1989, the year in which the image was acquired, for rainfall, mean annual temperature and altitude, the study area is classified into three main climatic zones, namely 1. Temperate Zone (Woina Dega) with altitude between 1500-2300m.a.s.l, mean annual temperature between 18oc and 20° c. 2. Warm Zone (kola) altitude between 800-1,500m.a.s.l and mean annual temperature varies between 22° c to 26° c. 3.

Semi-Desert Zone (Kefil Bereha) less than 800m.a.s.l.in altitude and with temperature greater than 26.8c.

The Temperate (Woina Dega) zone includes most of the area north and northwest of the town of Asela following the step faults of the eastern rift escarpment. About 75% of the study area falls falls within this zone.

The Warm (Kola) zone includes the area located around lake Koka. It covers and constitutes only about 5% of the area.

The remaining 20% of the area falls under Semi-Desert (Kefil Berha) climatic zone. The semi-desert zone in the area lies between lake Ziway and the Awash river just before it enters lake Koka.

According to study of Tato (1970) and Mengistu (1975) there are only two seasons in the area; 1. the Rainy season, which is colder and with smaller mean monthly range of temperature and higher rainfall. 2. The Dry season. The rainy season extends from the beggining of June to the end of September, and is much shorter compared to the dry season. The rainy season becomes relatively longer with intensive rainfall toward the plateau especially mainly near Mount Chilalo where frost occurence is common in August.

The mean monthly rainfall and mean maximum and minimum temperature curves shown in fig.1.5a and 1.5b respectively, confirm the presence of only two major seasons in the area.

One of the most important meteorological factors to consider during image processing and interpretation is the number of hours of bright sunshine in a day. It helps to know the intensity of cloud coverage, the knowledge of which inturn enables one to correct for the error introduced by clouds and cloud shadows during image processing and interpretation. For the study area, the number of hours of bright sunshine in the year 1989 is shown in fig.1.5c. In this graph, it is indicated that November, December, and January have maximum number of hours of bright sunshine. As a result, the image used for this research which, was acquired on November 22,1989, apparently has almost no errors introduced by cloud coverage.

Mean Monthly Rainfall

in millimeter

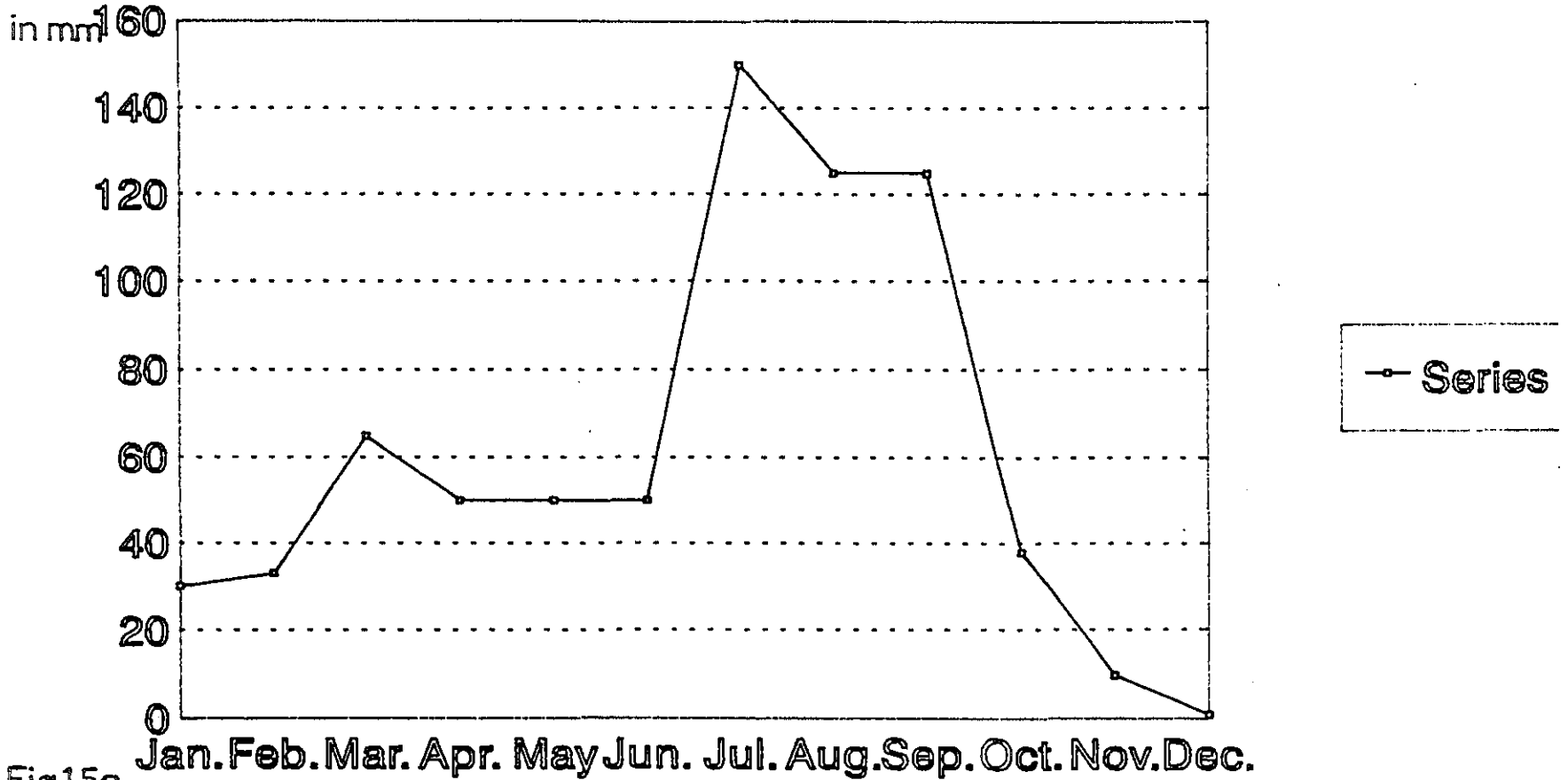

Fig.1.5a.

Only for the image acquisition year 1989

MEAN MAXIMUM AND MINIMUM TEPERATURE

In degree centigrade

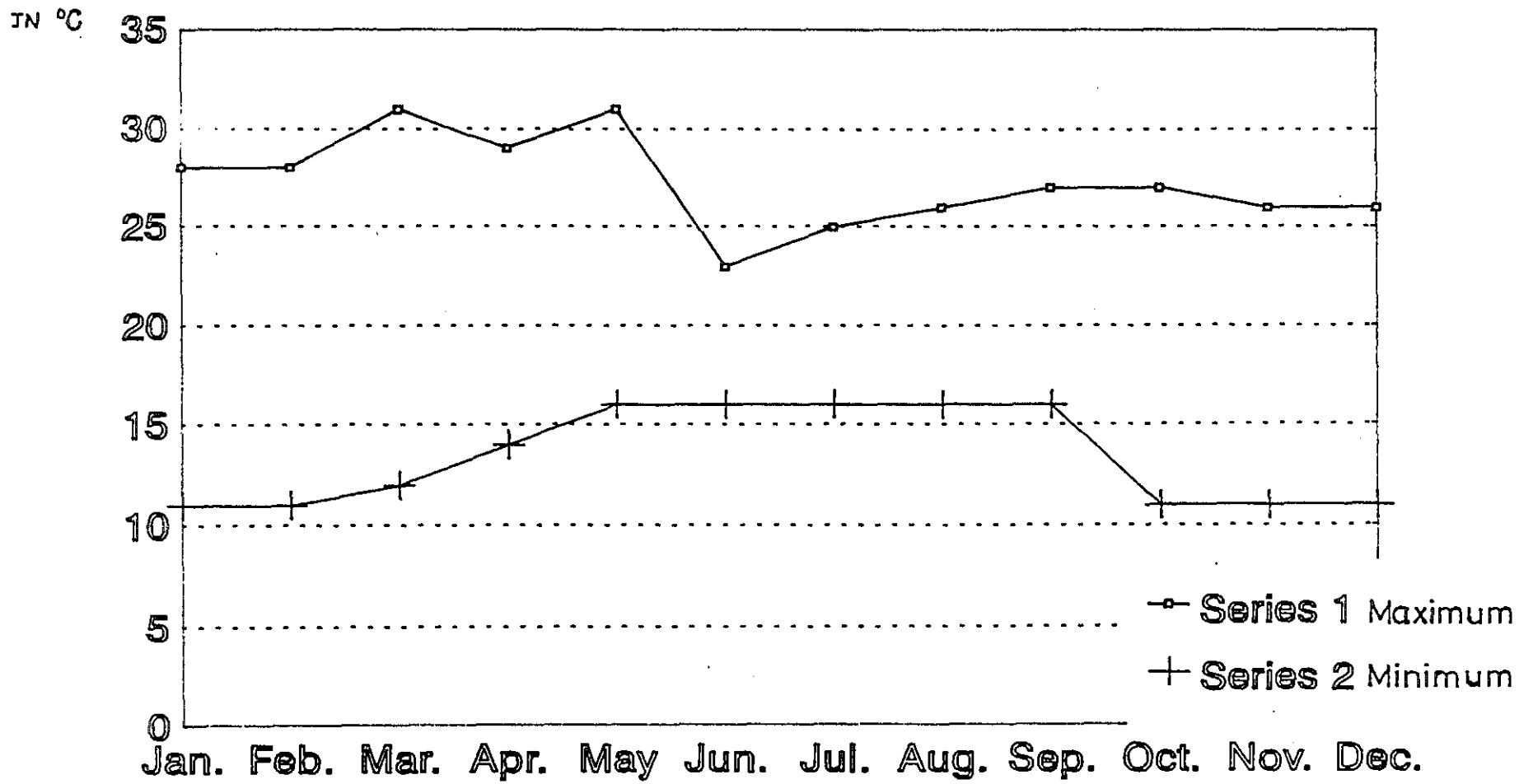

Fig.15b.

For the year 1989

MEAN MONTHLY NUMBERS OF HOURS OF BRIGHT SUNSHINE

In hours

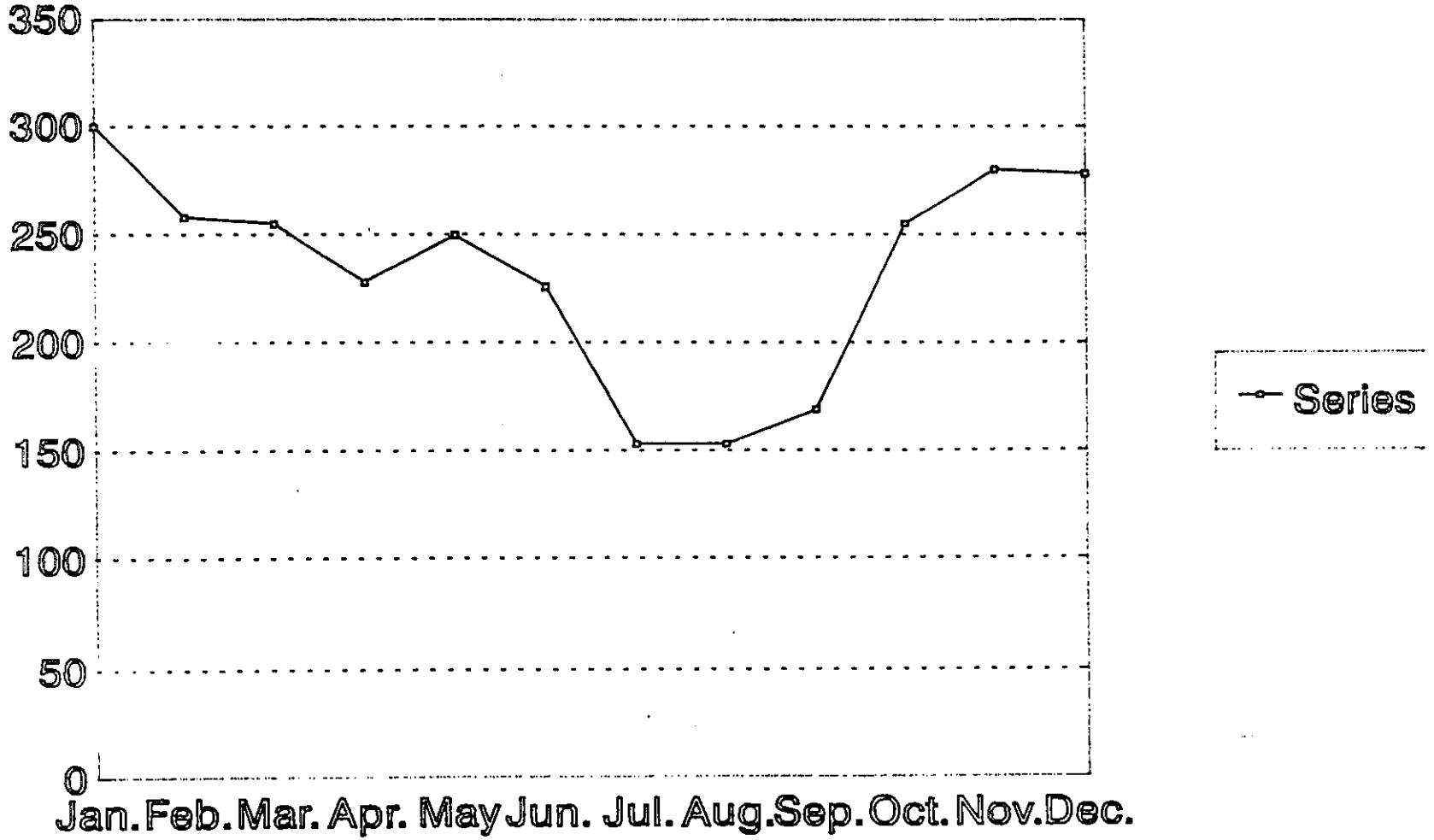

Fig.1.5c.

Only for the image acquisition year 1989

1.5.2.Vegetation

The vegetation cover within the study area changes with elevation from the depressed part of the rift valley (1640m.a.s.l.) to the elevated land on the slope of Mount Chilalo (2820m.a.s.l.).

The classification of the area into vegetational zones as given in the following section is based on the works of Mengistu (1975) and Lill and Lundgren (1969).
According to these authors, the area of interest can, in a generalised manner, be classified into three vegetational zones. These are:

1. Hihgland area (2000-3000m.a.s.l.)

This ecological zone occupies the mountain slopes, valley bottoms, open and rolling plains. It is constituted of three major, distinct plant communities: Hagenic and Juniperus forest, podocarpus forest and open grassland.

2. Medium altitude area (2000-2500m.s.l.)

The lower limit of this zone coincides, approximately with the Plateau-Rift boundary. The vegetation in this area can be generalised as Podocarpus forest, scattered tree grassland with Accacia trees, and open grassland.

3. Lowland area (lower than 2000m.a.s.l.)

The lowland area costitutes mainly the rift floor and includes part of the main rift escarpment. In the study area, this zone is characterized by altitudes in the range of (1640-2000m a.s.l.). It consists of swamps, grassland and scattered tree grassland with accacia as the dominant tree.

Eventhough, the above classification holds true in a general sense, the populated areas are devoid of any natural forest.

In the rift floor where accessibility is restricted due to rough topography, the vegetation cover is in its natural state. The younger geologic activity in the rift valley has not permitted the development of soil horizons especially on the pumice domes and ridges, scoria cones and rhyolite domes. As a result there are no bigger trees growing on these rock bodies. However, the rift floor basaltic flows are relatively populated by spesfic types of trees and can be mapped geobotanically.

In Remote Sensing study of lithology, it is very important to know the species of trees that grow on particular types of bedrocks, because reflectance that comes from plants may masks completely that coming from bedrocks in some wavelength ranges and only the reflectance that comes from the plants helps in mapping the bedrock.

1.6 Regional Geology

Volcanic and tectonic events in the study area constitute an essential part of the volcano-tectonic history of the Main Ethiopian Rift. Therefore, it is necessary to present a summary of the most important features of the Main Ethiopian Rift before discussing the geology of the study area.

The Main Ethiopian Rift is a part of the great East African continental rift and lies between lat. 5o00' - 9o00'N. and long. 37o30' - 40o00'E. The MER is divided geographically into three sectors: northern, central and southern. It divides the 1,000km wide uplifted Ethiopian volcanic province asymmetrically into the northwest and southeast plateaus. The adjacent plateaus on either side of the rift are characterized by huge piles of basaltic and rhyolitic flows and a number of large and small shield volcanoes and by relatively less intense tectonism.

The Main Ethiopian Rift is a huge graben which in its southern section is occupied by a number of volcano-tectonic lakes. It is characterized by normal, step faults of various dimensions and throws, commnly arranged in an echelon style and trending mainly along NNE-SSW and rarely along NE-SW, N-S ,and NW-SE directions. (Mohr 1967; Di Paola 1972; and others).

The central sector of the MER which includes the study area itself is more than 175km long and about 75km wide. It becomes wider toward the northeast (Afar) and narrower southward (Mohr, 1967).

Most of the geologic sections exposed along the rift margins are dominated by Tertiary volcanic rocks except for a few locations where crystalline basement is unconformably overlain by Mesozoic marine sedimentary and and/or Tertiary volcanic rocks. Such pre-Tertiary rocks are present along the eastern, western and southern Afar margins (Huchinson and Engles, 1970; Mohr, 1970; Zanettin and Justin - Viseotin, 1974; Black and others, 1975; Chessex and others, 1975), western rift margin (Guraghe Mountains) of the central sector of the MER (Weldegabriel and Aronson, 1986), and at Amaro Horst of southern sector of the MER (Levitte and others, 1974; Zanettin and others, 1978). In the broad rift zone of southwest Ethiopia, crystalline basement is unconformably overlain by various Tertiary (12.7 - 49.4 Ma) and Quaternary volcanic rocks, including the oldest known (Eocene) flood basalts in Ethiopia (Davidson and Rex, 1980; Davidson, 1983). In general, the floor of Ethiopian Rift is characterized essentially by Mio-Pliocene to present volcanism and volcano-sedimentary products (Abbate and Saggri 1979 in : Merla et al 1979).

Based on stratigraphic relationships and K/Ar dating of

volcanic rocks from both the escarpments, flanking plateaus, and from the rift floor of the central sector of the Main Ethiopian Rift,(Weldegabriel, Aronson and Walter 1990) six major volcanic episodes are recognized in the rift's development over a time span from the late Oligocene to the Quaternary.

Many authors (Burke and Dewey 1970, and others) relate the development of the East African Rift to the Afro-Arabian doming in lower Tertiary times. On the other hand, Bahat (1979); Mc Connel and others, (1980) maintain that the East African Rift as a whole, initiated as an ancient fracture. A recent view by Weldegabriel et al, (1990) based on structural and stratigraphic relationships from the central sector of MER indicate a two-stage rift development. The initial stage was characterized by the development (in late Oligocene or early Miocene) of a series of half - grabens along the rift with alternating polarity, such as that in the present Gregory and Western Rifts of East Africa and a second phase of symmetrical rifts that evolved from these half grabens in late Miocene and early Pliocene times. Thus, evolution from alternating half graben to a full symmetrical graben with a medially located neovolcanic zone that is biforcated to marginal grabens in the northern sector of the MER may be a fundamental part of the rift process.

2. BASIC CONCEPTS OF REMOTE SENSING

Remote sensing data basically consists of wavelength-intensity information, acquired by collecting the electromagnetic radiation leaving the object at specific wavelengths and measuring its intensity. The objects imposes its characteristic imprint on the wavelength-intensity relationship. In order to recognize the object, it is necessary to know how it affects the intensity of the radiation, and to do so requires an understanding of the nature of electromagnetic radiation and the way it interacts with matter.

2.1.Electromagnetic Radiation

As far as electromagnetic radiation is concerned, the basic idea of quantum theory is that radiant energy is transmitted in indivisible packets whose energy is given in integral parts of size (E=h x f), (where h is planks constant=6.6252 x 10^{-34} J/Sec. and f the frequency of radiation), and these are called quanta or photons.

The particular importance of the quantum approach for remote sensing is that it provides the concept of discrete energy levels in materials, and the values and arrangement of these levels is different for each material. Information

about a given material is thus available in electromagnetic radiation as a consequence of transition between these energy levels, a transition to a higher energy level being caused by the emission of energy. The amounts of energy either absorbed or emitted correspond precisely to the energy difference between the two levels involved in the transition. Because the energy levels are different for each material, the amounts of energy a particular substance can absorb or emit are different from those of any other materials. Consequently, the positions and intensities of the bands in the spectrum of a given material are characteristic of the material.

2.2. Electromagnetic Spectrum

It is the ordering of electromagnetic radiation according to wavelength, frequency and energy.

f=c/l where f: frequency
c: speed of light (EMR)
l: wavelength and

E=h x f E: energy of radiation
h: planks constant

E=h x c/l energy is inversely related to the wavelength.

Electrmagnetic spectrum has been divided into regions that bear names related to the source that produced it, such as the "ray"regions; or extensions from the visible range, such as the ultraviolet and the infrared regions or according to the way in which wavelengths in a range are used -such as radio and television. Figure 2.2 shows the wavelength ranges covered by each of these radiation types, together with the various effects that produce spectral features in each of these regions.

2.3. Interaction of Electromagnetic Radiation with Atmosphere

All radiation that comes to earth must pass through a dense atmosphere. Before reception by a satellite mounted, passive sensor using reflected solar radiation, the radiation must pass down through the atmosphere and then back again to the sensor. For a sensor measuring radiation emitted by the earth, although the path is single, there is some effect.

As well as oxygen and nitrogen, the atmosphere contains significant amount of water vapor, ozone (O_3) and carbondioxide. All of these interact with EMR by vibrational and rotational transitions, the net effect being absorption of energy in specific wavebands. At short wavelengths these

bands are narrow, but their width increases in the infrared and microwave regions. Figure 2.3 shows that 50% of the EM spectrum is unusable, simply because non of the corresponding energy can penetrate the atmosphere to the surface. In the case of gamma-rays, only by flying quite close to the ground can energy be detected.

Another irritation to the remote sensor is blue sky. This is caused by one of a number of phenomena resulting from the diffusion of radiation by matter, which is commonly called scattering. The type of scattering varies with the size of particles responsible. If the EMR interacts with particles smaller than its wavelength, such as molecules of oxygen and nitrogen, the scattering is known as Rayleigh scattering. The effect is to swamp the real reflected blue and ultraviolet radiation with a high scattered component, and to reduce contrast. For this reason many remote sensing techniques omit blue from their coverage using different filters.

Where atmospheric particles are smaller in size than the incoming radiation, as is the case for giant molecules of water and for dust, Mie scattering results. This affects wavelengths longer than that of blue light, and is a problem in clear but humid or dusty atmospheric conditions. There are also distortions produced by temperature variations in the air, which produce flactuations in its refractive index and a range of optical anomalies, such atmospheric shimmer forms an

important constraint on just how small an object remote sensing can detect, irrespective of the theoretical resolving power of each system.

All of this implies that remotely sensed images of the Earth are an avoidably degraded in various ways by the atmosphere. It also means that only some wavebands are available for surveillance. Those wavebands that pass relatively undiminished through the atmosphere are referred to as atmospheric windows. They determine the framework where in different methods of remote sensing can be devised.

2.4.Interaction of Electromagnetic Radiation with Surface Materials

The most important natural constraint on remote sensing system design is the interaction between EMR and those solids and liquids that comprises the Earth's surface. There are only three important components: water, vegetation and minerals making up rock and soil. For the geologist, the interactions between EMR and rocks and soils are most important. However, since these materials can contain water or have vegetation growing on them, these must also be considered.

2.4.1. Spectral Behaviour of Minerals and Rocks

The most important processes involved in an interaction between EMR and minerals and rocks are electronic and vibrational transitions, the former characterize the short-wavelength, visible range, where as the latter dominate the longer-wavelength infrared.

Rocks are assemblages of minerals, so their spectra are composites of those for each of their constituents. Minerals, in turn, comprise various proportions of different elements, held together as molecules by different bonds.

The most common ingredients of rocks and the minerals which make them up are oxygen, silicon and aluminum together with varying proportions of iron, magnesium, calcium, sodium and potassium, and smaller amount of other elements. Oxygen, silicon and aluminum atoms have electron shells whose energy levels are such that transitions between have little or no effect on the visible to near-infrared range. Because they can exist as ions with different valencies in different minerals such as silicates, carbonates, oxides, etc., the transition metals iron, copper, nickel, chromium, cobalt, manganese, vanadium, titanium and scandium exhibit a great range of possibilities. Since iron is by far the most abundant of these metals, its effects are the most common and

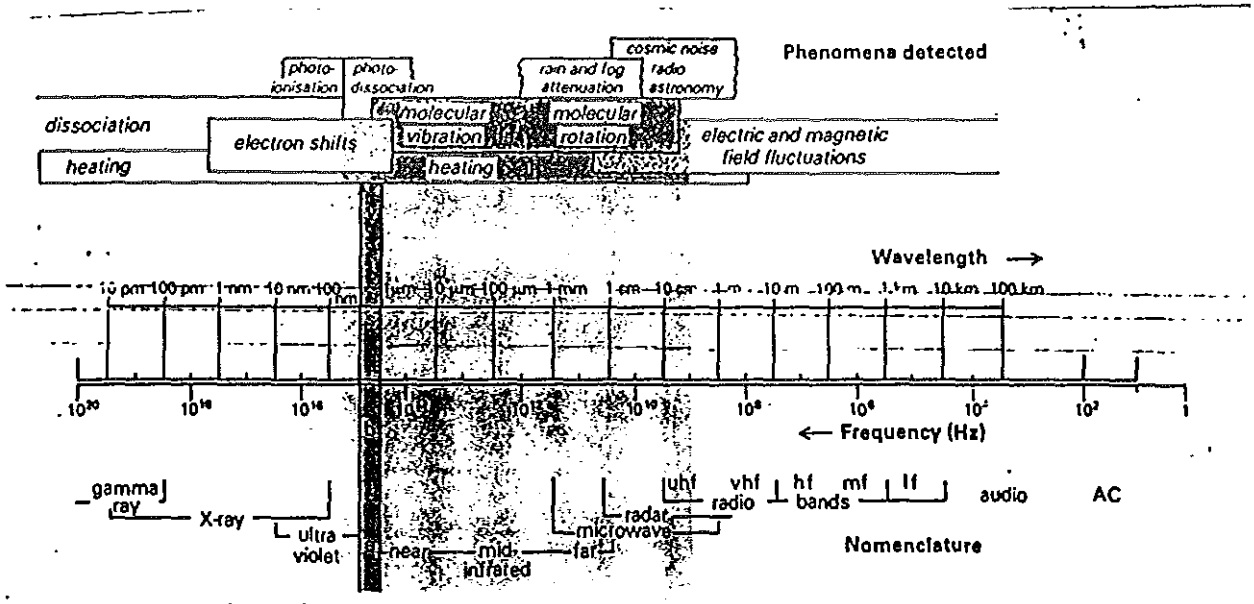

Figure 2.2. This summary of that part of the electromagnetic (EM) spectrum routinely detected by scientists shows the relationship between wavelength and frequency, the phenomena which are involved in the generation and interaction of EMR, and the nomenclature for different parts of the spectrum. Those portions covered by this book are highlighted, together with the processes relevant to geological remote sensing. The narrow visible band is useful as a reference. The wavelength and frequency scales are logarithmic.

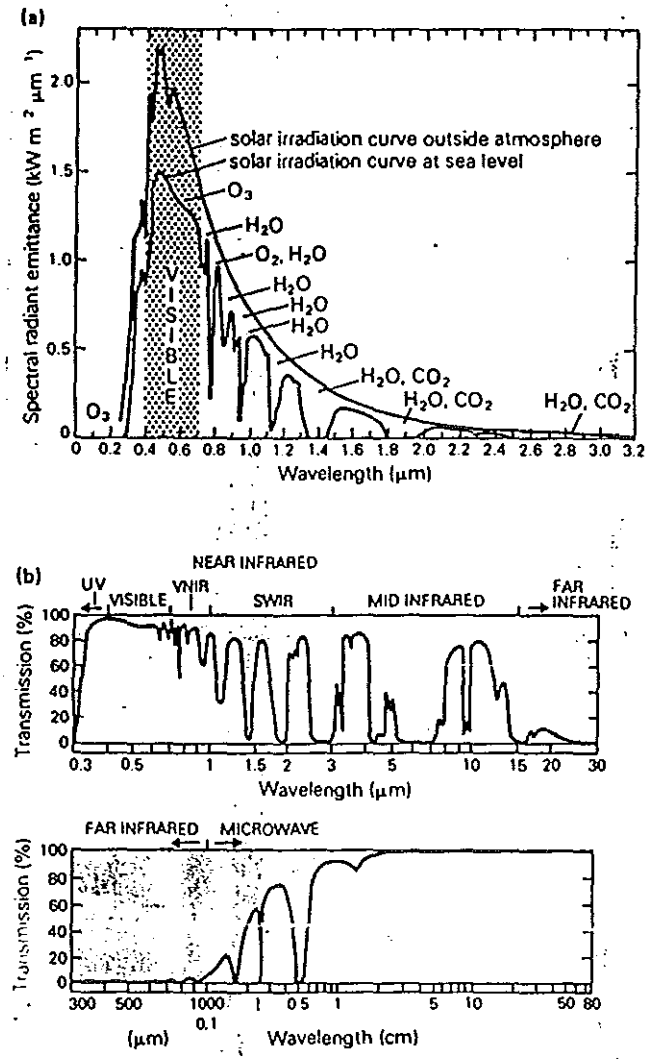

(After Drury, S.A., 1987)

Figure 2.3. Various gases in the atmosphere absorb solar energy in different wavebands by vibrational and rotational transitions. As a result, the solar irradiation curves measured in outer space – upper curve in (a) – and at the surface - lower curve in (a) – are very different. The energy available for interactions with matter at the surface is divided into discrete atmospheric windows separated by bands dominated by atmospheric absorption – grey. In (b) the main atmospheric windows throughout the whole of the useful part of the EM spectrum are shown on a logarithmic scale, in terms of the percentage transmitted through the atmosphere. These two graphs, together with the

the most marked. Figure 2.4a shows the reflectance spectra of several iron bearing minerals which show features due to electronic transitions in ferrous ions. The different wavelengths of the features relate to the symmetry, degree of lattice distortion and co-ordination of ferrous ions in the different minerals. The features are troughs, indicating that absorption of energy takes place over the band wavelengths involved, in order to cause electronic transitions. All of these features are due to transitions in discrete ions and result from crystal-field effects.

Another type of electronic transition results from the presence in metals ions of electrons that have sufficient energy that they are not strongly attached to any particular ion, and so may transfer from one ion to another. This is the property that imparts high electrical conductivity to metals. A similar transition, called a charge-transfer, can occur in a mineral. This, too, is induced by energy in narrow wavebands of EMR, giving rise to absorption features. The most common charge-transfer is involved in the migration of electrons from iron to oxygen,and results in the Fe-O transfer band at wavelengths shorter than about 0.55 micrometer. This charge transfer is common in all iron bearing minerals, and is responsible for a steep decline in reflectance towards the blue end of the spectrum. The most

noticeable effect is with iron oxides (fig.2.4b), this being the reason why these minerals and rocks containing them are yellow, orange or red.

In the part of the spectrum where EMR emission reaches a peak and an atmospheric window allows radiation to be sensed remotely (8-14 micrometers), the most important transitions are vibrational and relate to Si-O bonds. This phenomena is best shown by transmission spectra, and they occur in all silicates (see fig.2.4c). The most important feature in this family of spectra is that the minimum of the main absorption troughs shifts according to the type of silicate structure involved. So, too, does the peak of the short-wavelength edge of the absorption trough. A partial explanation for this is that in different silicates the SiO4 tetrahedra share oxygen atoms in different ways. The advantage for the geologist is that the progressive shift of the short-wavelength peak and the main trough towards longer-wavelength corresponds to a transition from felsic to increasingly mafic minerals.

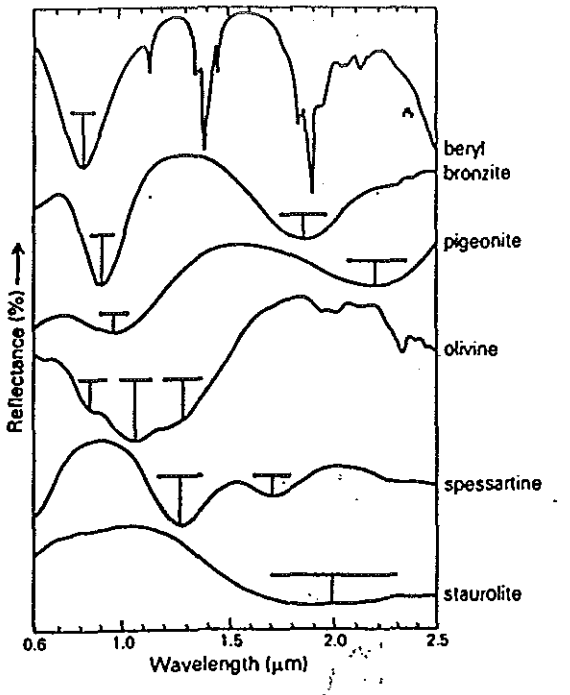

Figure 24a The number and position of features due to electronic transitions in iron minerals (T-shaped symbols) depend on the coordination of Fe^{2+} ions in the molecular structures of the minerals concerned. The spectra are offset vertically for clarity.

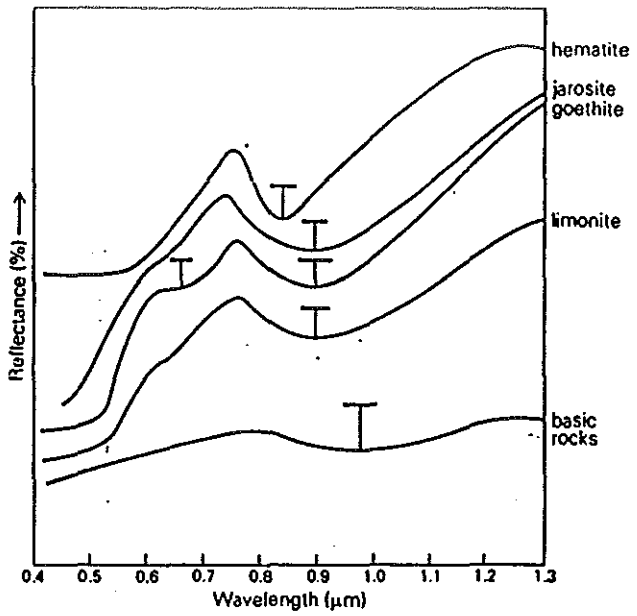

Figure 24b Iron oxides and hydroxides display absorption features due to crystal-field effects (T-shaped symbols) and Fe–O charge transfer in their reflective spectra. Substitution of iron in clay minerals superimposes similar features on clay spectra. The spectra are offset for clarity.

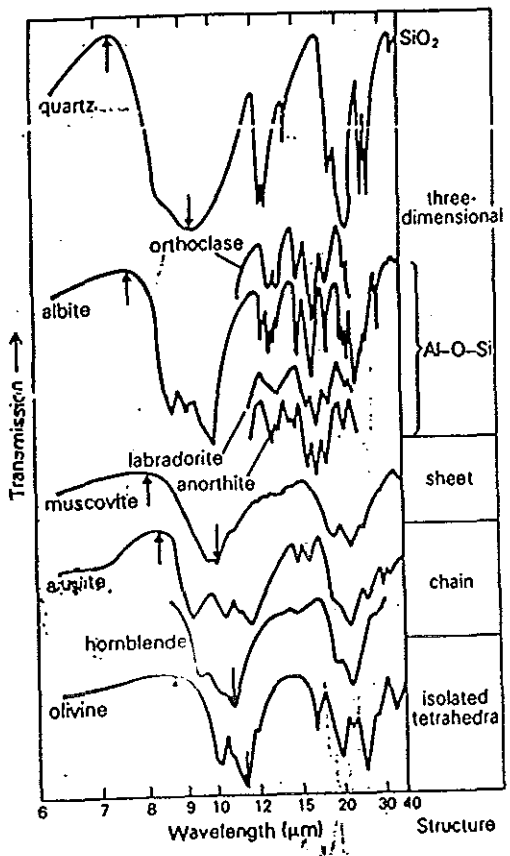

Figure 24c. Because of differences in the structure of silicates, the positions of both the Si–O bond-stretching trough and its 'shoulder' at shorter wavelengths (removal occur at slightly different positions in the mid-infrared spectra of different silicate minerals. The spectra result from experiments using transmitted energy, but would appear very similar for emission. The spectra are offset for clarity.

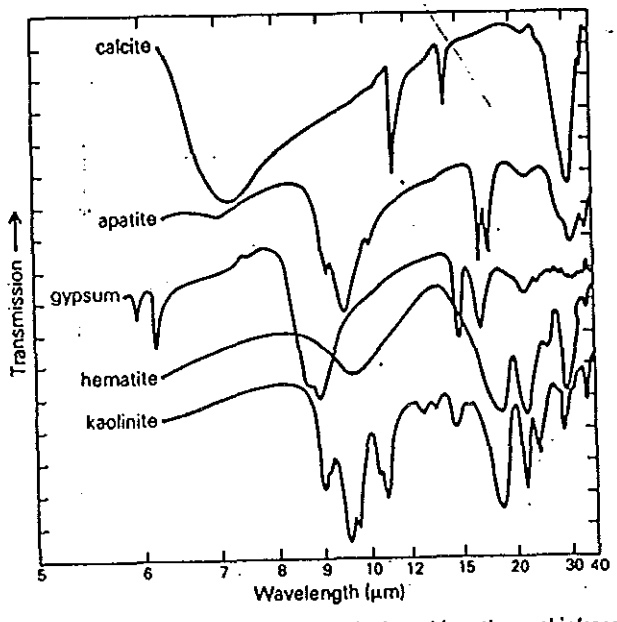

Spectra of non-silicates in the mid- or thermal infrared parts of the spectrum show completely different patterns of absorption features from silicates. They are also very different from each other, suggesting great potential for lithological discrimination by remote sensing of emitted thermal radiation. The spectra are offset for clarity.

(After Drury, S.A, 1987)

2.4.2. Interaction of Electrmagnetic Radiation with Vegetation

Depending on the climate and whether soils are derived directly from underlying bedrock or have been transported, vegetation may show variations that relate to geology. plants use solar energy to convert water and carbondioxide to carbohydrate and oxygen through the process of photosynthesis. How they do has strong influence on their interaction with EMR.

The catalyst for photosynthesis is the pigment chlorophyll, a complex organic compounds which contain iron. The function of chlorophyll is to absorb solar radiation, and there by fuel phtosynthesis. This is achieved by absorption bands near 0.45 and 0.68 micrometer in the blue and red parts of the electromagnetic spectrum. That is why healthy leaves appear green.

However, chlorophyll is unstable above a certain temperature. To protect it from thermal breakdown plants have evolved means of balancing energy. this is achieved by strong reflection of near infrared radiation, partly by shining coating to leaves, but mainly by the internal cells themselves. The structure of plant is such that upto 50% of incident near-infrared radiation is reflected internally. The remainder is directly transmitted through the leaves. Beyond

about 2.0 micronmeter leaves absorb near-infrared radiation.

The different cell structures, proportions of chlorophyll and other pigments, water content and surface morphology of different plants have a marked effect on their spectral properties in the visible to near infrared spectrum. Moreover, plants are assemblages of leaves, spaces, and sometimes branches, with different leaf shapes and sizes, and so on. All of these individual interactions in such compound structures can infer and further broaden the range of responses. This eases discrimination between species, and between healthy and stunted members of the same species.

Since organisms have life cycles of various durations, their spectral properties are not fixed. As a deciduous leaf matures before falling its chlorophyll content decays away, removing the strong red absorption. Consequently, it changes colour from green, through yellow to red. As cells shrink and dry they become less efficient at reflecting near infrared. As leaves fall progressively less of the plant intercepts solar radiation, and the reflectance becomes dominated by the soil and leaf litter beneath it. When new leaves appear, near-infrared reflectance is well developed, coupled with high yellow reflectance. As chlorophyll begins to be metabolized the blue and red absorption bands develop, until visible reflectance reaches a minimum at the height of the growing season.

3. LANDSAT MSS AND TM AND AERIAL-PHOTOGRAPHS CHARACTERISTICS AND THEIR SIGNIFICANCE IN MAPPING LITHOLOGY AND GEOLOGICAL STRUCTURES

3.1. Comparison of Aerial-photographs, MSS and TM Imageries.

Prior to availability of satellite imagery, geologist relied on aerial phtography to provide synoptic coverage of a study area. Colour,black and white, and infrared aerial photography for geologic interpretation is limited by a number of factors, including:

1. Poor spectral resolution: the broad-band spectral range of aerial phtographic film is generally insufficient to separate different lithologies.

2. The scale of aerial photography is commonly insufficient to recognize large surface features. Large features often requires a cumbersome number of photographs to provide complete coverage.

3. Acquisition of aerial phtography in remote and inaccessible areas can be prohibitive due to costs of mobilizing and flying for a photographic mission.

4. Geometrical distortion is higher in aerial photographs. The successful launching and operation of the Landsat Earth Observation Satellites since early 1970s has provided the geologist with another useful mapping aid. Data from the

landsat multispectral scanner (MSS)have been successfully applied for regional structural and lithologic mapping primarily in sparsely vegetated areas. However, the ability to use MSS imagery for detailed geologic interpretation in both non vegetated and vegetated areas has been restricted because of laminations in the spatial and spectral resolution of the MSS sensor. Goetz et al, forexample, noted that the major drawbacks of using landsat MSS images for geologic purposes have resulted from the luck of streo-pairs, coarse spectral resolution, and limited spectral coverage (0.5-1.1 micrometer) which does not extend into regions of the spectrum of most use in characterizing the spectral properties of geologic surface materials and low spatial resolution attained by the MSS as compared to TM.

3.2. TM Characterstics

The landsat thematic mapper (TM) is an earth resource imaging system that provides data of improved spectral, spatial and radiometric resolutions. It is a mechanical scanning device as for the MSS, and assembled on Landsat 4 and 5 satellites.

It incorporates several innovation over the MSS. Instead of using fiber optics to carry radiation to the detectors, the detectors are placed directly at the focal planes of optical system. One of these focal planes carries four banks

of 16 detectors for four bands in the range of (0.45-0.90 micrometer). Another is refrigerated by a radiative cooler and carries two banks of 16 detectors for emitted infrared. The resolution in these channels is 30m, an imrovement of 2.6 times over that of the MSS. Resolution of the thermal channel is 120m.

TM digital data is obtained in seven spectral bands

TM spectral bands	Wavelength (micrometer)	Instantaneous field of view (IFOV)
1	0.45-0.52 (blue)	30 x 30 m
2	0.52-0.60 (green)	30 x 30 m
3	0.63-0.69 (red)	30 x 30 m
4	0.76-0.90 (near-IR)	30 x 30 m
5	1.55-1.75 (mid-IR)	30 x 30 m
6	10.4-12.5 (thermal-IR)	120 x 120m
7	2.08-2.35 (mid-IR)	30 x 30 m

TM band 7 is out of sequence since it was added last in the design after the previous six bands had been firmly established. It was incorporated at the request of the geological community owing to the 2 micronmeter region in assessing hydrothermal alteration.

Thematic mapper scenes are identical in size to those from accompanying MSS, but because of the improved resolution and larger number of channels they comprise nine times as many digital numbers. This posses considerable difficulties for transmitting, receiving and handling of the data.

3.3. Significance of Orbital and Synoptic Imagery

The first three landsats have had identical orbit characterstics, as summarized in the following table.

Landsat 1,2,3 orbit characteristics

Orbit:	Sun synchronous,near polar; nominal 9:30A.M descending equatorial crossing; inclinded at about 99 degree to the equator.
Altitude:	920km (570mi)
Period:	103min.
Repeat cycle:	14 orbits per day over 18 days (251 revolutions)

The orbits are near polar and are sun synchronous that is, the orbital plane precesses about the earth at the same rate that the sun appears to move across the face of the earth. In this manner data is acquired at about the same local time on every pass.

The satellite acquire image data normally at 9:30 A.M local time on a descending (north to south) path ; in addition landsat 3 obtained thermal data on a night-time ascending orbit for the few months that its thermal sensor

was operational. Fourteen complete orbits are covered each day, and the fifteenth, at the start of the next day, is 159km advanced from orbit 1, thus giving a second day coverage contiguous with that of the first day. This advance in daily coverage continues for 18 days and then repeats. Consequently complete coverage of the earths surface is given, with 251 revolutions in 18 days.

The orbital characteristics of the second generation landsats, commencing with landsats 4 and 5 are different from those of their predecessors. Again image data is acquired normally at 9:30A.M local time in a polar, sun synchronous orbit ; however the space craft are at the lower altitude of 705km, both to assist in achieving higher resolution and to avoid shuttle recovery for refurbishing. This lower orbit gives a repeat cycle of 16 days at 14.46 orbits per day. This correspond to a total of 233 revolutions every cycle. The next table summarizes the landsat4,5 orbit characteristics.

Orbit Parameters for Landsat 4, and 5

Orbit:	Near polar, sun synchronous ; nominal 9:30A.M descending equatorial crossing.
Altitude:	705km
Period:	98.9min
Repeat cycle:	14.56 orbits per day over 16 days (total 233 revolutions)

Unlike the orbital pattern for the first generation Landsats, the day 2 ground pattern for Landsat 4 and 5 is not adjacent and immediately to the west of the day 1 orbital pattern. Rather it displaced the equivalent of 7 path centers to the west. over 16 days this leads to repeat the cycle.

3.4. Lithologic Mapping

General lithologic descrimination with landsat MSS and TM imagery has been reported extesievly in the literature (Tarnik and Trautwein,1977 ; Abrams and Seigel, 1970; Baired, 1984; Davis et al, 1987); however, application of landsat data to specific lithologic identification has not been comprehensively documented (Sultan et al, 1987).

Investigation of rocks spectra, whole rock geochemistry and landsat imagery indicates that the longer wavelength visible and near infrared thematic mapper (TM) bands 3,5 and 7 provide more effective lithologic descrimination than the shorter wavelength bands due partly to deeper penetration of lower frequency energy and greater primary rock compositional response. Spectral contamination of vegetation degrades lithologic information in band 4. Thus ratios, colour composites, and principal component images using TM bands 3, 5 and 7 generally leads to superior lithologic contrast (refer to chapter 4). Shorter wavelength, TM bands 1 and 2

are affected more by surficial weathering products, such as soils and alluvial and fluvial deposits which may or may not provide indirect link to the subsurface bed rock lithologic identity. Principal component colour composites provide best overall lithologic contrast but not specific lithologic identification. PC2 tends to contain lithologically dominant variance and combines favourably with other images influenced strongly by the lithology. Late magmatic differentiates that are "evolved" with respect to alkalis and the "incompatible" elements exhibit steep spectral curves throughout the TM bands 5 to 7 interval, leading generally to low 5/7 ratios and dark contrast on 5/7 ratio images.

3.5. Structural Mapping

The greater spatial resolution and synoptic capability of the TM coupled with its improved geometric fiedelity and radiometric sensitivity allows smaller geologic surface features to be recognized on TM images compared to MSS images. One measure of spatial resolution is the size on the ground of a single measurement called the ground projected instataneous field of view. This resolution is about 79 by 58 meters for the MSS and 28.5 by 28.5 meters for the TM. TM resolution is sufficient to meet a map of scale smaller than 1:100,000 (Weelch et al.;1985).

Emphasizing the high spatial frequency component of an image can further enhance obscure features (Leith and Alvarez,1985), or peak out features of interest hidden within a cluttered, highly textured, original image (Drury,1986). This may be done by masking out part of the Fourier transform of the image (filtering in the frequency domain) or, more simply, by passing a rectangular "box-car" filter over the image (filter in the spatial domain).

In general, it is the easiest method to produce a mega-lineament map using an edge enhanced, non-directional high pass filtered image, although the confidence level of most detected lineaments is greater if results are combined from directionally filtered images. If more detailed lineament data are required, then directionally filtered edge detection techniques are more suitable, provided care is taken to recognize and discount artifacts such as roads.

4. IMAGE PROCESSING

4.1. Introduction

Image processing includes all complex mathematical manipulations applied on raw digital data so as to obtain imageries that contain details for particular interpretation.

The TM imagery was processed and enhanced at the remote sensing center of Ethiopian Mapping Authority by the Earth Resource Data Analysis system (ERDAS) ver. 7.4 using a Compaq host computer. ERDAS is one of the most powerful and important image processing softwares. It performs all interactive image processing procedures at the rate of the computer and display it on 512 x 512 pixel size screen and enables to export imageries using colour printers, film writer, magnetic tape drive units and floppy diskettes. The interactive display capability enabled me to select through iterations an optimum image enhancement for geologic interpretation.

A number of image enhancements and transformations were performed on the TM imagery to improve the discriminablity of geologic features using TM bands 2, 3, 4, and 5. Each TM images were displayed using three band false colour combinations (fig. 5.2.3a and 5.2.3b). Band correlation

matrix were created for each image (Tables 4.2a and 4.2b) to assist choosing bands for the best band combinations and visual interpretation.

False colour composites of different enhanced spectral band data, principal components, and band ratio (vegetation index) were created and displayed interactively using ERDAS. Edge enhancement techniques were also employed to delineate faults, and other lineaments, lithologic contacts and craters on the false colour composites.

4.2. Band Selection

As mentioned earlier the digital data used in this thesis project is Landsat TM which is supposed to contain seven spectral bands. However, some of the bands for the study area have been found to be incomplete particularly band numbers 1,6 and 7 of which the last two are very essential for geological analyses. To compensate for the lacking bands, different approaches of data enhancement and transformation techniques have been employed. In this respect vegetation index (VI), texture on band 3 and principal component analyses (PCA) data transformation algorithms have been used while histogram equalization which is very essential for display purpose in other applications has intentionally been omitted so as not to enhance other features which do not have

any relevance to this study.

Statistical analysis matrix were done to investigate the distribution of pixels (DN) in every applied bands and represented by standard deviations and variances (Table 4.2a). The variance of a single band expresses the spread of its grey tone values about the mean. But the most important statistical parameter is the covariance in the TM band correlation matrix (Table 4.2b). Correlation matrix helps to choose the best band combination for false colour composites. Covariance is the measure of joint variation of two bands about their weighted mean. When the covariance is positive the data are positively correlated, and therefore there is high redundancy of informations in the two bands. When negative, an inverse relationship exists and the features shown by higher pixel values (DN) in one of the bands will be shown by lower pixel values (DN) in the other band. When covariance matrix is zero, the two channels of the data are completely independent of each other (see table 4.2b)

Table 4.2a Variance and Standard deviation of the four Bands

Band	Variance	Standard deviation
2	719.94	26.83
3	58.72	7.66
4	223.23	14.94
5	173.08	13.16

Table 4.2b Covariance Matrix of the Bands

Band	2	3	4	5
2	719.94			
3	159.15	58.72		
4	309.75	112.58	223.23	
5	207.74	70.34	135.24	173.08

As stated in the above paragraph, except for bands (3-5) and (4-5), there is high redundancy of informations in the bands. The false colour composites for the row data shown in plates 5.2a and 5.2b, in which Bands 5, 3 and 2 in RGB, and 2, 5 and 3 in RGB order give better lithologic contrast. For further enhancement principal component analysis was required.

4.3 Principal Component Analysis

In most cases a high reflectance in one waveband is matched by similarly high reflectance in the others. In such cases the data are said to be highly correlated. High correlation indicates that there is a high degree of redundancy among the data. For many purposes the information in one band is similar to that in the other. High correlation between the three bands that are used to produce a false colour composite results in little improvement over a single band image.

Principal component analysis is a method of improving the

spread of data about another set of axes in multidimensional space, which maximizes the separation of differences in the data.

The original four bands of data are projected onto four principal components as linear, additive combinations by using eigenvectors (Table 4.3a). Each of these is a loading factor for the contribution of each band to a component. As well as transposing the axes through the four bands of data, the covariance matrix is also transformed, so that the covariaces between the bands are set to zero. This decorrelation process has the effect of spreading the data to the limits of the new, principal component axes. The variation within the data is recast as variances on the principal components, known as eigenvalues (Table 4.3b). The highest eigen value is associated with the first principal component, and progressively lower eigenvalues with each higher order principal components. The result is that the first principal component generally a weighted average of all of the data, and approximates an image of the albedo and topography in the range covered by remote-sensing system. The higher order components express deviations of various kinds from this average, and contain information relating to the geological and vegetational variations in the scene. The first principal component also has the greatest contrast, and is usually a very high quality image in its own right. First

principal component image is therefore good for edge enhancement and structural interpretation.

Tables 4.2a, 4.2b, 4.3a and 4.3b summarizes the silent statistics involved in the production of plates 5.2c, and 5.2d. Table 4.2a shows the variance and standard deviations for each of the four bands in the landsat TM images concerned. Table 4.2b shows the covariance matrix for the four bands. The eigenvector matrix in Tables 4.3a and 4.3b shows that PC1 has positive loading on all bands. This confirms that PC1 is roughly an average of all of the bands and, indeed, its image is similar to those of the four bands. The contrast between positive loading for bands 3 and 4 and negative loading for 2 and 5 in the eigenvectors for PC3 suggests that materials showing different spectral responses between these two sets of bands will be emphasized in its image. Likewise in PC4 the negative loading for bands 4 and 5 suggests that there is detailed information on vegetation, soil moisture and rock types in the image PC4. Due to this fact the FCC image (plate 5.2c) of PC 1, 3 and 4 in RGB order gives much details on the types of lithologies and associated soil types and vegetation cover.

Table 4.3a Eigenvectors for PC

Bands	PC1	PC2	PC3	PC4
2	0.83	-0.53	-0.18	0.00
3	0.21	0.22	0.31	0.90
4	0.42	0.43	0.67	-0.44
5	0.30	0.76	-0.65	-0.02

Table 4.3b Eigen values for the bands used

Bands	Eigen values	Var%	Cuml%
2	991.83	84.41	84.41
3	122.58	10.43	94.84
4	59.06	5.03	99.87
5	1.52	0.13	100.00

4.4 Band Ratioing

Ratio pictures have the effect of suppressing the detail in a scene which is caused by topographic effects, while emphasizing colour bounderies. This property has made ratio pictures quite useful in geologic applications because they exaggerate subtle colour differences in a scene, and many geologic problems require the distinction between rock types that may appear to be quite similar. However, ratioing suppresses the ability to descriminate between rocks with strikingly different albedos, but similar reflectance spectra. Removal of atmospheric scattering increases contrast between features in ratio pictures.

The band ratio image for this study is composed of TM

band 3 (red) and TM band 5 (infrared) radiations. The ratio is [band(5-3)]/[band(5+3)]. The image for the band ratio is shown in plate 5.2f in black and white. It enhances all types of rocks outcropped in the area.

4.5 The Image Histogram

An image of a single band of digital remote sensing data is a representation of how the EMR energy reflected by the surface is distributed in two spatial dimensions. The energy is Expressed as DN, which are represented in a display by a variation in grey tones. An image can also be expressed statistically as the probability of finding a DN of a given value within it. For the 0 - 255 range of possibilities, this measure is termed the probability density function . The PDF is most conveniently represented by a histogram of the number of pixels, which regardless of spatial position within an image, have a particular DN.

The histograms shown on pages 48, 49, 50, 51, 52 and 53 indicates the distribution of DN values in the applied ERDAS bands 1, 2, 3, 4, 5 and 6, which is equivalent to PC1, PC2, PC3, PC4, VI, T3 (texture derived from TM band 3) and TM band 5 respectively. The histogram of DN distributions is an important measure in digital image processing. Its shape indicates the contrast and homogenity, of the scene. For

instance, a scene of a homogeneous surface with a low contrast will produce a histogram with a single, sharp peak (fig. 4.5b, 4 .5c and 4.5d sharp peak histogram for PC2, PC3 and PC4). Therefore these three bands contain much information

about particular features. A broad single peak suggests homogenety, but a wide range of contrast (fig.4.5a, 4.5e and 4.5f, histograms for PC1, VI and T3). Other shape attributes of the histogram give a kind of statistical short hand for an image. The presence of tails and the degree of asymmetry of the peak in an image both indicate important structural features which will rarely be obvious from the picture itself. This type of relation is indicated in the histogram for PC2 and VI (fig.4.5b and 4.5e).

Fig 4.5a IMAE HISTOGRAM FOR PC-1

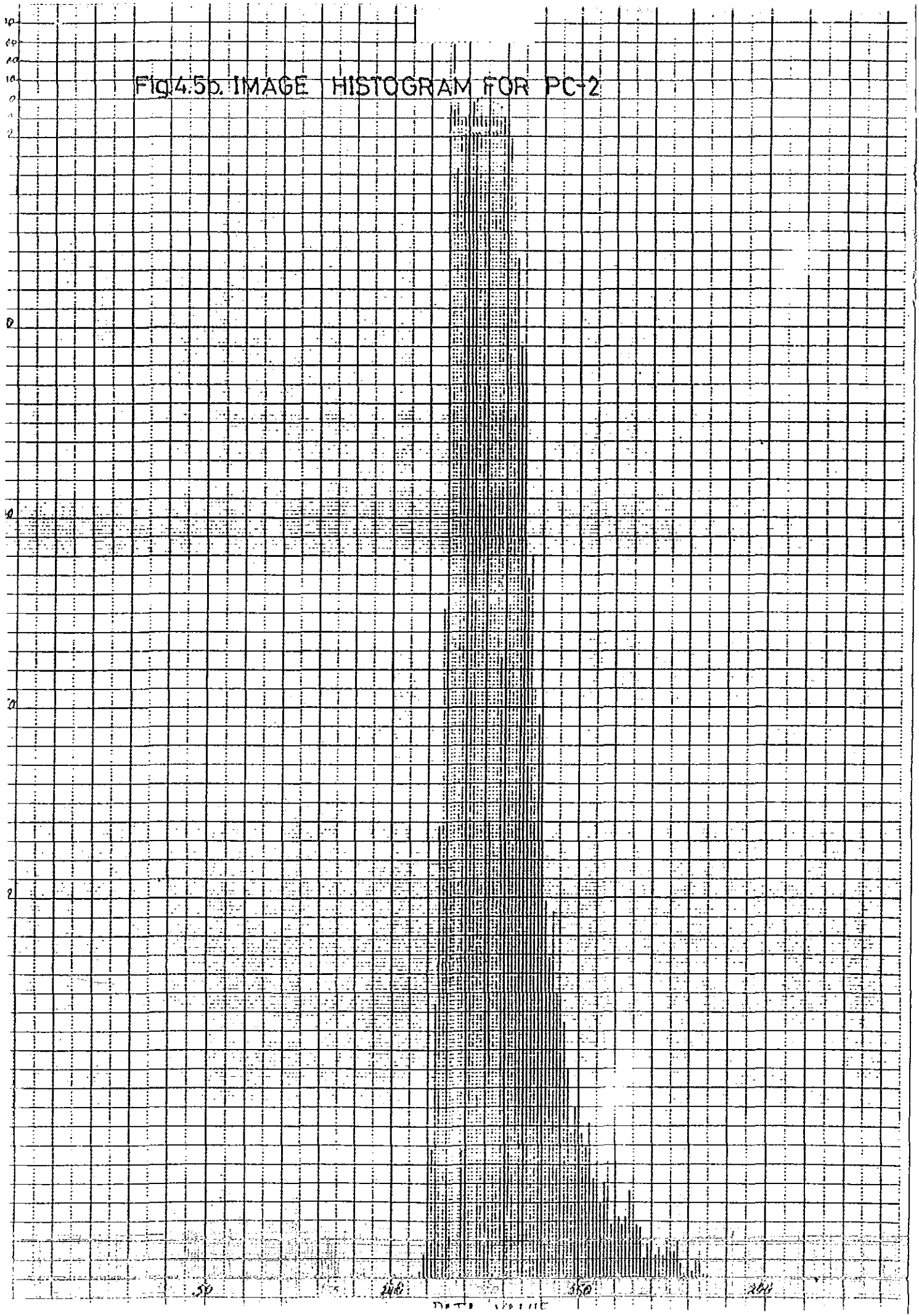
Fig.4.5b. IMAGE HISTOGRAM FOR PC-2

Fig 4.5c. IMAGE HISTOGRAM FOR PC-3

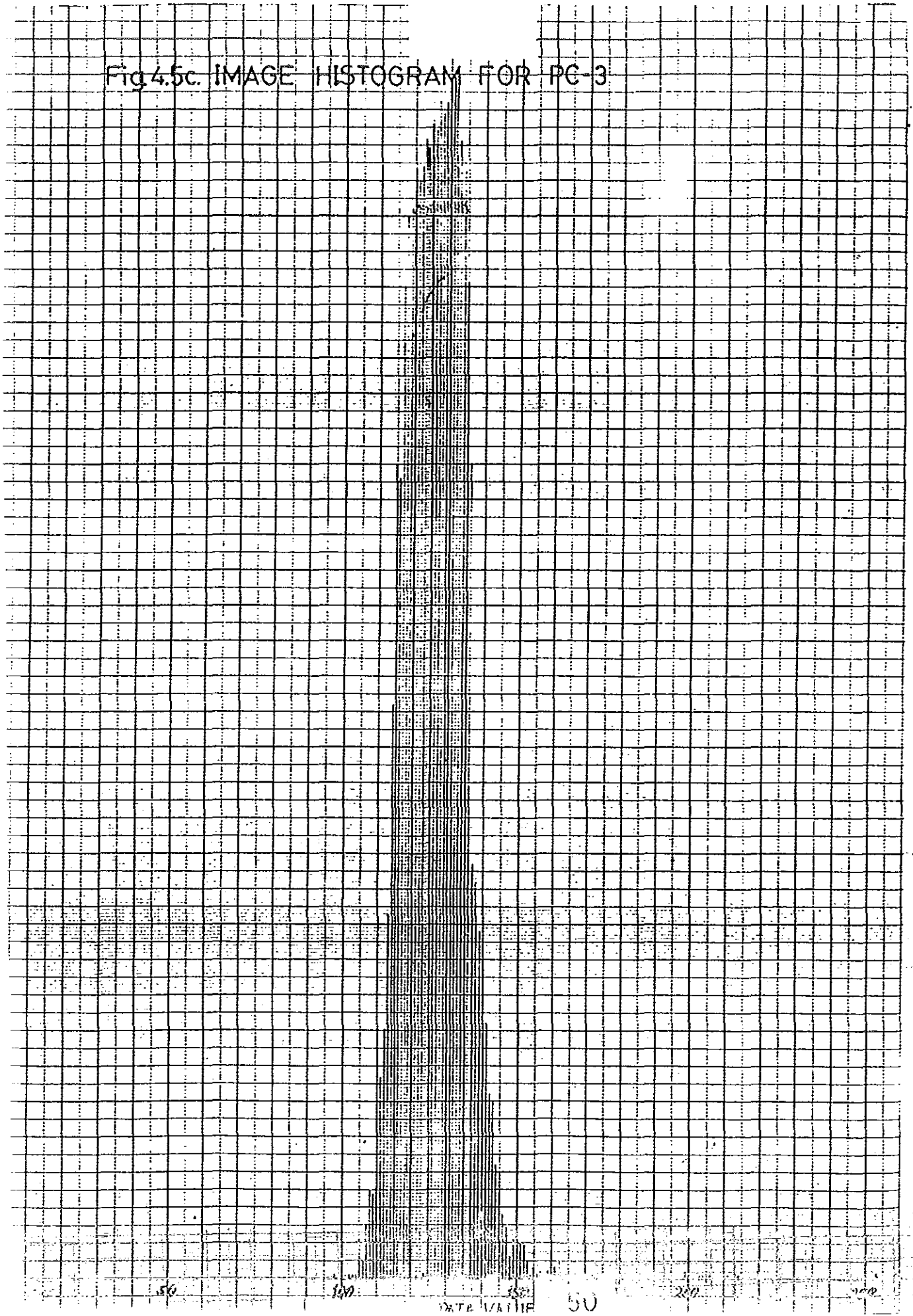

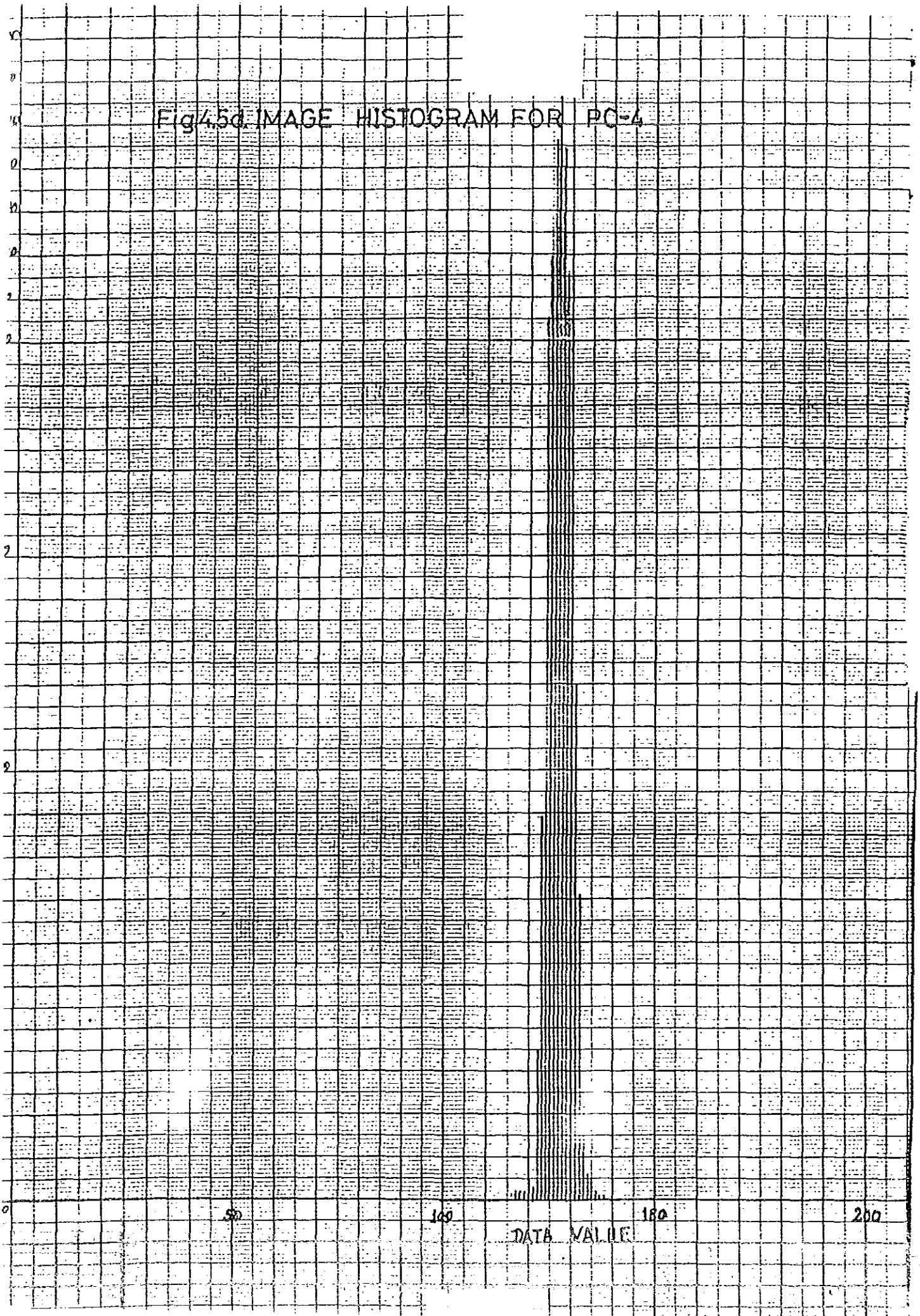

Fig 4.5d. IMAGE HISTOGRAM FOR PC-4

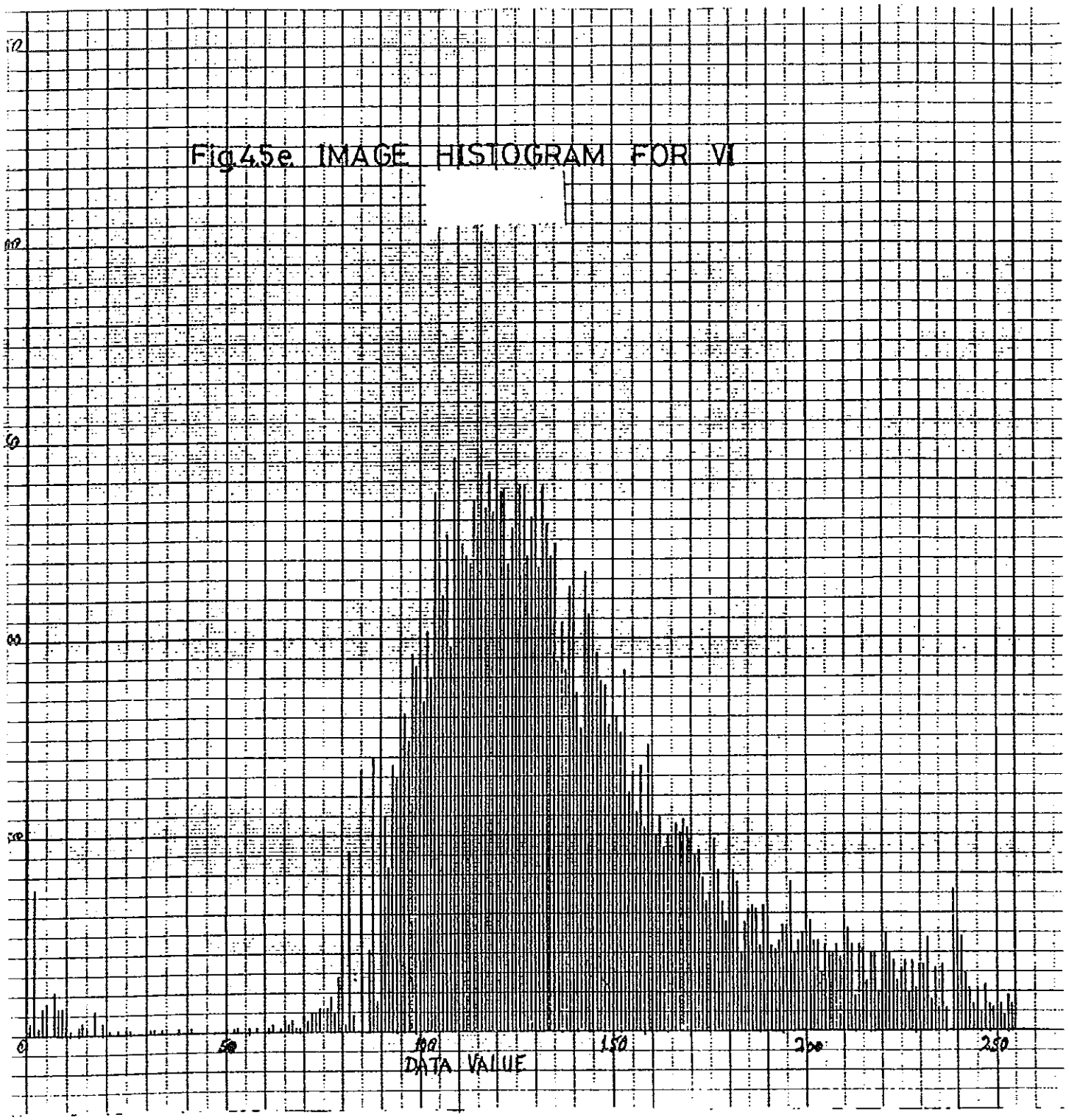
Fig.45e. IMAGE HISTOGRAM FOR VI
0
50
100
150
200
250
DATA VALUE

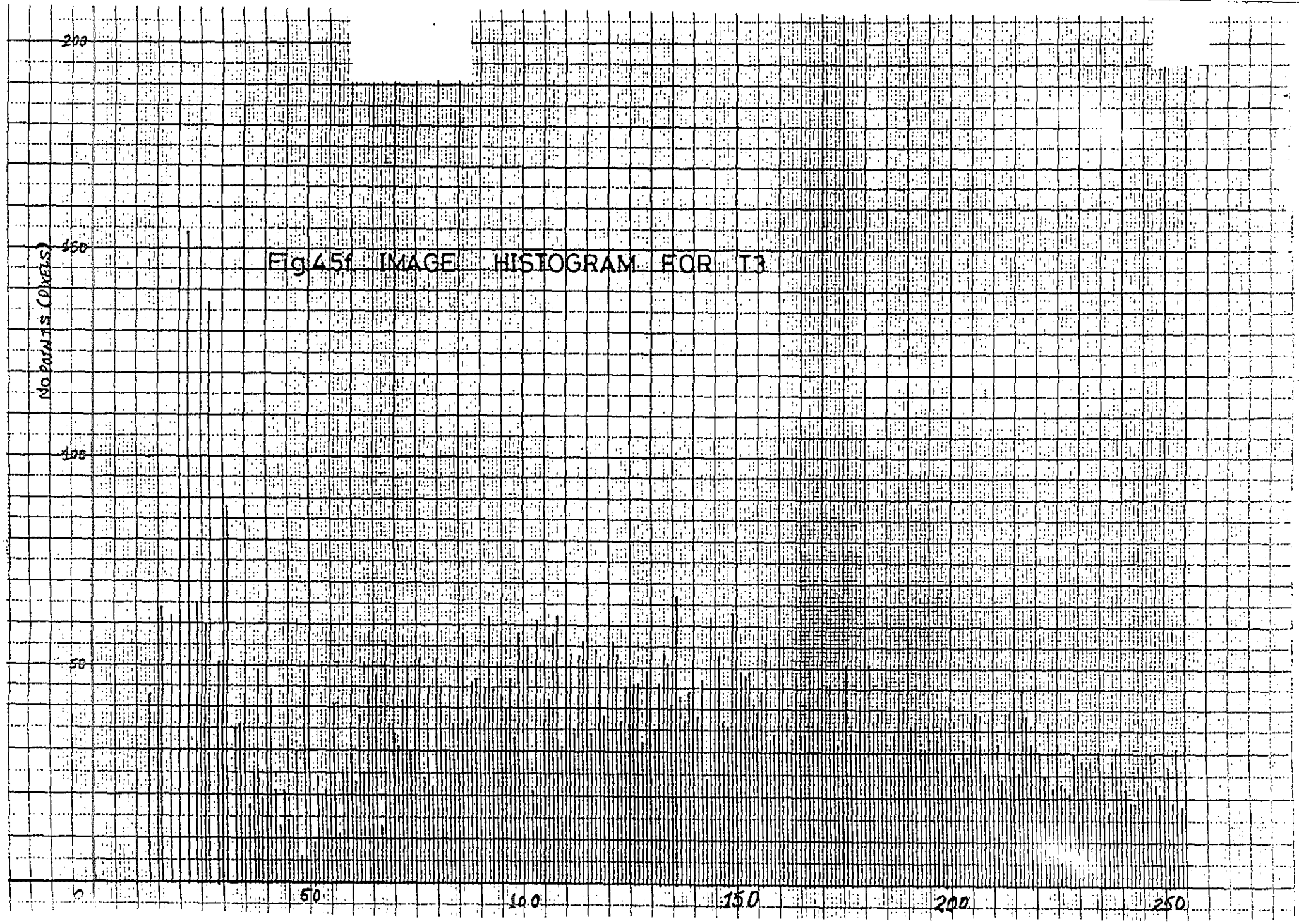

Fig 45f IMAGE HISTOGRAM FOR T3

4.6. Selection of Sample Points (Training Areas)

The test area on which the computer was trained is chosen on the basis of the presence of almost all types of lithologies, structures and landforms that are found distributed in the study area, and its accessibility both by car and on foot to conduct field survey in order to confirm laboratory results.

The test area has the dimenssion of 512 x 512 pixels which is equivalent to 15.36 x 15.36 km.sq. It is located in the northeastern corner of the study area, 12km northwest of the town Iteya.

All statistical analysis and qualitative interpretations before classification were made on the test area. The final result of interactive image processing on the test area were extrapolated to the remaining part of the study area during classification.

Selection of the training areas on the basis of spectral pattern recognition algorithm for geological information extraction possess difficulties. This is so because it makes the identification of the underlying material on the bases of surface features reflectance extremely difficult. However, the selection of the representative samples for all possible classes has been made by relating the field information to the spectral reflectance of surface features in the selected

sites. With the sample pixels carefully selected for each geological types, the building of statistics (see table 4.6) proceeded which is to be used in the subsequent stage of classification.

Table 4.6 signature statistics for assigned classes

Signature Statistics

1.Signature Name: SCORIACEOUS BASALT

Number of Points = 42

Band	PC1	PC2	PC3	PC4	VI	T3	B5
Minimum	85	127	113	125	163	26	82
Mean	88.38	103.26	115.19	126.76	176.29	36.12	84.83
Standard	1.48	1.14	1.03	0.82	6.06	5.24	1.31
Maximum	91	133	117	128	189	47	87

Covariance Matrix

PC1	2.18						
PC2	-0.26	1.30					
PC3	0.22	0.21	1.07				
PC4	0.39	-0.26	-0.09	0.67			
VI	-1.65	5.59	-2.16	-0.20	36.70		
T3	-0.62	-0.36	0.95	0.36	-5.35	27.41	
B5	1.68	-0.54	-0.40	0.40	-1.31	-1.04	1.71

2. Signature Name: OBSIDIAN

Number of Points = 27

Band	PC1	PC2	PC3	PC4	PC5	VI	B5
Minimum	49	134	113	126	219	35	51
Mean	58.67	137.04	115.78	126.67	228.26	54.26	58.41
Standard	3.77	1.01	1.07	0.60	4.29	8.34	3.59
Maximum	70	140	117	127	242	104	69

Covariance Matrix

PC1	24.50						
PC2	2.35	1.46					
PC3	-0.45	0.31	0.80				
PC4	0.65	0.04	-0.04	0.20			
VI	1.89	5.72	-0.09	0.68	35.32		
T3	59.15	6.43	-6.70	1.63	24.85	302.10	
B5	19.97	1.49	-0.88	0.57	0.39	50.63	16.70

3. Signature Name: SCORIACEOUS PORHYRITIC BASALT
Number of Points = 21

Band	PC1	PC2	PC3	PC4	VI	T3	B5
Minimum	100	126	114	126	152	55	94
Mean	105.86	127.86	116.05	127.29	159.38	73.14	99.48
Standard	3.77	1.01	1.07	0.60	4.29	8.34	3.59
Maximum	114	130	118	129	166	85	107

Covariance

PC1	14.18						
PC2	-2.44	1.02					
PC3	-2.32	0.63	1.14				
PC4	0.40	-0.14	-0.19	0.36			
VI	-8.71	3.32	0.24	0.14	18.42		
T3	2.06	-1.28	-0.57	-2.13	-5.78	69.63	
B5	13.33	-2.58	-2.57	0.45	-8.15	1.70	12.86

4. Signature Name: PUMICE AND ASH GROUP-I

Number of points = 37

Band	PC1	PC2	PC3	PC4	VI	T3	B5
Minimum	157	123	109	126	140	77	143
Mean	175.11	130.62	119.43	128.70	159.70	116.05	154.68
Standard	8.93	3.06	5.09	1.23	9.83	33.09	5.28
Maximum	190	136	129	131	177	184	162

Covariance Matrix

PC1	79.81						
PC2	7.92	9.33					
PC3	38.17	5.52	25.93				
PC4	6.93	0.11	4.58	1.52			
VI	-31.21	21.26	-19.73	-5.59	96.60		
T3	-127.11	-64.58	-29.74	2.82	-161.60	1095.10	
B5	44.76	1.72	17.14	3.37	-20.31	-75.33	27.93

5. Signature Name: PORPHYRITIC ALKALI BASALT

Number of points= 32

Band	PC1	PC2	PC3	PC4	VI	T3	B5
Minimum	114	119	120	125	110	44	105
Mean	119.37	120.97	121.69	127.44	117.19	57.59	109.41
Standard	2.42	0.83	1.36	1.00	4.15	6.36	1.81
Maximum	124	122	125	129	125	71	113

Covariance Matrix

PC1	5.87						
PC2	-0.49	0.68					
PC3	1.49	-0.07	1.84				
PC4	-0.24	-0.19	-0.15	1.00			
VI	-4.03	2.20	-3.83	1.13	17.23		
T3	-2.65	-0.22	-0.61	1.19	4.72	40.42	
B5	4.09	-0.59	0.37	-0.02	-2.21	-2.06	3.27

6. Signature Name : TRACHYTIC ROCKS

Number of Points = 15

Band	PC1	PC2	PC3	PC4	VI	T3	B5
Minimum	126	120	116	124	121	60	116
Mean	135.07	122.53	117.33	126.33	130.53	72.00	124.20
Standard	6.89	1.45	0.78	1.42	5.04	7.32	5.83
Maximum	147	125	119	128	140	87	134

Covariance Matrix

PC1	47.45						
PC2	-7.23	2.11					
PC3	3.12	-0.73	0.61				
PC4	7.82	-1.64	0.55	2.00			
VI	-22.51	7.04	-2.89	-4.85	25.36		
T3	45.55	-7.29	2.27	8.12	-21.54	53.51	
B5	40.06	-6.24	2.48	6.75	-19.07	39.07	33.99

7. Signature Name: PUMICE AND ASH GROUP-II

Number of Points = 16

Band	PC1	PC2	PC3	PC4	VI	T3	B5
Minimum	141	126	127	125	123	33	121
Mean	143.00	127.87	129.25	126.62	133.62	48.44	123.56
Standard	1.36	1.35	1.23	0.84	5.60	9.16	1.58
Maximum	146	131	132	128	147	63	127

Covariance Matrix

PC1	1.86						
PC2	-0.91	1.82					
PC3	-0.64	0.21	1.51				
PC4	-0.23	0.84	-0.05	0.70			
VI	-2.79	7.08	-0.84	3.98	31.41		
T3	-3.35	1.81	5.77	0.00	-4.58	83.94	
B5	2.00	-1.17	-1.29	-0.32	-3.16	-5.55	2.51

8. Signature Name: VEGETATED AREA INCLUDING THE MARSHES

Number of Points = 96

Band	PC1	PC2	PC3	PC4	VI	T3	B5
Minimum	96	154	124	127	250	27	76
Mean	101.18	164.18	129.93	129.10	254.95	38.46	80.27
Standard	2.19	4.32	2.03	0.66	0.51	6.37	1.69
Maximum	107	174	134	130	255	53	84

Covariance Matrix

PC1	4.78						
PC2	5.13	18.66					
PC3	2.45	7.28	4.13				
PC4	0.56	0.88	0.47	0.44			
VI	0.22	0.53	0.15	0.06	0.26		
T3	-0.83	-1.10	0.97	-0.28	-0.29	40.60	
B5	1.45	-3.65	-1.70	0.02	-0.04	-0.82	2.86

4.7. Evaluation of Sample Statistics

In the evaluation process, several methods have been used to make sure that the selected samples are representatives of all the classes. Together with quick look and ellipse used to evaluate on the display and contingency matrix, statistics, divergence matrix, signature distance (euclidean) formed part of the activity at this stage.

As the findings of the evaluation indicate the samples have been found to confirm the representativeness of the selected pixels for each category (see tables below)

Table 4.7a Image Classification Contigency Table

Maximum Likelihood Classifier

Signature Name	Scoriaceous Basalt		Obsidian		Scoriaceous Por.Basalt		Pum & Ash Group-I	
Scoriaceous Bas.	0	0.0%	0	0.0%	0	0.0%	8	14.3%
Obsidian	0	0.0%	0	0.0%	0	0.0%	0	0.0%
Scor.Por-Basalt	0	0.0%	0	0.0%	4	19.0%	11	19.6%
Pum.& Ash Gr-I	42	100.0%	7	25.9%	17	81.0%	37	66.1%
Por.Alk-Basalt	0	0.0%	0	0.0%	0	0.0%	0	0.0%
Trachytic Rocks	0	0.0%	0	0.0%	0	0.0%	0	0.0%
Pum.& Ash Gr-II	0	0.0%	0	0.0%	0	0.0%	0	0.0%
Vegetated	0	0.0%	20	74.1%	0	0.0%	0	0.0%
Total Points	42		27		21		56	

cont.

Signature Name	Por.Alkali Basalt		Trachytic Rocks		Pum.& Ash Group-II		Vegetated	
Scoriaceous Bas.	10	30.3%	0	0.0%	2	12.5%	0	0.0%
Obsibian	0	0.0%	0	0.0%	0	0.0%	0	0.0%
Scor.Por-Basalt	12	36.4%	6	40.0%	0	0.0%	0	0.0%
Pum.& Ash Gr-I	11	33.3%	9	60.0%	13	81.2%	0	0.0%
Por.Alk-Basalt	0	0.0%	0	0.0%	0	0.0%	0	0.0%
Trachytic Rocks	0	0.0%	0	0.0%	0	0.0%	0	0.0%
Pum.& Ash Gr-II	0	0.0%	0	0.0%	1	6.2%	0	0.0%
Vegetated	0	0.0%	0	0.0%	0	0.0%	96	100.0%
Total Points	33		15		16		96	

Table 4.7b Signature Separability Table

Distance Measure: Transformed Divergence

Using Bands:PC1 PC2 PC3 PC4
VI T3 B5

Taken 6 at a time

Class	(weight/Total Weight)
1 Scoriaceous Basalt	0.125
2 Obsidian	0.125
3 Scoriaceous por.Basalt	0.125
4 Pumice and Ash Gr-I	0.125
5 Por. Alkali-Basalt	0.125
6 Trachytic Rocks	0.125
7 Pumice and Ash Gr-II	0.125
8 Vegetated Area	0.125

Best average Separability using
Transform Divergence

Bands	Average Minimum	Class Pairs:						
		1:2	1:3	1:4	1:5	1:6	1:7	1:8
		2:3	2:4	2:5	2:6	2:7	2:8	3:4
		3:5	3:6	3:7	3:8	4:5	4:6	4:7
		4:8	5:6	5:7	5:8	6:7	6:8	7:8
PC1 PC2 PC3	2000 2000	2000	2000	2000	2000	2000	2000	2000
PC4 VI T3		2000	2000	2000	2000	2000	2000	2000
B5		2000	2000	2000	2000	2000	2000	2000
		2000	2000	2000	2000	2000	2000	2000

Best Minimum Separability
Using Transform Divergence

Bands	average Minimum	Class Pairs:						
		1:2	1:3	1:4	1:5	1:6	1:7	1:8
		2:3	2:4	2:5	2:6	2:7	2:8	3:4
		3:5	3:6	3:7	3:8	4:5	4:6	4:7
		4:8	5:6	5:7	5:8	6:7	6:8	7:8
PC1 PC2 PC3	2000 2000	2000	2000	2000	2000	2000	2000	2000
PC4 VI T3		2000	2000	2000	2000	2000	2000	2000
B5		2000	2000	2000	2000	2000	2000	2000
		2000	2000	2000	2000	2000	2000	2000

Table 4.7c Signature Euclidiean Table

	Scoriaceous Basalt	Obsidian	Scoriaceous Por.Basalt	Pumice & Ash Group-II
Scoriaceous Bas.	0.00	68.25	46.72	138.15
Obsidian	68.25	0.00	95.39	177.21
Scor.Por-Basalt	46.72	95.39	0.00	98.52
Pum.& Ash Gr-I	138.15	177.21	98.52	0.00
Por.Alk.-Basalt	75.15	137.58	48.81	102.37
Trachytic Rocks	84.70	142.28	48.26	73.48
Pum.& Ash Gr-II	81.60	143.57	58.38	85.79
Vegetated	88.04	64.73	110.64	165.32

cont.

	Porphyrtic Alkali-Basalt	Trachytic Rocks	Pumice & Ash Group-II	Vegetated Area
Scoriaceous Bas.	75.15	84.70	81.60	88.04
Obsidian	137.58	142.28	143.57	64.73
Scor.Por-Basalt	48.81	48.26	58.38	110.64
Pum.& Ash Gr-I	102.37	73.48	85.79	165.32
Por.Alk.-Basalt	0.00	29.55	34.90	149.87
Trachytic Rocks	29.55	0.00	28.26	146.91
Pum.& Ash Gr-II	34.90	28.26	0.00	140.59
Vegetated	149.87	146.91	140.59	0.00

Distribution of the eight spectral classes DN value in all ERDAS bands (PC1, PC2, PC3, PC4, VI, T3, B5) is shown in figure 4.7a and 4.7b. In the figure the DN distribution for the classes in PC1 and VI is almost identical, therefore, to avoid redundancy of information, we neglected VI from the GIS image. Texture image is the most informative band among the enhanced data and it is added to the GIS image as a principal component of the colour composite. Next to texture image,

Landsat TM band 5 has an appreciable contribution to the contrast of the colour composite image.

In general, classes that are overlapped, grey tone ranges of every spectral classes in every ERDAS bands and separability of different spectral classes in a particular band is well depicted in fig.4.7a and 4.7b. In fig.4.7b PC1, VI, T3, and TM band 5 show maximum separability between different classes. Due to this PC1, T3 and B5 are chosen for final classification.

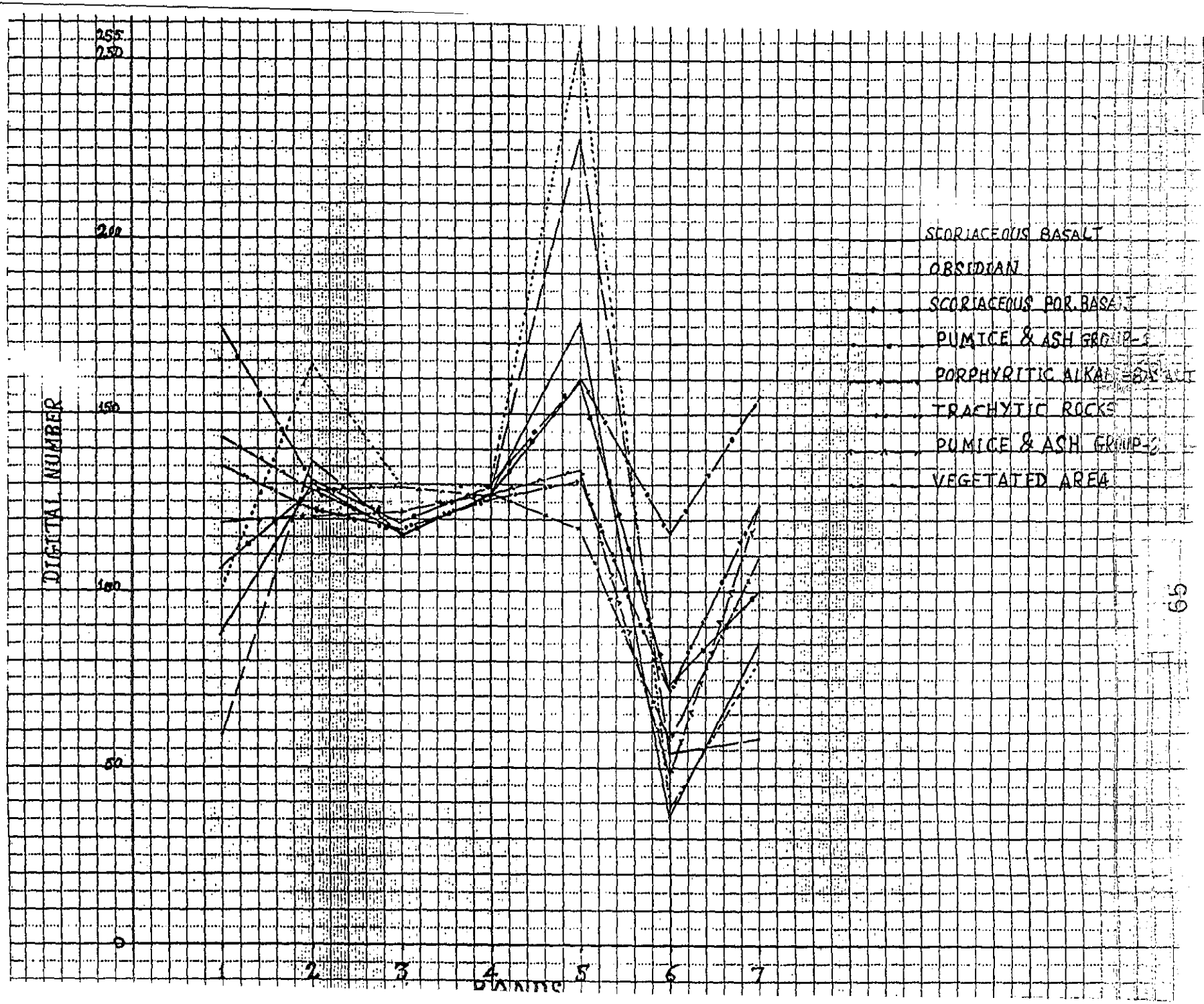
255
250
200
150
100
50
0
DIGITAL NUMBER
1
2
3
4
5
6
7
BANDS
SCORIACEOUS BASALT
OBSIDIAN
SCORIACEOUS POR. BASALT
PUMICE & ASH GROUP-1
PORPHYRITIC ALKALI-BASALT
TRACHYTIC ROCKS
PUMICE & ASH GROUP-2
VEGETATED AREA

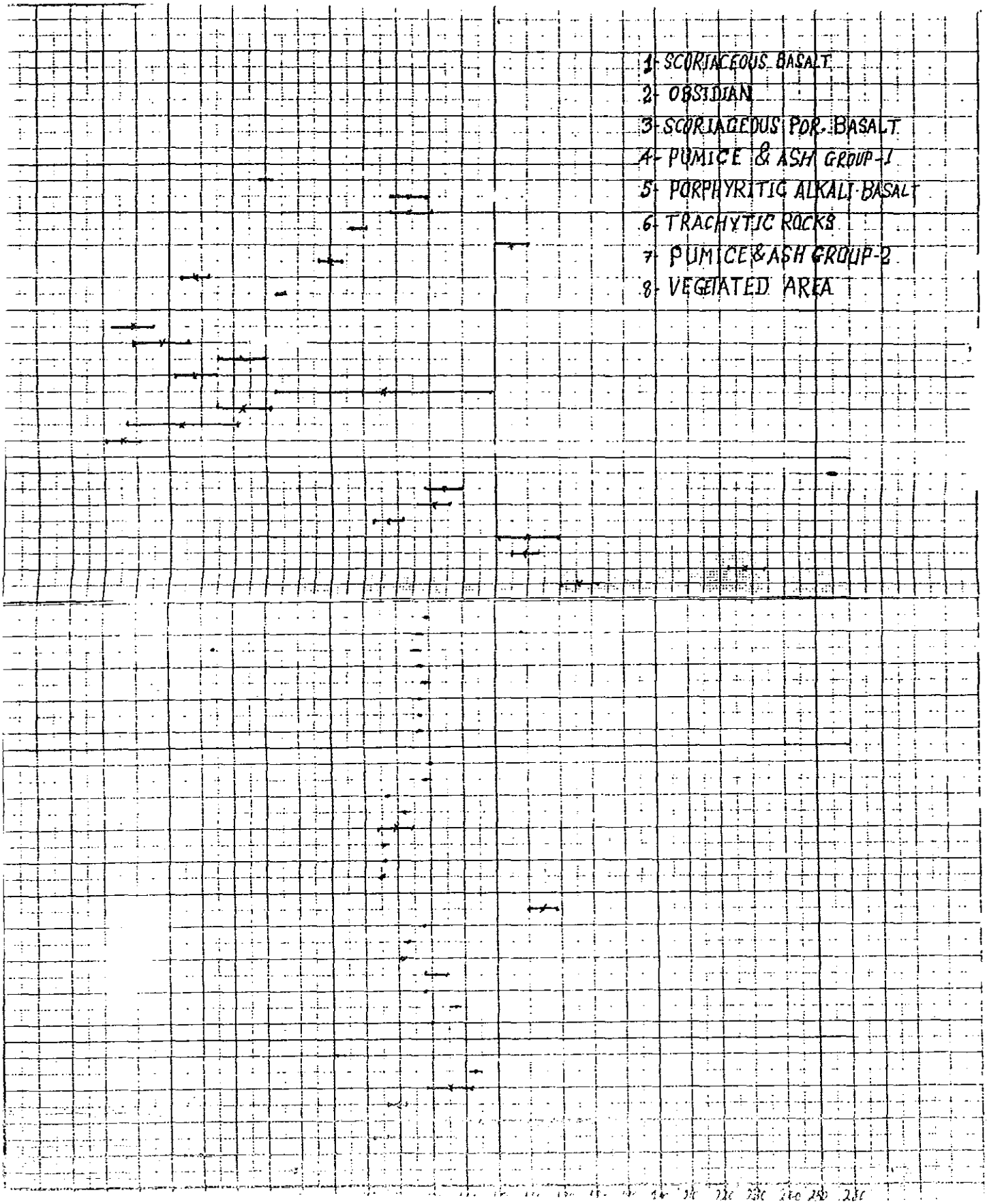
1- SCORIACEOUS BASALT
2- OBSIDIAN
3- SCORIACEOUS POR. BASALT
4- PUMICE & ASH GROUP-1
5- PORPHYRITIC ALKALI BASALT
6- TRACHYTIC ROCKS
7- PUMICE & ASH GROUP-2
8- VEGETATED AREA

4.8. Classification

Having carefully investigated the statistics of the samples the classification stage followed. The most informative combination on which classification had been run is PC1, Raito image of TM band 3 and 5 and B5 in RGB order. Here the major activity was being the selection of an algorithm of classification that satisfies the desired goal among the available ones.

To meet the objective of this thesis project, as detected by the training histograms the decision rule employed to classify the pixels laying outside the sample pixels categories is the maximum-likelihood classification rule.

The area of study contains 1950 columns and 1288 rows that has been submitted to this decision rule. The resultant output, that is the classified map, initially comprised seven spectral-lithologic classes. However, for reasons mentioned earlier concerning the difficulties inherent in digital classification for geological application improvements on the output have been deemed necessary.

4.9. Post Classification

At this stage of the process, Three major activities has been accomplished. One is editing the output map so as the classes obtained on the basis of the training statistics

matches with the field information and the other ones are geometric correction and rectification.

4.9.1. Editing

Here the output map has been manipulated using a program called GIS EDIT. This program gives the analyst the opportunity to carry out changes, particularly, to part of a class or classes that is/are thought to be included into a class/ classes it doesn't/they don't belong to. In this respect part of the class categorized as scoriaceous basalt have been removed from this class and has been appended into obsidian. Not only removing part and adding into a class it is supposed to belong to has been possible but removal of sporadic noises within the same class also has been affected.

4.9.2. Geometric Correction and Rectification

Like in any Remote Sensing data, Geometric distortion in the TM data requires correction. To this effect about 33 ground control points (GCP) have been selected on both the image and Topo-Map (table 4.9a).In the process of GCP selection the maximum precaution has been taken in order to avoid the mismatch of points on the images and the Topo-Maps, and to maintain uniformity in the distribution of these points.

The correction proceeded with first order of transformation and Root Mean Square error (RMS) at 2.5. The result obtained indicates that about half of the total GCP have been correctly identified that the output GIS map has been corrected with these points involved (see table 4.9b).

Table 4.9a Selected GCP from both the Image and the Topo Maps

Point count	point number			Image Pixels	
		X	Y	X	Y
1	1	478030.0000	895065.0000	317.00	834.00
2	2	476015.0000	892075.0000	252.00	987.00
3	3	472094.0000	888025.0000	174.00	1140.00
4	4	489087.0000	896045.0000	707.00	797.00
5	5	493073.0000	893020.0000	856.00	879.00
6	6	485085.0000	892095.0000	599.00	919.00
7	7	492020.0000	889018.0000	829.00	1025.00
8	8	478050.0000	908080.0000	252.00	415.00
9	9	480035.0000	900075.0000	353.00	684.00
10	10	499020.0000	905065.0000	991.00	403.00
11	11	495075.0000	897085.0000	941.00	688.00
12	12	488095.0000	901005.0000	673.00	627.00
13	13	484018.0000	897070.0000	499.00	769.00
14	14	502085.0000	909030.0000	1094.00	276.00
15	15	506055.0000	910040.0000	1214.00	218.88
16	16	508080.0000	906015.0000	1272.00	313.00
17	17	506055.0000	903053.0000	1255.00	456.00
18	18	514058.0000	905048.0000	1524.00	354.00
19	19	510020.0000	911015.0000	1342.00	174.00
20	20	501053.0000	894065.0000	1078.00	832.00
21	21	501095.0000	887075.0000	1181.00	1033.00
22	22	525045.0000	908045.0000	1877.00	193.00
23	23	524020.0000	903085.0000	1862.00	357.00
24	24	521058.0000	902050.0000	1781.00	414.00
25	25	525060.0000	898085.0000	1937.00	517.00
26	26	524055.0000	894040.0000	1927.00	681.00
27	27	515060.0000	892020.0000	1625.00	808.00
28	28	513070.0000	886069.0000	1591.00	1008.00
29	29	510080.0000	885000.0000	1493.00	1080.00
30	30	517035.0000	885030.0000	1718.00	1035.00
31	31	514065.0000	878065.0000	1656.00	1281.00
32	32	510090.0000	879025.0000	1527.00	1280.00
33	33	511060.0000	881060.0000	1527.00	1197.00

order of transformation is 1

-0.1136493E+02 0.3442622E+02
 0.3456042E-01-0.4778941E-02
-0.5398150E-02-0.3494055E-01

These are the computed results of the above matrix:

Point Count	Point Number	Image X pixel	X pixel Residual	Image Y pixel	Y pixel Residual
1	1	324.29	0.7292E+01	867.68	0.3368E+02
2	2	270.79	0.1879E+02	981.78	-0.5216E+01
3	3	157.14	-0.1686E+02	1142.03	0.2032E+01
4	4	701.14	-0.5864E+01	780.60	-0.1640E+02
5	5	855.22	-0.7764E+00	867.25	-0.1175E+02

Table 4.9b Finally accepted Ground Control Points.

Total RMS error= 1.43398

Point Count	Point Number	Error	Error contributed by point
1	8	1.6958	1.1826
2	2	1.5506	1.0813
3	26	0.9814	0.6844
4	33	1.3467	0.9392
5	17	1.4915	1.0401

Here are the points that were used:

Point Count	Point Number	X	Y	Image Pixels X	Y
1	8	478050.0000	908080.0000	252.00	415.00
2	2	476015.0000	892075.0000	252.00	987.00
3	26	524055.0000	894040.0000	1927.00	681.00
4	33	511060.0000	881060.0000	1527.00	1197.00
5	17	506055.0000	903053.0000	1255.00	456.00

Number of control points= 5
Maximum acceptable RMS error 2.00000

4.9.3. Rectification

The purpose of rectification is to assign brightness values in the case of the original data or colour code in the case of classified output map. Since the selection is done on the GIS map the resampling technique employed is the nearest neighborhood. This resampling technique considers the nearest pixel (cell) code for the point under consideration.

5. IMAGE INTERPRETATION AND MAPPING

5.1. Image Interpretation

The purpose of this study is primarily to map lithology and lineaments that are found in the study area using methods of Remote Sensing. In Remote Sensing the most important task next to image processing is interpretation of the processed images in the desired sense. Among the images used during the study, TM false colour composites both classified and unclassified are found to be more informative for lithologic mapping.

However, the maximum lithologic contrast study was obtained from false colour combination of TM band 5 in red, and enhanced images principal component 1 (PC1) in green and ratio of Tm band 5 and 3 in blue. In the chapter for image processing, the statistical relationship among these bands is discussed (see fig.4.7a and 4.7b). Supervised classification was run carefully on a colour composite (Fig.5.1a) which was simplified to geological map of the area (Fig. 5.1b). As a result of classification , nine spectral classes that correspond to types of lithology and landcover features found in the area are established.

Class 1: Scoriaceous Basalt

Class 2: Obsidian

Class 3: Scoriaceous Por. Basalt

Class 4: Pumice and Ash Group-I

Class 5: Porphyritic Alkali Basalt

Class 6: Trachytic rocks

Class 7: Pumice and Ash group-II

Class 8: Vegetated Area

Class 9: Water body

Class 1. Scoriaceous Basalt

As it will be discussed with class 3, this group of basalt is a subdivision of the youngest scoriaceous porphyritic basalt found on the rift floor. The subdivision is mainly based on reflectance differences and statistical results. However, no clear difference was observed during field survey, it is somewhat reddish brown in colour and has scoriaceous texture. During petrographic analysis almost no phenocrysts are found except for the presence of few feldspar crystal laths in a glassy groundmass.

The occurrences of the basalt is restricted to the zones that are affeted by the youngest deep penetrating faults and fractures of Wonji Fault Belt. Its flow is damed by young fault scarps striking NNE with throws ranging from

by young fault scarps striking NNE with throws ranging from 2m to 15m. On the surface the basalt is found surrounded by the scoriaceous porhyritic basalt and it covers 2.16% of the area.

Class 2. Obsidian

This class is named obsidian, because obsidian contributes more than half of the signature for this class. It covers 2.66% of the area. Among the rocks included in the class; different varieties of glassy rocks such as obsidian, pitchstone, perlite and pumiceous glass, and dark grey ignimbrite and greyish ash domes are the dominant ones. The Sensor categorization is mainly based on similarity in the mineralogical composition of the rocks in the class.

In the outcrop level, the class is distinctly represented by obsidian domes, flows and fragments of juvenile magma associated to pumice and ashes of class 4 and trachyte of class 6. It is mainly found along active fault zone through which it had been poured out.

On the TM map this class is found overlapped with the reflectance from shadows of steep fault scarps, crater rims and deeper valleys. This anomalous overlapping in reflectance of two different rock bodies is minimized by running filter programmes, band rationing (band 5 - band 3)/(band 5 + band 3) and by changing the standard deviation of the classes

based on field data. Usually when such problem happens in classification, the thermal infrared band is used for further spliting or subdividing the overlapped zones into subclasses based on heat capacity differences. For this study it was not possible to extract band 6 from the original data. So band 6 is not involved to overcome the problem.

From petrographic point of view, as mentioned earlier the rocks grouped in this class differs only in texture and structure. Their mineralogical composition is more or less similar.

Class 3. Scoriaceous Porphyritic Basalt

This class is further subdivided in to scoriaceous basalt (class 1). Its distribution is logical and pocket outcrops of the rock is pinpointed by the Sensor. It covers 3.98% of the study area. It has no spectral overlap with the other classes except with its subdivision class 1.

The rocks in this class are mainly exposed at the periphery of scoriaceous basaltic flows of class 1 found at the southern part of the area mainly within the marshy grabens such as Shetemata and Harakelo. The boundary between class 1 and 3 is hardly identified during field mapping, but with the Sensor digital data the computer put clear and distinct boundary between the two classes. This is one of the

for defining lithologic contacts.

The petrographical differences between class 3 and class 1 are mainly based on phenocryst content, colour and texture. Class 3 has darker colour and contains mainly phenocrysts of feldspars. It forms sheets of flows with rolled edges pahoehoe and banked against fault scarps. While basalt of class 1, is scoriaceous with brecciated surface (aa-lava) and reddish brown in colour.

Class 4. Pumice and Ash Group-I

Rocks included in this class are tuffs and pumiceous ignimbrites, pumice and ash falls and flows, and very few alluvial and lacustrine sediments that are dominated by pyroclastic rock fragments (volcaniclastic sediments).

It is the most widely distributed class and covers 34.67% of the study area. The spatial distribution of this class shown on the satellite map positively correlates with the results of field survey and aerial photo interpretation. The outcrop of this class dominates in the western and northwestern of the study area filling the depressions, grabens and mantling flat -lands. It is outcropped in the area as pumice domes and ridges, and rift floor pyroclastic flows and falls, which attain the maximum thickness in the

locality between the foot of Mt. Bora and lake Ziway and the vicinity of mount Bora. This is because, the source for the pyroclastics is the eruption of Bora and the surrounding volcanoes. Some of the lacustrine sediments surrounding lake Ziway are included in this class, due to their similarity in reflectance that is resulted from similar mineralogical and chemical compositions with the other rocks categorized in the class.

Parts of the pumice domes and ridges dissected by faults and erosion show difference in reflectance, and hence classified wrongly as different classes. In the field checking procedure it was found that these differences in reflectance are not due to compositional or lithological variations between the rocks outcropped in the gulleys and those on the bare ridge, but are due to shadows of steep cliffs and higher EMR absorpition of dense vegetation in the gullys. Shadow of craters rim associated with differences in intensities of vegetation in the craters such as Tulu Moye and Bora Craters contributed to the interference (spectral overlap) with the other classes. These pockets of signatures of other classes were proved to be noises during field observation and their effect is minimized by applying similar techniques of enhancement applied for class 2.

Class 5. Porphyritic Alkali Basalt

It is the thickest and most extensively distributed basalt, covering 9.81% of the total study area. It includes all varities of porphyritic alkali basalts of different sources in the area. Since it has been affected by the faulting, it is outcropped on fault scarps, cliffs, horsts and in the grabens as continues lava flow with pahoehoe- lava structure. It seems to dominate in the southern central part of the area occupying mainly the horsts.

The top part of the basalt is affected by weathering and hence mapped as soil cover with rocks in class 7 and insignificant proportion is included in class 2. Despit this, very few spectral overlaps, as confirmed by the statistical analyses shown in fig.4.7b and field observation it has no any other interference with the rest classes.

In general, the three basalt classes displayed on the satellite map are classified based on their spectral differences resulted from diversity in texture, structure and composition that might be indirectly related to their age and magmatic history.

The petrography of the basalt in this class will be discussed in the next chapter.

Class 6. Trachytic Rocks

This class is named trachytic rocks, because it includes

rocks that have similar reflectance to trachyte as a result of similarity in mineralogical composition and texture. The rocks grouped in this class are trachyte, some rhyolite and ignimbrites that are grey to greenish in colour. It covers 8.04% of the area and found scattered within the area.

This class has considerable spectral overlap with classes 4,5 and 7, and therefore needs further analyses using TM band 7 (reflected infrared) and band 6 (thermal infrared) to map rhyolites, ignimbrites and trachytes separately. But for the reason mentioned earlier it was not possible to make further interactive image processing to enhance the lithologic contrast among these rocks. The only solution was to reduce the standard deviation of the class and map the lithology based on the sample point selected from the dominant rock type (trachyte) in the group.

The rock types included in this class are found as lava flows, domes, ridges, cliffs and caldera rims.

Class 7. Pumice and Ash Group-II

This group is a subdivision of class 4 based on degree of lithification, surficial weathering effect and secondary processes. Spatially, it is widely distributed next to pumice and ash in class 4, and covers 20.51% of the total area. It mainly includes pumiceous ignimbrites, tuffs, hardened ash layers and some soils derived from rhyolithic flows,and

pumice and ash falls.

In the statistical evaluation process of the different classes present in the image, it was not possible to subclassify this class into smaller classes that have approximately closer DN values.

5.2. Image Analysis

1. False colour composite of TM band 5, 3 and 2 in RGB order.

Band 5 (Red) is associated to basalts of class 1, class 3 and class 5, and some acidic lava flows such as the southern obsidian domes (class 2) which is highly vegetated. Band 3 is represented by green colour which is highly associated to the pyroclastic deposits. Blue for Band 2 is linked to the obsidian dome at Jano (class 2).

Plate 5.2a. False colour composit of TM band 5, 3, and 2 in RGB order.

In this image class 1 (C1) scoriaceous basalt has similar reflectance with the obsidian dome found south of it, therefore it is not possible to map class 2 (C2) and class 1 (C1) separately using this colour combination. It enhanced the similarity in vegetation types that are growing on the two different bedrocks rather than lithology.

The trachytic domes represented in the image by C6 show better contrast from the surrounding rocks and they are partly mapped from the contribution of this colour combination.

The scoriaceous porphyrtic basalt (C3) found at the frontal part of the scoriaceous basaltic (C1) flow is also relatively enhanced.

The two obsidian domes (C2) located at the top of the image are different from the bottom main obsidian dome only due to the difference in intensity of alteration and vegetation cover, there are no as such manifestated lithological or mineralogical differences between them.

2. False colour composite of TM band 2, 5 and 3 in RGB order.

Plate 5.2b False colour composite of TM band 2, 5 and 3 in RGB order.

In this combination the scoriaceous basalt (C1), Scoraceous porphyrtic basalt (C3), porhyritic alkali basalt (C5), pumice and ash group-I (C6) are distinctly identifiable. Especially C4 and C6 shows better contrast as compared to the surrounding lithology.

The most widely distributed porphyrtic alkali basalt (C5) is well detectable with its flow direction in this colour combination. The variegated colour for this class is due to

different reflectance that comes from altered and fresh parts of the basalt (see Plate 6.1.4c).

3. False colour composite of principal component 1, 3 and 4 in RGB order.

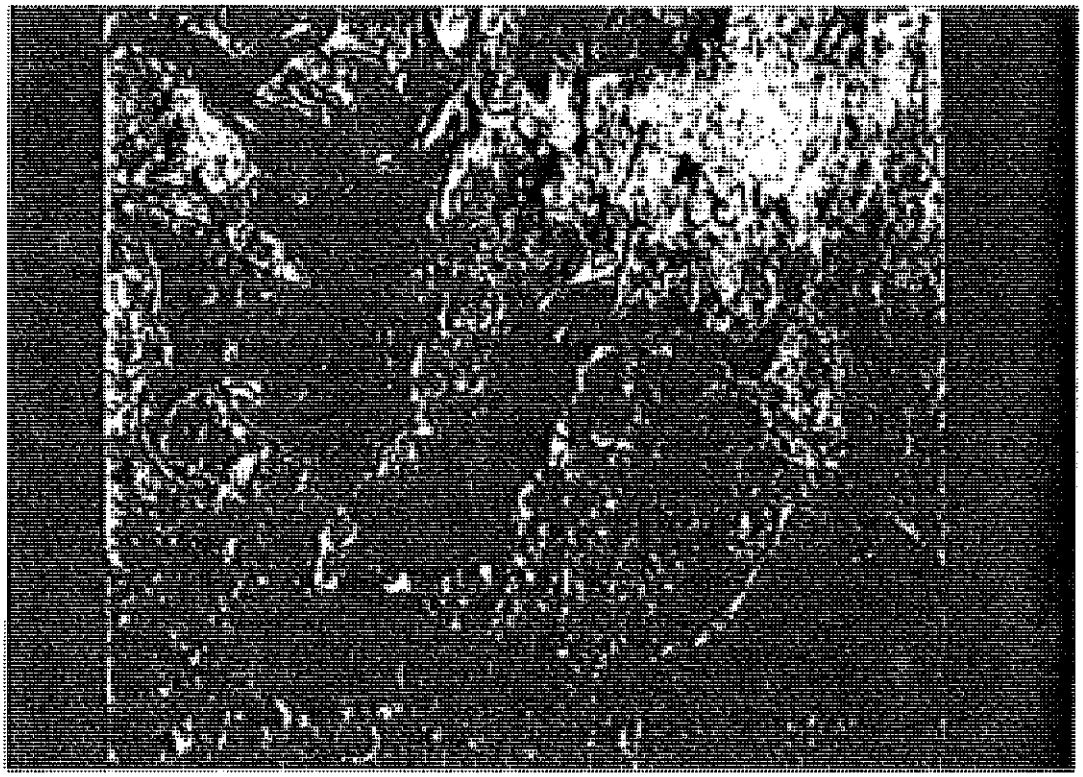

Plate 5.2c False colour composite of principal component 1, 3, and 4 in RGB order.

In this enhanced data false colour composite, the distribution of class 2 (C2), class 5 and class 7 is well traced, mainly the three obsidian domes which were recognized previously as different rock bodies are mapped in this image as similar rocks.

The distribution of class 4 within class 7 is also enhanced as compared to the previous combinations.

The spatial distribution and stratigraphic relation of class 7 with the other classes is also understandable from the flow relationships. Class 5 (porphyrtic alkali basalt) is older than the faults that cut it, and the scoriaceous basalts and obsidian flows that has poured out through these faults. Therefore C5 is older than C1, and C1 in turn is older than C2.

4. False colour composite of PC1, TM band 5 and PC4 in RGB order.

Plate 5.2d. False colour composite of PC1, TM band-5 and PC4 in RGB order.

This colour combination is constituted of interactively

enhanced and geologically most informative bands. Therefore, it emphasizes on the discrimination of silicic rocks such as trachyte, rhyolite, obsidian, pumice and ashes. As a result it was possible to map C2, C4, C6 and C7 distinctively and separately from this colour combination.

5.Single TM band 5 (near infrared) image in black and white.

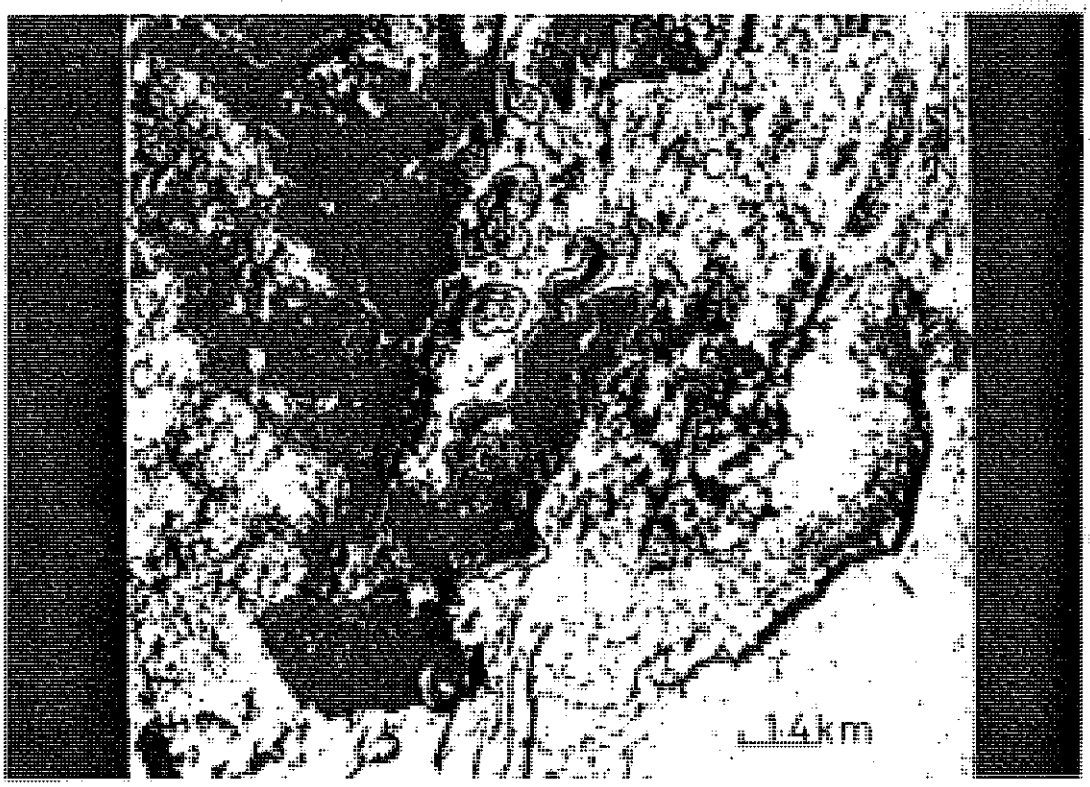

Plate 5.2e. Single TM band-5 (near-infrared) image in black and white.

This image emphasizes particularly on the distribution of trachyte and obsidian domes because of their distinctive flow structure. It therefore, gives substantial information in mapping the silicic lava flows that show well preserved

flow structures. It also magnifies the linear structures more than the previous images.

Eventhough the image is displayed in black and white, all the classes established in this study are distinctly mappable using grey tone level differences. Therefore, based on the mean of DN values for each spectral classes found in this single band image the following interpretation is given.

Class	Representative rock type	Average DN value	Grey tone contrast
C2	Obsidian	58	dark
C1	Scoriaceous Basalt	85	dark grey
C3	Scor. Por. Basalt	100	grey
C5	Por. Alkali Basalt	109	light grey
C6	Trachyte	124	cloudy
C7	Pumice & Ash Group-II	124	cloudy
C4	Pumice & Ash Group-I	155	bright

6. Band ratio (band 5 - band 3)/(band 5 + band 3) in black and white.

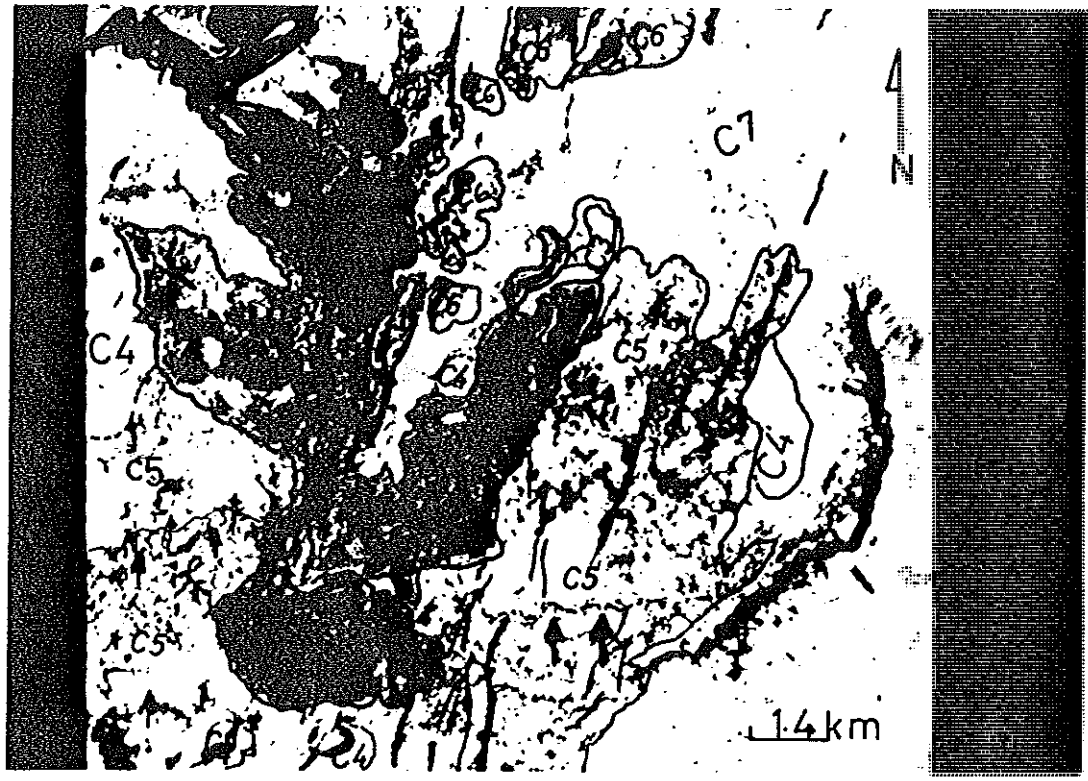

Plate 5.2f. Band ratio (Band5 - band3)/(band5 + band3) in black and white.

As explained in the chapter for Image Processing, ratio image has the most important role in mapping the lithology of the study area.

In this image the two obsidian domes found in the northern part of the test area are connected with the southern bigger dome with a ridge composed of obsidian associated with ash and pumice cones.

Using this image it is also possible to locate the source region for the lava flows by tracing the flow direction as indicated by the arrows. Hence, the source for the lava flows younger than the porphyritic alkali basalt (C5) is the fissures that trend NNE and found partly covered by the lava flows. But, the source for the porphyritic alkali basalt is a bit far to the south near Tulu Moye.

7. High-pass (7x7) Laplacian filter on TM band 5 image in black and white.

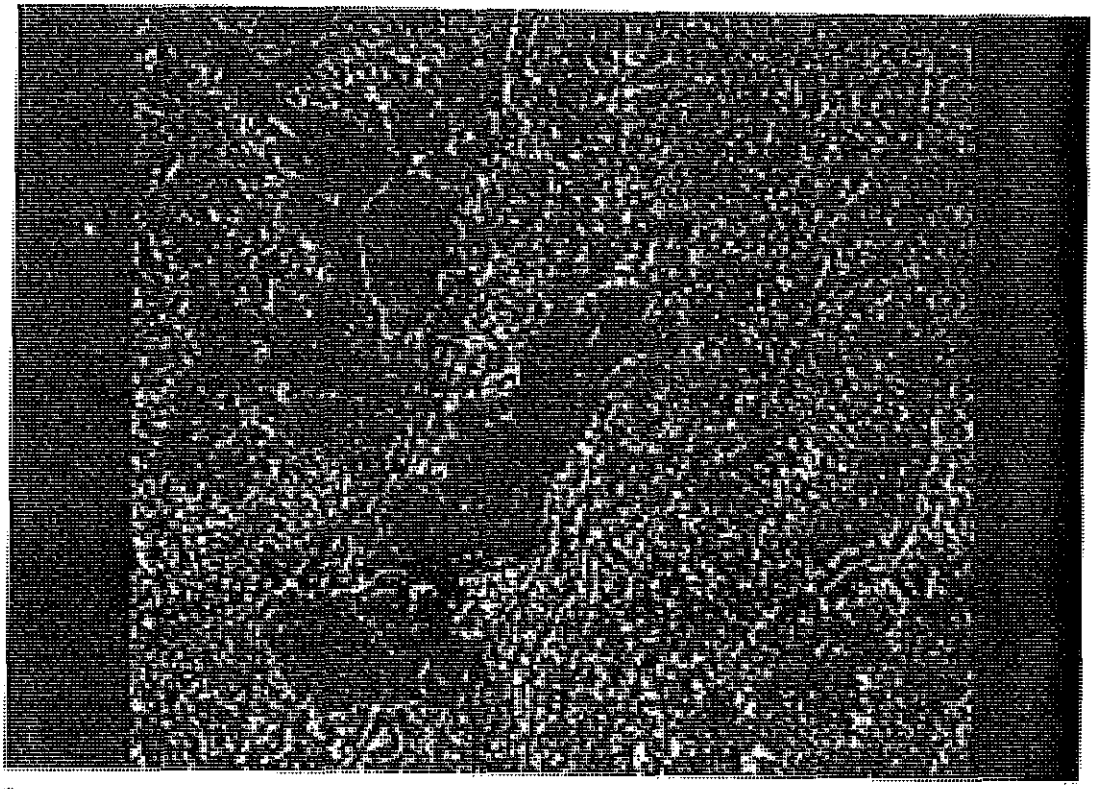

Plate 5.2g. High-Pass (7 x 7) Laplacian filter on TM band-5 image in black and white.

The main objective of filtering the image was to enhance lineaments and lithologic contacts found in the study area. Therefore, the smaller faults cutting the recent obsidian domes and ridges are well enhanced in the image, and the major faults found in the rift floor as well. The flow structures in the obsidian and trachytic domes are also revealed in the image.

6. GEOLOGICAL FIELD STUDY OF THE AREA

The study area totally falls within the central part of the complex structural system of the Main Ethiopian Rift. The overall lithology comprises lava flows and pyroclastics belonging to the "Nazreth series" and "Wonji series" of Meyer et al. (1975) and rift floor lacustrine sediments of Neuman (1902), Baci (1940) and Mohr (1962,1966). The volcanic rock types found in this area are ignimbrites, rhyolites, welded and unwelded tuffs, pumice deposits, basalts and trachytes. Among the sedimentary rocks, conglomerates, sandstones and mudstones of lacustrine origin are common ones. The sedimentary rocks are found near Lake Ziway underlying the tuffs from mount Bora.

6.1.1. Local Stratigraphy

The succession of the rock units outcropping in the area, from the youngest to the oldest respectively can be summed up as follows:

9. Pumice and ash unit
8. Obsidian flow unit
7. Rift floor scoriaceuos basalt unit
6. Trchytic flow unit
5. Rift floor pyroclastic unit

4. Rift floor porphyritic basalt unit
3. Shorima escarpment porphyritic olivine basalt unit
2. Co-Ignimbrite breccia and ignimbrite of Tulu caldera
1. Main escarpment pyroclastics unit

1. Main Escarpment Pyroclastic Unit

The overall stratigraphy of the study area is characterized at its base by rift related starts with the pyroclastics outcroping upper part of the MER eastern escarpment. This pyroclastic series in consists of greenish crystalline ignimbrite near the bottom and, ash and pumice interlayering towrards the top (figure 6.1a and 6.1b).

This pyroclastic series is well observed at the foot of the main rift escarpment east of town Huruta and in the river valleys flowing along the escarpment. The dominant rock type in the locality is a greenish and highly welded lithic ignimbrite.

The ignimbrite exposed at a fault scarp at about 2km east of the town Huruta is very compact and contains comparatively thin layers of ash. It forms a steep wall about 15m high across the river Wedecha (see plate 6.1.1a). The bottom part of this ignimbrite is grey to green in color and contains lithics, glassy fiamme, and crystals. In the lithic fraction

pumice, rhyolite, and other volcanic rock fragments are observed. At this locality the amount of crystals in the ignimbrite seems to dominate over the other components. It is less welded near its top and grades upwards into tuff with more pumice fragments.

This greyish green Ignimbrite is conformably overlain by a thick pumice fall unit which contains interbeds of well sorted and thinly laminated ash layers. The contact between the pumice and ash layers is discernible in plate 6.1.1b that shows one of the exposures.

The unconsolidated pumice fall unit above the ignimbrite contains fine grained lithics and shows normal grading near its top. The vertical relation among the pyroclastic fall units at the outcrop is shown in plate 6.1.1b, and its thickness reachs about 12m.

The pyroclastic fall unit above the Ignimbrite includes a paleosol horizon of thickness about 25cm near the bridge on Boru river. The thin paleosol horizon within the pumice and ash intercalation zone is found exactly at the top of an ash fall (plate 6.1.1c). The presence of this paleosol horizon within the pyroclastic fall succession indicates that, the succession is not the result of a single phase of eruption. Near its top part, the pumice fragments in the pyroclastic fall unit becomes finer and finer and,

finally pass into ash which inturn is consolidated to a yellow tuff with larger (about 20cm) size pumice fragments close to its top.

The pyroclastic unit, at the top, ends with an ash layer partly altered to soil that has mantled most of the cultivated fields between the main fault scarp running parallel to Keleta river and a second fault scarp found west of Iteya-Gonde road. At the contact between this thick ash-rich soil horizon and the bottom lithics - rich pumice fall, there is a layer of agglomerate of about 10-30cm in thickness cemented by crystalline carbonate. The crystalline cement appears to be derived from subsurface precipitation of carbonate in the form of calcret. It extends all over the area covered by the above pyroclastics association.

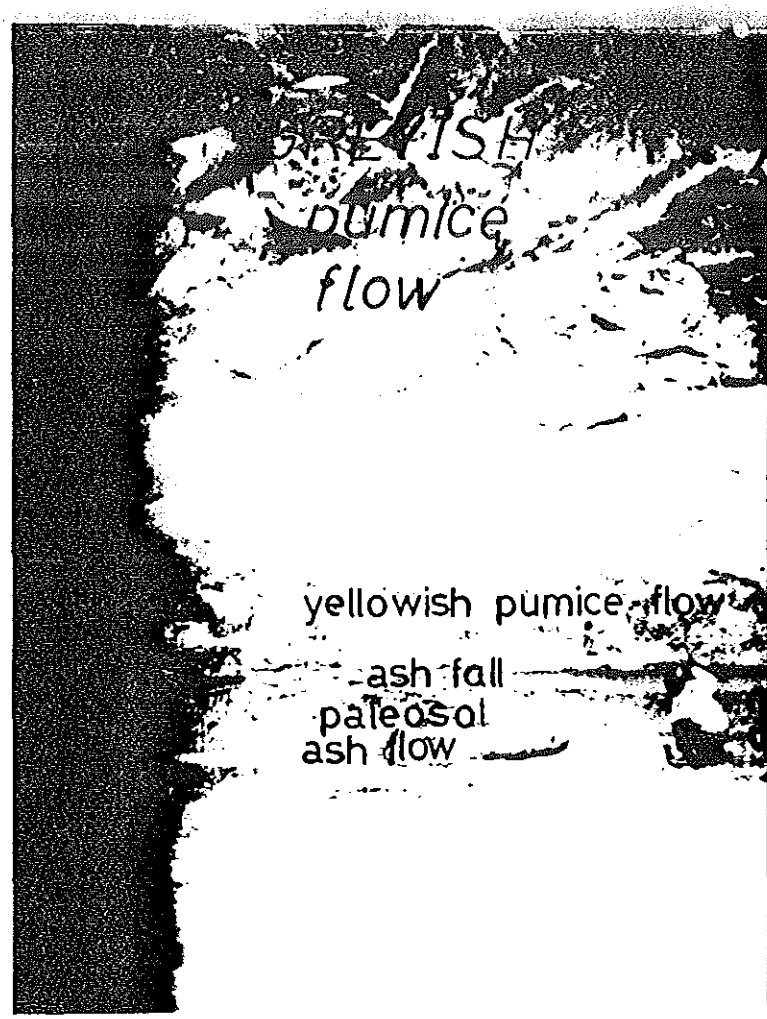

Plate 6.1.1a. Pyroclastic deposits in Wedecha River valley.

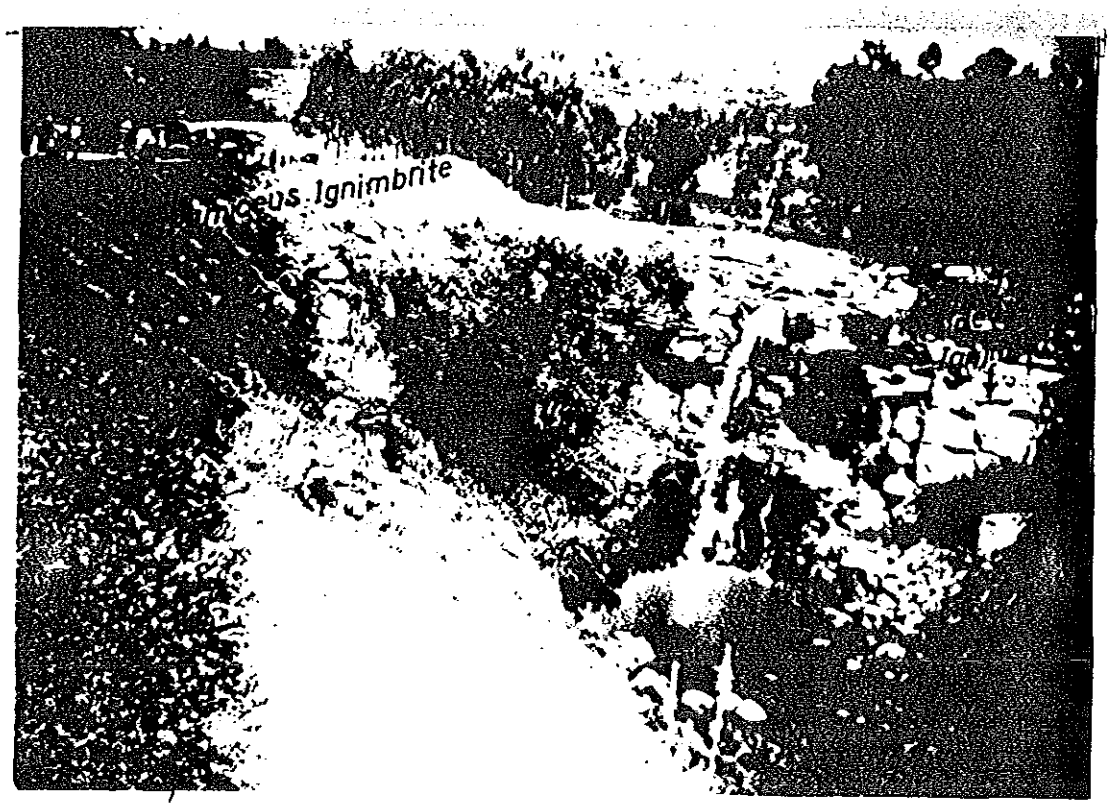

Plate 6.1.1b. The lowest grey ignimbrite forming a waterfall across Wedecha River.

2. Co-ignimbrite Breccia and Ignimbrite of Tulu caldera

These two pyroclastic flows are the result of formation of Tullu caldera. The caldera is the result of collapse with a semi-circular rim preserved. The floor of the caldera is flooded by porphyritic alkali basalt that has been cut by NNE trending faults which oblitrated the western boarder of the caldera.

The representative stratigraphic section from this locality is shown in figure 6.1d. The section shows three lithologic types that are conformably interrelated: Volcanic breccia at the bottom, compact greyish ignimbrite in the middle and white to grey pumice and ash fall layer of thickness greater than 2m at the top.

The breccia is reddish to reddish brown in colour, and is massive in structure except for the presence of thin discordant co-genetic ignimbrite beds. It is relatively consolidated (agglomerate). The thickness of the bed at the locality is greater than 30m and is constituted of volcanic rock fragments including obsidian (both from juvinile magma and the rock fragment), scoria, rhyolites ignimbrites and porphyritic basalt and few intrusive igneous rock fragments. It is characterized by poor sorting and absence of any internal structure and, the size of lithics range from few mm to 40cm. This pyroclastic flow is conformably overlain

by comparatively high temperature product greyish - green Ignimbrite.

The grey - greenish Ignimbrite is highly welded and contains fiamme that reach in length upto 5cm. Petrographically, it contains fractured crystals of anorthoclase and few aegirine. The anorthoclase crystals were fractured during the flowing phase of the pyroclastic flow. The fiamme in the rock is devetrified into different varieties of quartz mainly chalcedony.

Well sorted pumice and ash fall layers overlie the ignimbrite mentioned above. These pyroclastic fall deposits vary in thickness from place to place mainly due the degree of preservation to variation in intensity of erosion. At the locality of the section its thickness exceeds 2 meters.

In general, the lateral extension of these pyroclastic products is highly restricted to their source area and their thicknesses rapidly decrease away from the source.

3. Shorima Scarp Porphyritic Olivine Basalt Unit

This basalt unit is well exposed along a major fault scarp that runs from Gonde river through Shorima to Tulu caldera, striking in a NNE direction. At Shorima fault scarp the thickness of this basalt flow reaches up to 10m. It is overlain by another aphyric basalt flow with the presence of

about 30cm thick agglomerate in between and underlain by pumice and ash deposits derived from Tulu volcano with paleosol of about 30cm thick in between. In thin-section the groundmass and phenocrysts are mainly constituted of olivine, pyroxene and substantial amount of plagioclase feldspar is also present as phenocrysts. Unlike the other basalts found in the study area, this basalt contains no or very few amount of titano-augite.

Concerning its texture, the rock is porphyritic with larger phenocrysts of plagoclase and olvine, and groundmass that can be completely identified through microscope. Due to its similarity in mineralogical composition and stratigraphic position with Chilalo basalt (Weldegabriel et al., 1990), the transitional basalt in the area is most likely derived from the same source with Chilalo basalt.

Figure 6.1c shows the stratigraphical relation of the basalt unit with the adjacent pyroclastics and basalts at Shorima fault scarp.

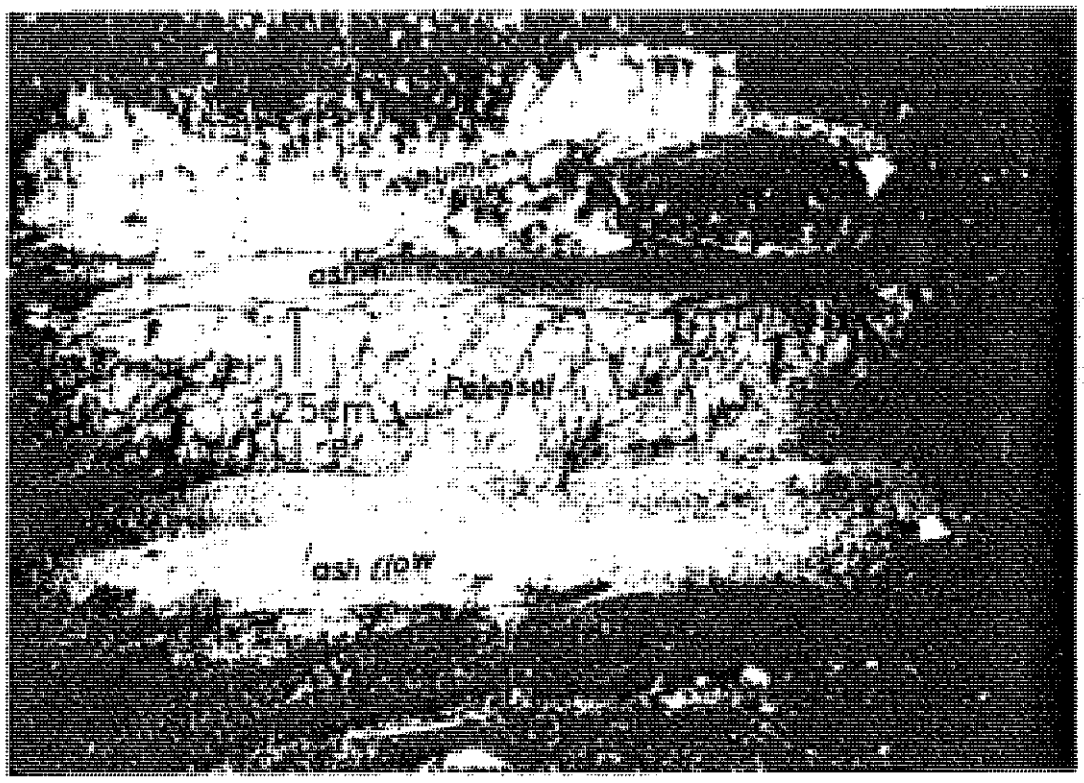

Plate 6.1.1c. Different pyroclastic layers with the paleosol in Wedech River valley.

4. Rift Floor Porphyritic Basalt Unit

The Rift floor Porphyritic basalt is the most widely distributed type of basalt in the study area. It is exposed in almost all grabens and horsts within the studied sector of the rift floor. The thickness of this rock unit reaches upto 40m at a fault scarp near Anole village (see Plate 6.1.4a. and figure 6.1e). The basalt unit is cut by axial rift faults, and is, therefore, older than these faults The flow

formed bridge like landform that has transversally connected two adjacent fault scarps of a graben.

From the bottom to the top of the basalt section structural and textural variations are observed. Among the variations; the bottom part of the basalt flow lacks vescicles. It is highly porphyritic and sheet flows overlapping one another with irregular contacts are found.

The central part of the section is characterized by reddish to reddish brown cinder like basalt with chilled fronts (plate 6.1.4b). The amount of phenocrysts found in this zone is less than in the bottom and top zones.

The top part of the unit is full of vescicles, both of primary and secondary origin. The primary vesicles are the result of escaping of gas and fluids in the process of cooling. The secondary ones are voids left after removal of plagioclase feldspar and olivine phenocrysts by the action of surface weathering and splashing by surface water. The secondary pores are very few and mainly observed on the surface of the rock.

Both primary and secondary vesicles are partly refilled by precipitated calcium carbonate giving amygdaloidal texture to the rock and partly by clay minerals resulting from alteration of plagioclase feldspar and olvine phenocrysts (see plate 6.1.4c).

Handspecimen comparison, indicates that the size, shape, type and distribution of phenocrysts in this unit is similar to that in the basalt flow unit underlying it. However, in thin-section there are important differences in the amount of olvine in both phenocryst and ground mass fractions. Olivine is more abundant in the underlying basalt, while the amount of titano-augite is higher in the upper basalt.

From petrographical investigation it is observed that, almost all of the phenocrysts in this basalt are made up of very coarse grained crystals of plagioclase feldspars with few titano-augite, olivine and rutile needles. The plagioclase, olivine and pyroxene crystals are highly altered with olivine characterized by idingitization rims.

The groundmass is made up of abundant crystal laths of mainly plagioclase feldspars with very few olvine and pyroxene. In general, the mineral association in the groundmass and phenocryst is similar to that of a mildly alkaline basalt commonly described in the Ethiopian Rift.

From analysis of flow structures on the ground surface and from imageries, the source area for the basalt is deduced to be related to fissures found near Tulu Moye. On the basis of petrographic composition, the basalt appears to be equivalent to "porphyritic feldspar basalt of Tulu Moye" described by Di Paola's (1976) .

Plate 6.1.4a. Porphyritic alkali basalt section exposed by one of the youngest rift faults.

5. Rift Floor Pyroclastics

This lithological rock group is represented by a thin layer of about 1m pumice and ash fall overlying the alkali basalt and outcroping in the northeastern part of the study area. It is well developed at the locality of mount Bora and its proximity. The best outcrop of these pyroclastics is observed at Ula Arba ridge, which is in the same physiographic belt with mount Bora.

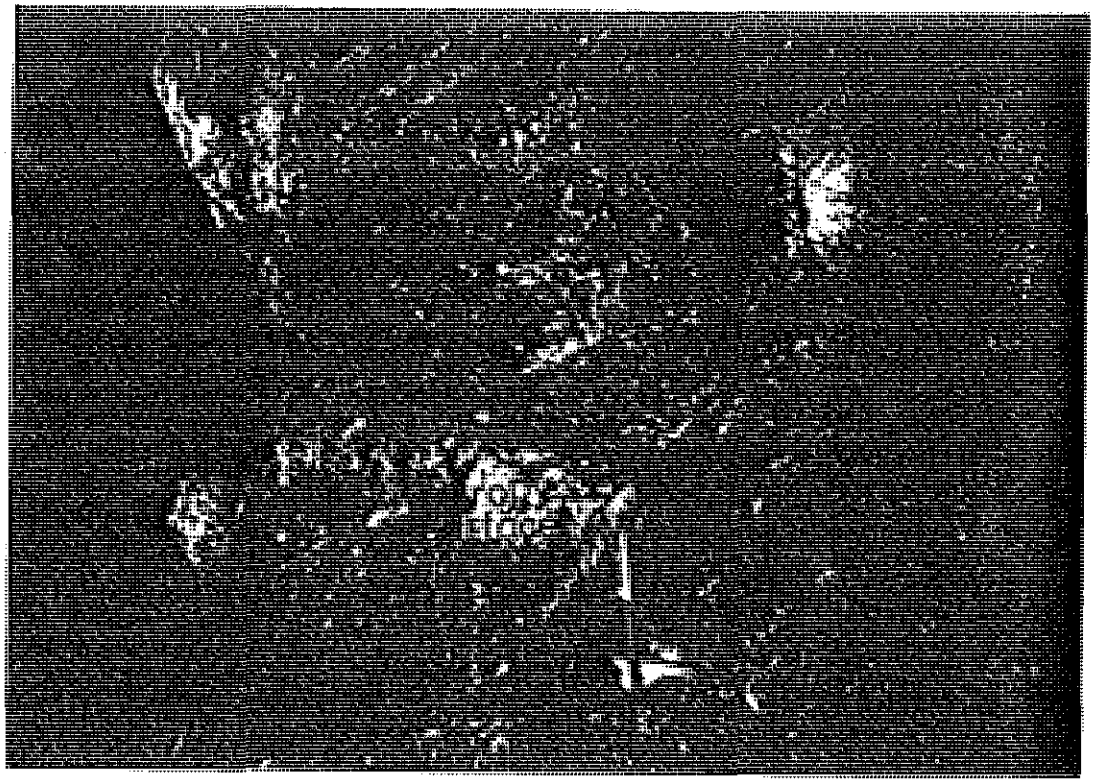

Plate 6.1.4b. The middle part of an outcrop of the porphyritic alkali basalt showing ropy surface and chilled fronts.

From the analysis of the drainage pattern, density, texture and tone of analog images of Mount Bora and its surrounding, it is deduced that the exposed rocks in the area are mainly constituted of coarse grained unwelded pyroclastic products.

At Ula Arba an outcrop of intercalated pumice and ash units more than 17m in thickness is exposed. The outcrop as a whole is made up of unconsolidated pyroclastic flows and

falls (see plate 6.1.5a). It extends upto Ogolcho under a thin cover of scoriaceous basalt near Tulu Riae (fig.6.1h). The basalt flow extends upto lake Ziway as discontinuous patches of flows.

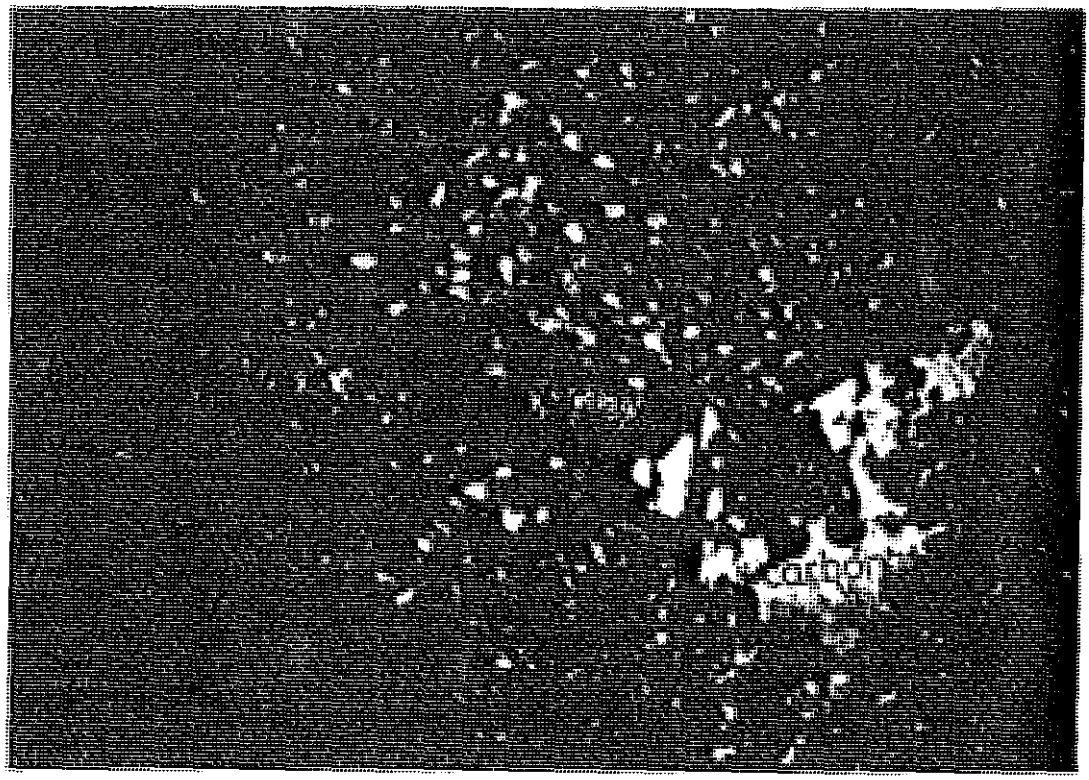

Plate 6.1.4c. An outcrop Showing alteration (X) and secondary precipitation (Y) on the surface of the upper part of the porphyritic alkali basalt.

The Stratigraphic succession (fig.6.1i) at Ula Arba terminates with a 7m thick pumice flow at the top. The pumice flow is characterized by poor consolidation

and massive structure. Underlying the pumice flow, there is a well sorted ash fall layer which reaches upto 40cm in thickness. The colour of this ash fall layer varies from light to dark grey. Underlying the ash fall another pumice flow, characterized by a higher content of angular obsidian fragments, is present. The thickness of this second flow is about 4m. Underlying this second ash layer there is a zone in which pyroclastic fall layers alternate. The alternation is between thin layers dominated by pumice fragments and layers dominated by obsidian fragments (plate 6.1.5b). These layers range in thickness from millimeter size to 2cm and they are not well sorted. The overall thickness of this alternation zone is about 1.5 meters.

The most bottom pyroclastic layer at this section is constituted of less sorted and laminated pumice fall (plate 6.1.5c) rich in obsidian content as compared to other pumice layers at the top. The bottom contact of the lowest bed is not exposed hence it was not possible to measure its exact thickness. The angular obsidian fragments found in the pyroclastic fall deposits are partly derived from brecciation of previously formed obsidian layers near the vent by later phases of pyroclastic erruption. The other source for the angular obsidian fragments is the chilling of acidic lava by the direct contact with ground water while ascending through the vent. The obsidian fragments formed by the second

mechanism contain some phenocrysts of quartz and feldspars.

According to the work of Bill Morton, 1978, the town Meki is built on lacustrine sediments and volcanic tuff. To the east of Meki, mount Bora and mount Berichiya have a wide variety of volcanic rocks: rhyolite, obsidian, pitchstone, basalt, and tuffs and agglomerates.

All theses rocks are well detected by the Satellite according to their spectral similarity with rocks outcropped in the the sample areas.

6. Trachytic Flows and Domes

Trachytic domes are found at Tirbocha and its neibouring domes and entirely made up of trachytic lava with well preserved flow structures typical of acidic lavas. The structures consists of cave- like openings on the flanking surfaces of the ridges and troughs formed by the lava flow. The trachytic occur in the field both as sheeted flows and hemispherical domes. They have been extruded as thick, and viscus lava with dome like or mushroom shapes (forexample Tirbocha dome) or artichoke, piling up over and around the vent. The ratio of the horizontal diameter to the overall thickness of the domes is close to 1 and then assume a hemispherical shape.

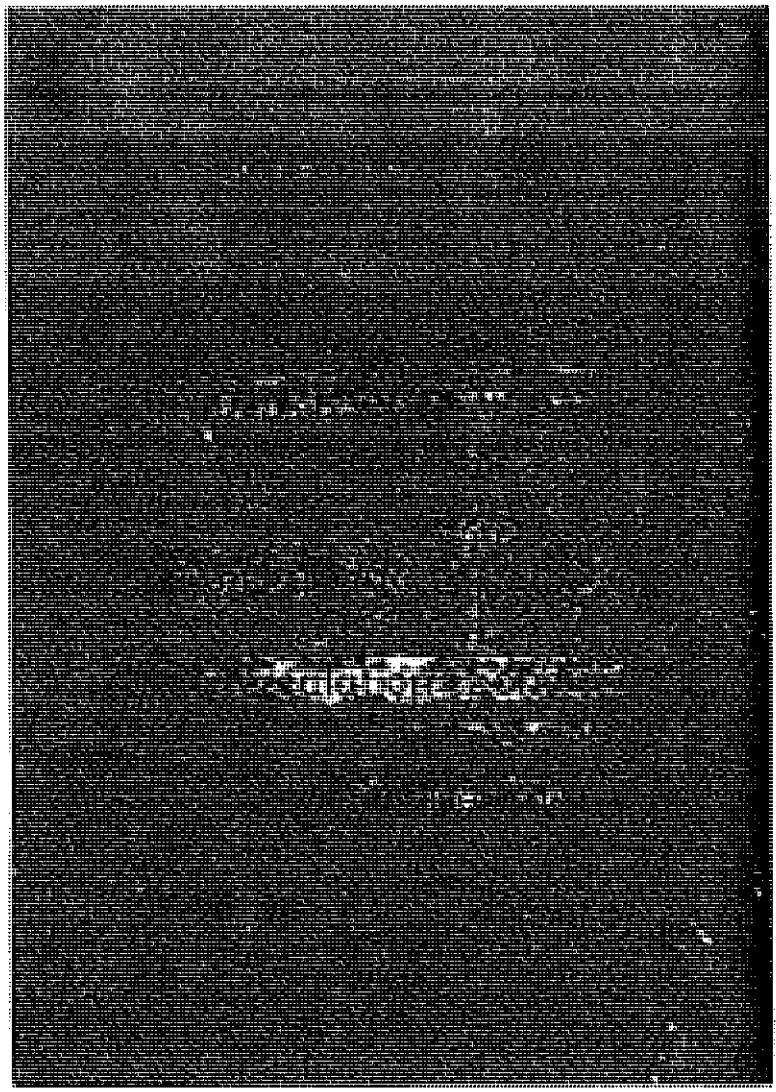

Plate 6.1.5a. A Pyroclastic section at Uìa - Arba. Most of the trchytic domes contain relatively more felsic minerals as compared to the trachytic lava flows, which are rich in mafic mineral content both in their groundmass and phenocrysts.

Trachytic lava has also been extruded through deep fissures and faults oriented NNE-SSW. Flows along these structures

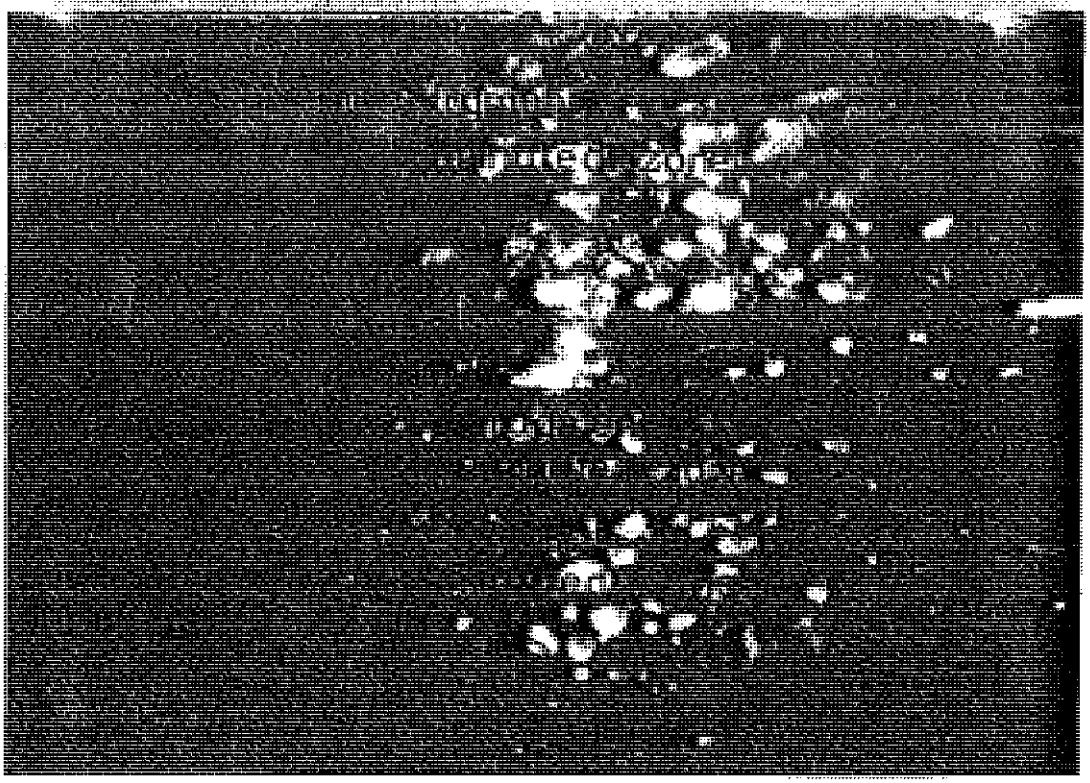

Plate 6.1.5b. Intercalation zone of pumice and obsidian fragments dominated layers.

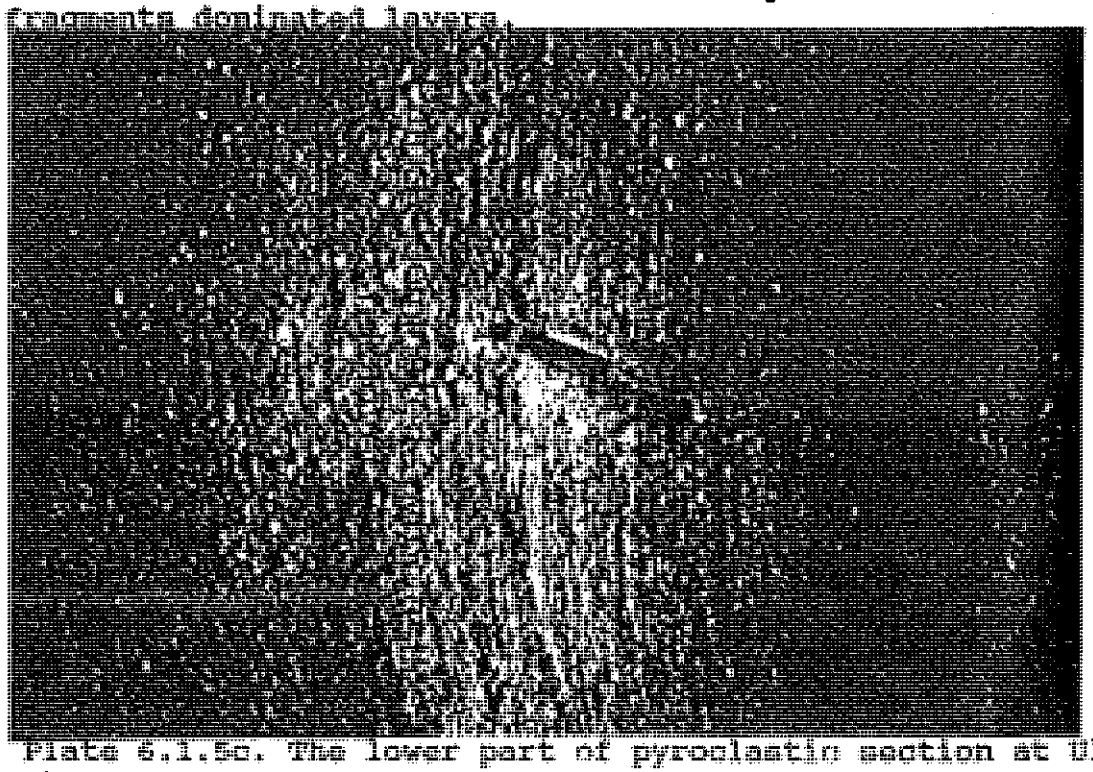

Plate 6.1.5c. The lower part of pyroclastic section at Ula - Arba.

have formed ridges of lava of considerable altitude from the surrounding.

The trachytic lava overlies pumice and ash products emitted both from Bora volcanic complex and Tulu volcanoe at different places. The trachytic flow terminates against fault scarps that cut through the rift floor porphyritic alkali basalt. Therefore, it is clearly younger than the rift floor alkali basalt. The trachyte underlies ash and pumice deposits extruded from the nearby pumiceous craters, and domes that have either open (such as Moye tuff-ring) or closed top tuff-cones (Mt. Salen) and flat topped domes (Mt. Jima). These domes are mainly composed of pumice mixed with some obsidian and cinder fragments. Where the cinder content dominates over the other components, it forms cinder cones and where pumice dominates, it forms tuff-cones. The pumice and ash deposits are in turn overlain by a scoriaceous basalt unit. The stratigraphic relation among these rock units is shown in figure 6.1e.

The main trachyte outcrop is restricted to the northern part of the study area, where the intensity of faulting and fracturing seems to dominate.

From petrographic point of view, the trachyte contains substantial amounts of euhedral plagioclase and alkali feldspars phenocrysts and fewer aegirin and magnetite

crystals. The groundmass is completely crystallized and no quartz at least in comparable amount with feldspars present in the rock. This difference in content of quartz and feldspars proves as the rock is not rhyolitic in composition.

7. Rift Floor Scoriaceous Basalt

This basalt unit is found as a thin sheet of lava flow with scoriaceous (aa - lava) texture and extruded from fissures. The fissural origin is shown from flow directions observed on aerial photographs and on the surface of the lava flow. At a place called Artu there are thermally active fissures trending N18o-N25o, from which part of the basalt had been poured out. These fissures continue further to the south under an obsidian dome that has extruded lately through the same fracture system. This fissure system is characterized by the presence of aligned geysers which suggest that the volcanism in the area is very young and still active.

In the study area the scoriaceous basalt is exposed as patches of thin flows covering gentle slopes formed of either trachytic flow and porphyrtic alkali basalt or pumice and ash deposits (see figure 6.1e.). There are no observable phenocrysts in the basalt exposed at Artu. However, another basaltic flow that has similar stratigraphic position (see figures 6.1g and h) and lithologic character exposed at

Shetemata, Horna and Deneba contains some phenocrysts and is found as patches forming small dome-like topography and ridges aligned on fractures through which it has been extruded. This lava features reach upto 20 meters in height above the surrounding. These dome-like features are probably formed by the upwelling of pressurized gas accumulated in the lava in the process of cooling.

Petrographically, the basalt flow contains very few corroded phenocrysts of plagioclase feldspars, and rare mafic minerals. It has a glassy groundmass with very few microlites of plagioclase feldspars. This suggests that it is a compositionally evolved or differentiated type of basalt.

8. Obsidian Flow

Obsidian in the form of flow sheet is well exposed at the north central part of the study area closer to pumice and ash domes, and the scoriaceous basalt. It mainly overlies pumice and ash ridges. It is also found as bolbous obsidian lava domes forming reliefs as Mt. Gnyaro and Mt. Jano. These obsidian domes are aligned along fractures from which pumice and ash ridges have been extruded.

The obsidian in the Jano area overlies pumice and ash deposits of Bora group and underlies another thin pumice and ash fall layer which is the top most unit in the area. In

some places where the flow has advanced further from its source, it overlies the scoriaceous basalt and trachyte units. Its stratigraphic relation with the other rock units observed at the outcrop is shown in figure 6.1e.

The obsidian domes show well preserved flow structures that can be even identified on unenhanced satellite image (see plate 5.2e). In between the flows sometimes agglomerate and breccia layers are found. Other varieties of glassy rocks such as pitchstone with phenocrysts of quartz and alkali feldspars, perlite and pumice are present at the upper part of the outcrop. The obsidian dome at Jano becomes fibreous and lighter in weight comparable to pumice, with vitreous luster closer to its top (plate 6.1.8a). This is due to alteration and resulting from interaction between air and magma (lava) in the process of cooling. Particularly, devitrification has changed the unstable constituents of obsidian into stable varieties of quartz.

Within single flow sheets of obsidian domes at Gnyaro, banding constituted by alternation of dark and vitreous laminae and white to light grey colored mineral segregation zone is observed (see plate 6.1.8b).

Using normal optical microscope it was not possible to identify minerals in the chilled part except minor amounts of quartz and K-feldspars that occur as phenocrysts in the light grey coloured zone.

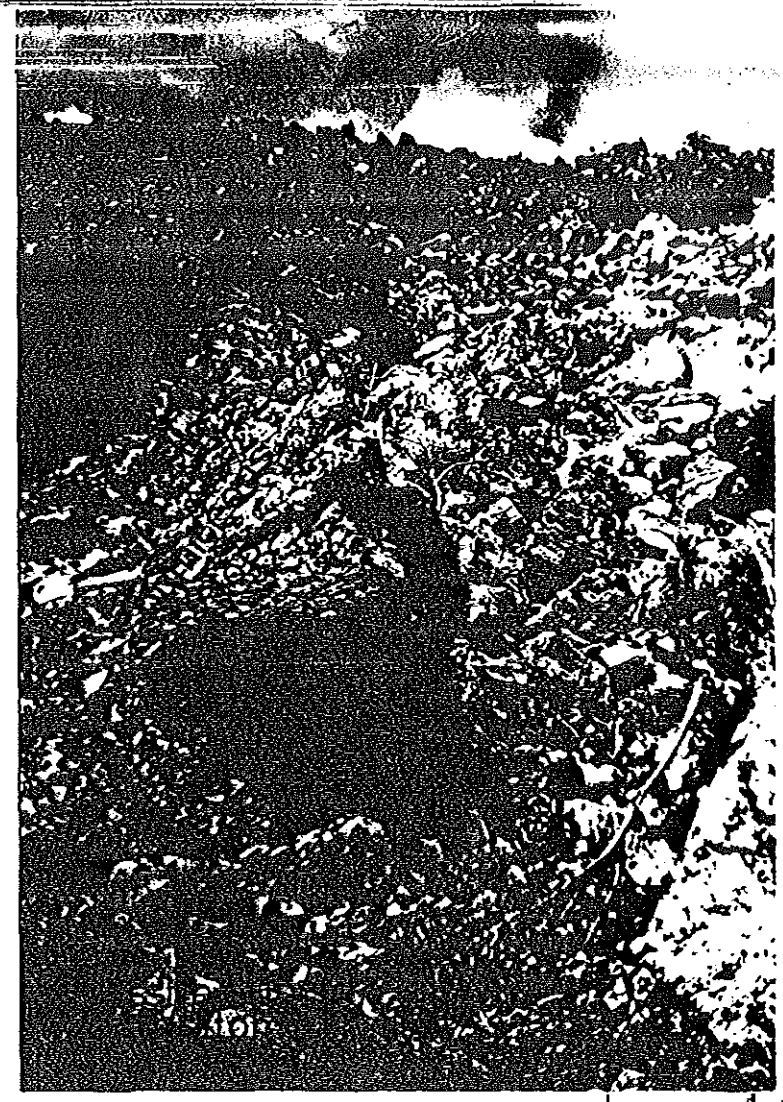

Plate 6.1.8a. The pumiceous top part of obsidian dome at Gano.

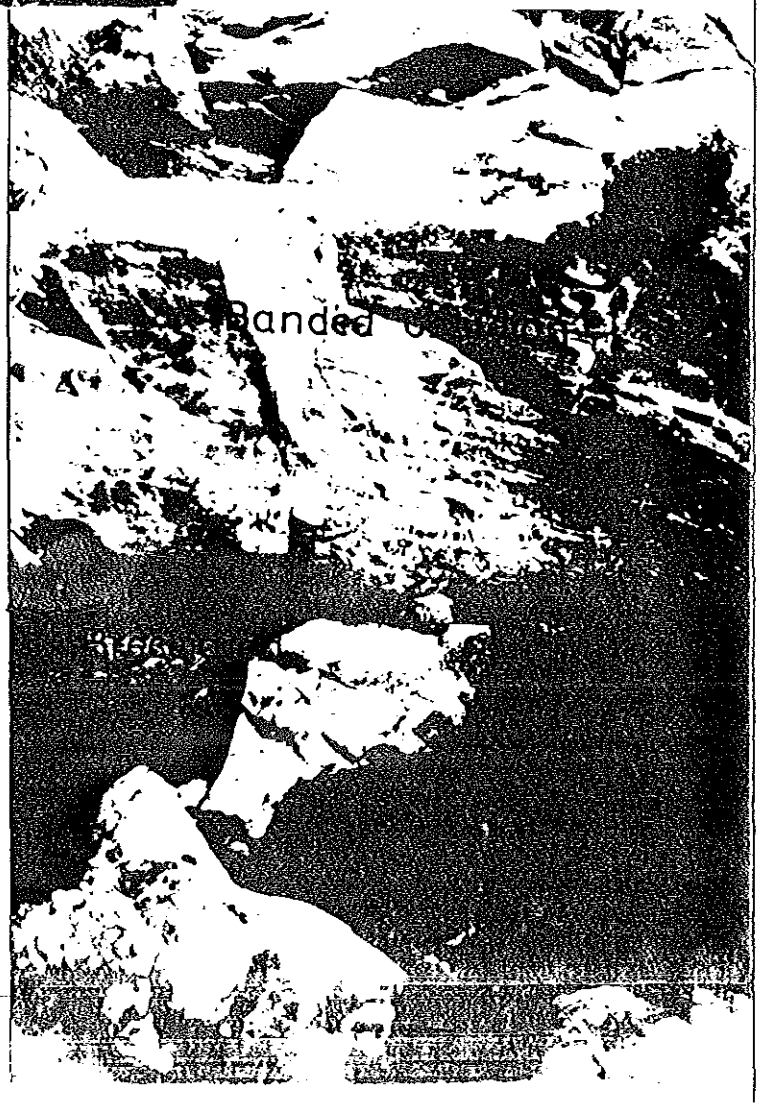

Plate 6.1.8b. Banded obsidian at Gnyaro.

9. Pumice and Ash Fall

This pyroclastic fall unit makes up the topmost part of the rock succession in the study area. It is characterized by interbeding of thin layers of pumice and ash fall, and its overall thickness is about 1m in the area. Texturally, it is well sorted and thinly bedded.

It is difficult to locate with certainty the source area of these products manly due to the following reasons: first, the layer is very thin and almost completely eroded in most places so it is not possible to trace the thickening direction. Second, since it is a pyroclastic fall material, it is also possible that it resulted from an eruption that has occured tens of kilometers away from the study area.

6.1.1. Correlation

Figure 6.1.2a. shows possible local correlation among different rock units observed at different outcrops in the study area.

The general stratigraphic succession of the rock units outcropping in the area can be catagorized into four major lithologic classes. The grouping is based on similarity in lithology and stratigraphic position (Table 6.1a).

Table 6.1a. Generalised Stratigraphy of the Area

Class	Major Rock Units Included in the Class	Common features of the class
Fresh lava flows	Pumice and Ash Falls	Fresh lavas and pyroclastic deposits emitted through W.F B. fissures
	Obsidian	
	Scoriaceous basalt	
Pyroclast-ics and acidic lava flows	Trachyte & Rhyolite	Acidic volcanic products
	Rift - Floor pyroclastics	
Phorphyrit-ic basalts	Rift-Floor Por. basalt	Highly porphyritic basalts
	Shorima Scarp por. basalt	
Pyroclast-ic flows and falls	Co - ignimbrite breccia and ignimbrite related to Caldera	Pyroclastic products
	Main Escarpment pyroclastics	

After establishing the local stratigraphic succession as shown in Table 6.1a, it is necessary to attempt fitting the rock units in the regional stratigraphic framework (Table 6.1b). Using the existing regional stratigraphic chart for the Central Sector of the Ethiopian Rift the age range for the rock units observed in the study area may be inferred directly from the available radiometric ages. Hence, the oldest ignimbrite unit in the study area may be inferred to belong stratigraphically to the so called "Nazreth group". K/Ar age determinations by Morbidelli and others (1975), Juch, (1975), Kunz et al. (1975), Mayer and others (1975), and compiled by W/ Gabriel et al. (1990), an Upper Miocene - Lower Pliocene age has been assigned to the "Nazreth Group" to which the Eastern Escarpment pyroclastics belong.

The porphyritic basalt outcropping at Shorima fault scarp can be tentatively correlated on the basis of lithological similarity and stratigraphic position equivalent with the Chilalo trachyte and trachybasalt (1.6-3.5 Ma) of Middle to Upper Pliocene age. Weldegabriel et al. (1990) state that the Chilalo trachyte series is Pliocene in age and it includes trachytes, silicic rocks, and basalt flows and overly units that belong to either the Shebele trachyte and Butajira ignimbrite or the Nazreth series.

The remaining lithologic units overlying the Shorima basalt in the study area belong to the "Wonji Group". This group consists of diverse Quaternary lavas, pyroclastic rocks, and volcaniclastic strata (younger than 1.6 Ma.) that

are generally confined to the Wonji fault belt along the entire MER (Kazmin 1979).

Table 6.1b. Correlation Chart

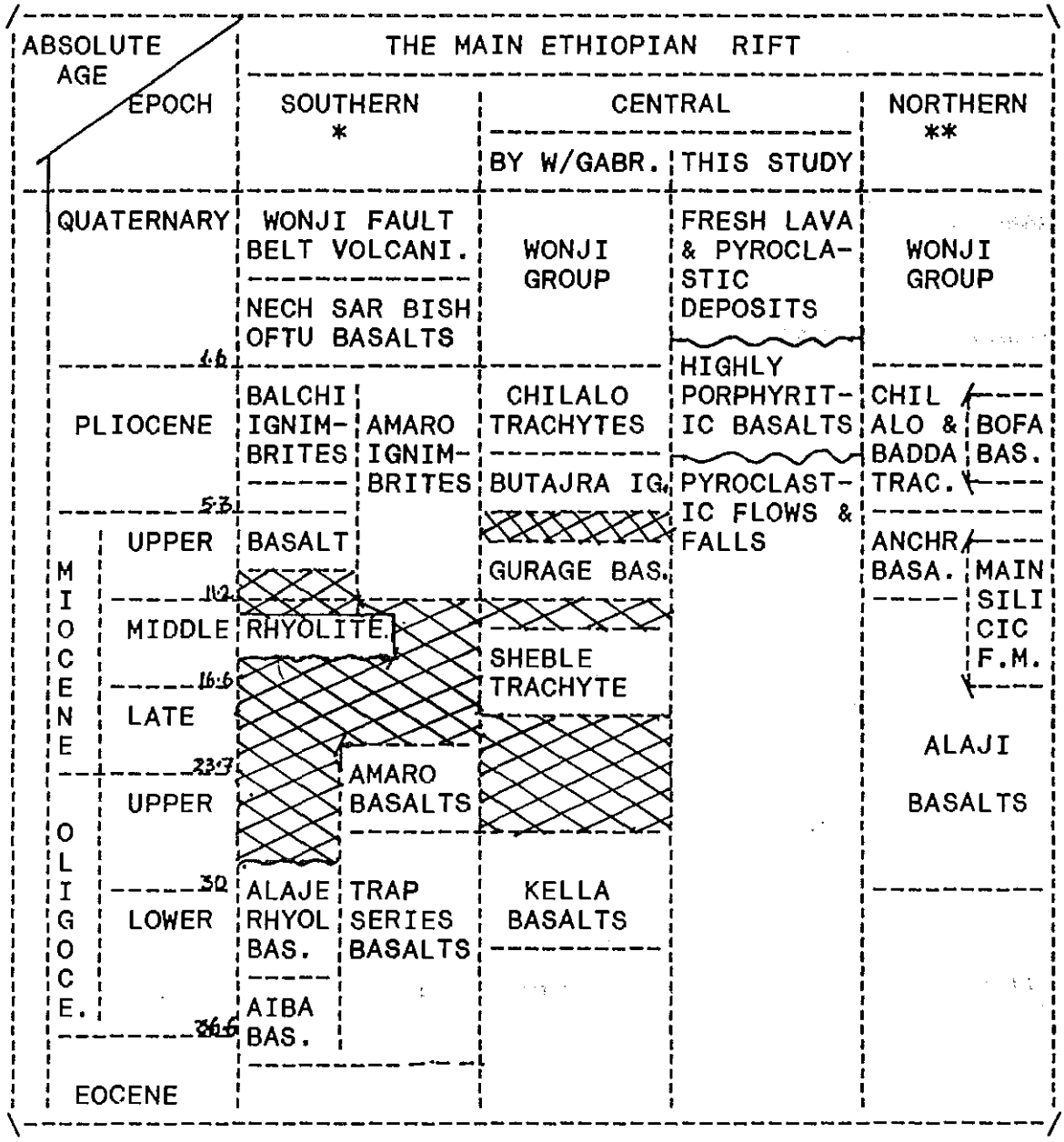

* Levitte and Others, 1974, Zanettin and Others, 1978.
** Juch, 1975, Kunz and Others, 1975, Meyer and Others, 1975, Morbedlli and Others, 1975.

6.2. Geological Structures

6.2.1. Regional Overview

The central sector of the MER is a symmetrical rift, mostly characterized by well defined synthetic rift margins having variable throws along the strike of the boundary faults (Mohr 1967a). These margins are marked by high-angle normal faults with large throws that comprise several step-faulted blocks.

The ESE-WNW Guraghe-Chilalo line (shown in fig.6.2.1) effects a major displacement dextrally off the Main Ethiopian Rift (Mohr 1960, 1966a). The eastern margin curving south wards from Mt. Gugu terminate at Mt. Bada, and resumes some 15 kms to the west at Asela where strong NNE-SSW faulting continues south to form the eastern margin of the rift above lake Ziway and Langano. The north ward continuation of the rift margin faulting at Asela is directly along the Wonji fault belt, which also suffers a small dextral displacement at the Guraghe-Chilalo line. Thus there is shown in figure 6.2.2a an intimate translation between rift-margin and active rift-floor faulting and volcanism. This might be due to the recent oblique rifting associated to the Central Ethiopian

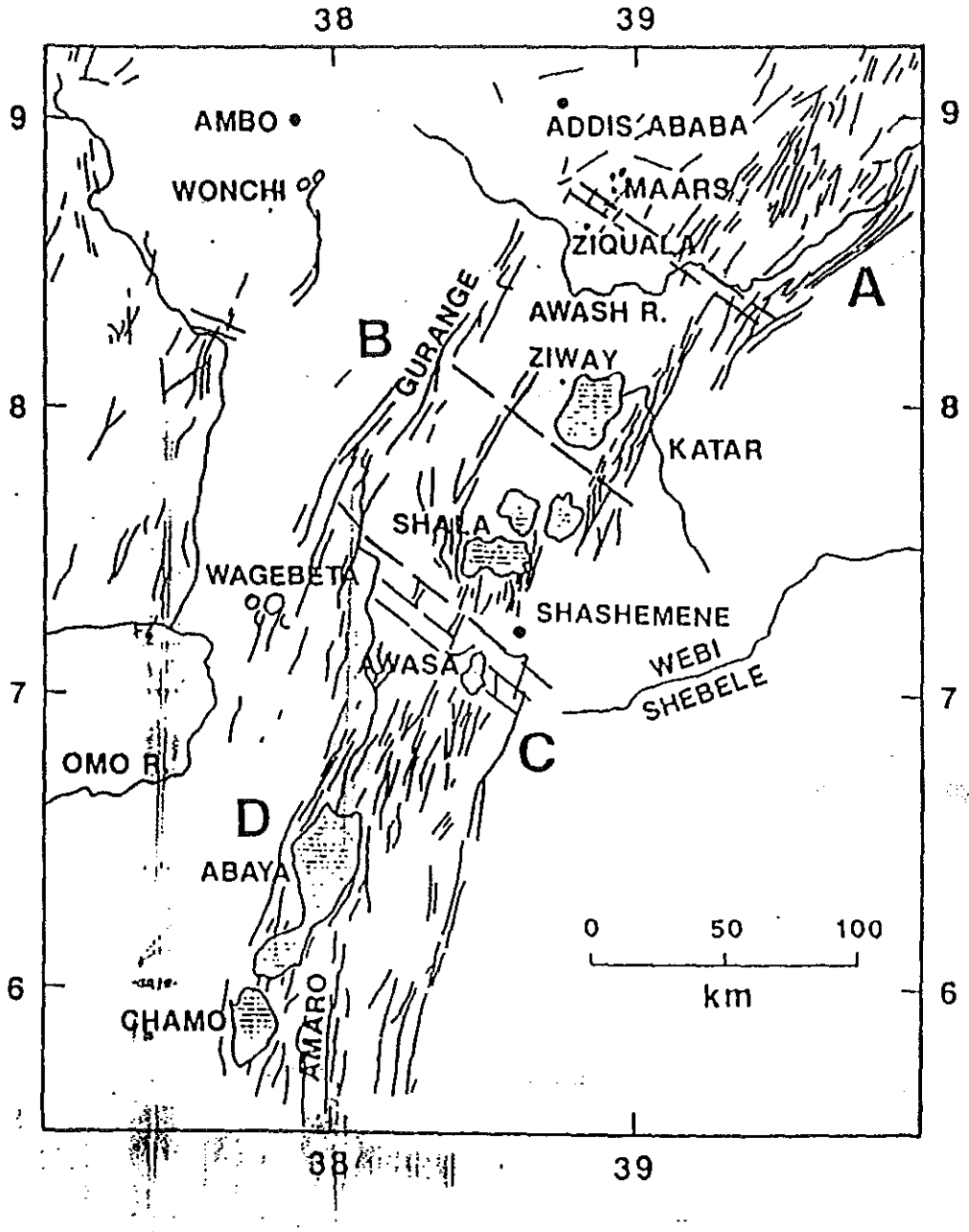

Figure 6.2.1. Fault traces in the MER and adjecent areas (compiled by Giday, W. G, et al, 1991, after Mohr, 1980). Major boarder faults indicated by letters (A, B, C and D) are where steep escarpments expose thick sequences of Oligocene basalt against which Miocene and Pliocene volcanic rocks are banked.

Rift. It is notable that the Wonji fault belt is hugging the eastern side of the rift in the lake Ziway region.

The floor of the Main Ethiopian Rift is marked by a persistent belt of intense, fresh faulting which has been termed the Wonji fault belt (Mohr 1960). The faults are short and of normal type, and are notably associated with tensional fissures first recognized by Gibson (1967b) from the Fantale region. The Wonji Fault belt is frequently, but not always, axial to the rift and is dextrally displaced along the same cross - rift lineaments which displaced the rift margins (Mohr 1967). The Wonji fault belt is also the line along which recent lavas and ignimbrites have erupted, and the whole volcano-tectonic association is one suggestive of crustal tension acting across the rift (Mohr 1967a).

Paul Mohr in his 1967 work discussed that, the Wonji fault belt in the lake Langano and Ziway region lies against the eastern margin of the rift. From the western margin of the Shala caldera, and ultimately in continuous alignment with the Wonji fault belt north of Lake Abayata, there extends northwards a median zone of faulting with which some explosion craters are associated. This median rift-faulting is predominantly upthrown east along extensive, linear faults of a type more typical of the rift margins.

From the eastern shore of lake Ziway to the Awash river at Wonji, the Wonji fault belt is intensely developed. It

forms a NNE-SSW belt about 15 kms across (Mohr 1967) and is marked by numerous basaltic cinder cones and older silicic cones and calderas. The direction of upthrow of the fault is again variable but is more commonly to the west, and again associated with tensional features (see fig.6.2.2b). The most intense part of the belt is dextrally displaced at Asela by about 13kms (Mohr 1967), at the same altitude as Chilalo-Guraghe cross rift lineament.

6.2.2. Structural Mapping and interpretation

The super synoptic view provided by satellite images is ideal for re-evaluating fault patterns and other reflections or britle tectonics over large areas. Small, regionally insignificant features are suppressed and very large, subtle and previously unsuspected ones may show up. Figure 6.2.2a is interpreted from MSS band 7 at scale of 1:500,000. The lineament map shows the spatial geometricl relations between the marginal and the rift floor normal and strike slip faults. However, in the map almost all minor lineaments less than the resolution of the system (79m) are not detected and mapped. The smaller the scale is, the more subtle, more completely connected and larger are features that can be discerned. Using the image four sets of structures are identified; 1. NE-SW marginal faults, 2. E-W oriented strike slip faults, 3. NW-SE striking younger strike slip faults and 4. NNE-SSW and N-S sriking youngest normal faults.

Fig.6.2.2a

LINEAMENT MAP ACROSS THE MER BETWEEN
N7°55' N8°30'
INTERPRETED FROM LANDSAT MSS BAND 7
IMAGE

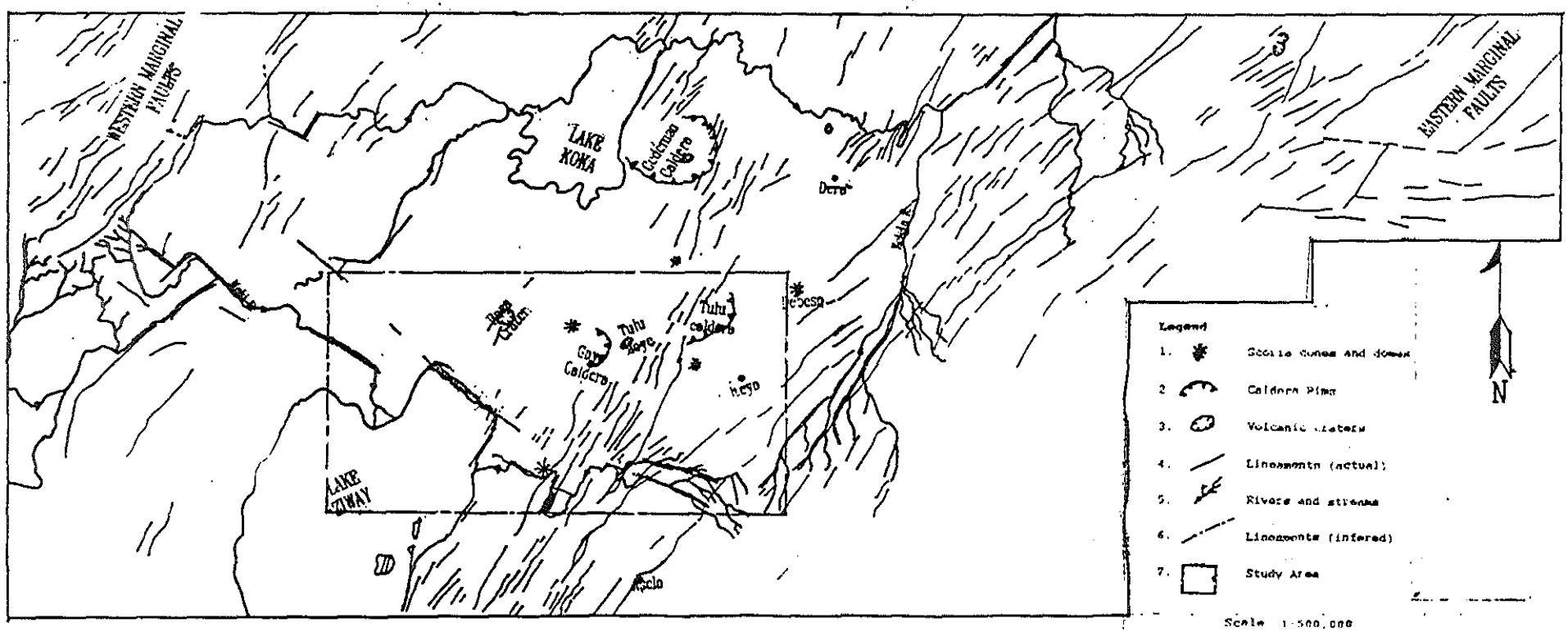

The photo-interpretation of fault is often more reliable than their detection in the field. Because they are usually weaknesses, fault surfaces are rarely seen at outcrop. They often control low lying features, from which views into the distance are difficult. Changes in vegetation and surface texture related to faults are difficult to see at close range. The synoptic view of photographs enables widely separated pieces evidence to be linked as sharp and semi-contineous linear features or lineaments. The vertical exaggeration associated with stereoscopic viewing accentuates even the most subdued topographic features, and reveals clearly any vertical displacement associated with the faulting.

The graben and horst structures in the area are therefore, carefully mapped from photo-interpretation supported by field survey to the scale of 1:50,000. In the northeastern and eastern part of the study area which is highly affected by Wonji fault belt, the rift-in-rift structure (graben-horst) systems run for tens of kilometers parallel to each other (see fig.6.2.2b). For the reason mentioned in section 6.2.1, the lineaments (faults and associated tensional fissures) are concentrated in the eastern part of the area closer to the main eastern escarpment of the Rift Valley.

Step faults in the area are conspicuous on photographs

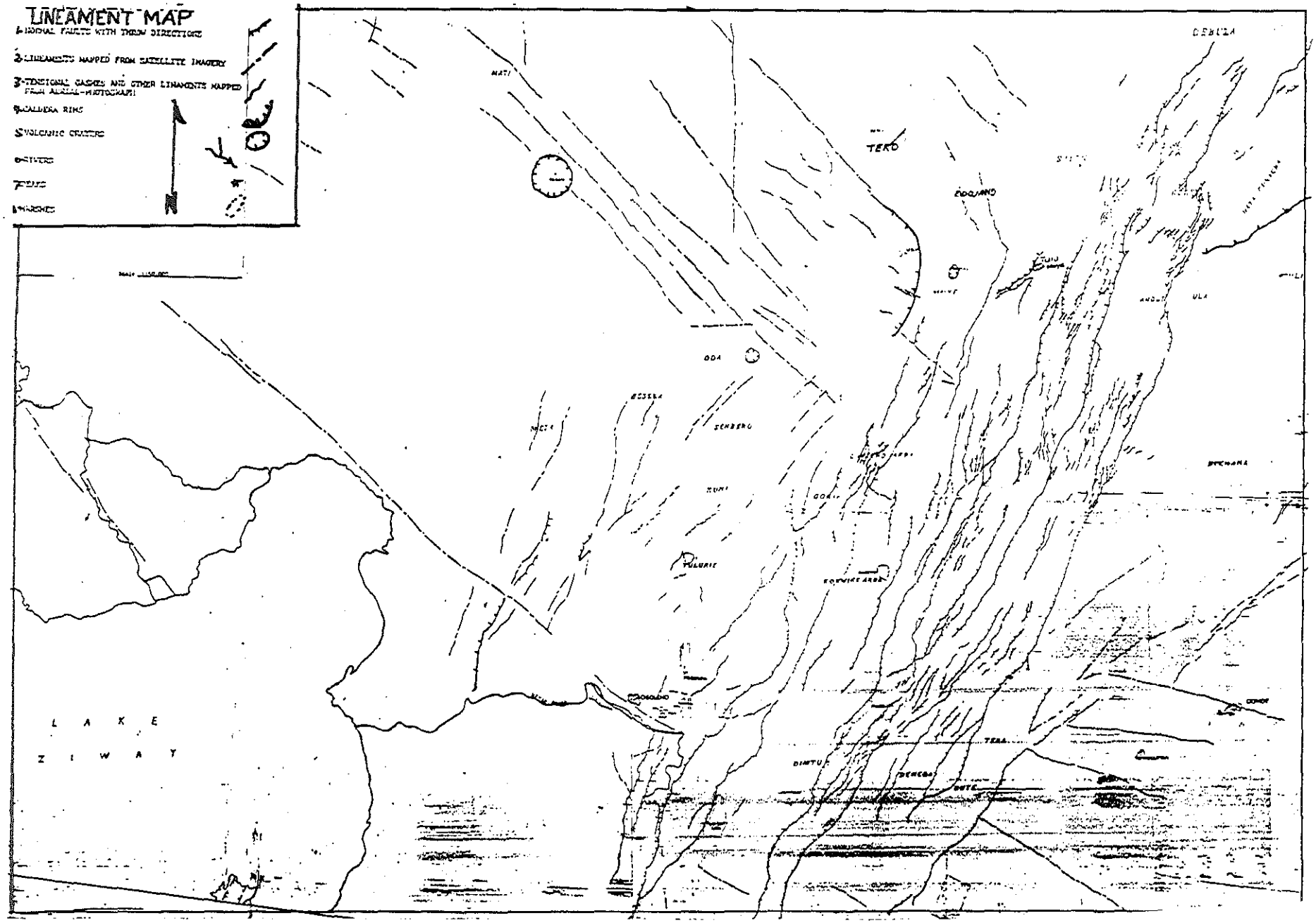
LINEAMENT MAP
1-NORMAL FAULTS WITH THROW DIRECTIONS
2-LINEAMENTS MAPPED FROM SATELLITE IMAGERY
3-TENSIONAL CRACKS AND OTHER LINEAMENTS MAPPED FROM AERIAL-PHOTOGRAPH
4-CALDERA RIMS
5-VOLCANIC CRATERS
6-RIVERS
7-ROADS
8-TOWNS
L A K E
Z I W A Y
TERO
ODA
BOSSA
SENBERO
ZUWAI
FULURIA
DIMTU
TERA
DEBRA

because of their near-independence of valleys, ridges and uplands. The steeper they are, the more they resemble regular lines on photos. The eastern escarpment is formed by steps of faulted and rotated blocks. The rotation is observed both during aerial- photo interpretation, and field mapping from dip and slope mesurements of the faulted blocks. Figure 6.2.2c shows profile section in which graben and horsts, normal step faults and blocks rotation are evidenced. Where faults juxtaposes rocks of grossely different resistance to erosion, the fault can be expressed as a line of cliffs, waterfalls (like that of Kulumsa) or abrupt changes in slope.

The younger faults do not continue straight throughout the area. They die out, because the strain being taken up along other faults found closer to them and form an en echlon arrangement. They were being splited and developed sply faults along their length. In the study area such fault systems are located near Anole vilage, southwest of Tulu caldera and along the Shorima main fault scarp at Gallo. These sply faults result from the reorientation of principal stress axes in close proximity of the major faults (see fig.6.2.2d). In turn, large sply faults have a similar but less widely distributed effects, and develop minor sply of their own. The result is a complex pattern of curved faults and tectonic joints of different sizes.

The oldest faults in the area are found northwest of Asela town and their strike (NE) is persistently similar to the eastern marginal faults found on the plateau. They are younger than Chilalo volcanism because they cut across Chilalo basalts and trachytes forming steep fault scarps. The major scarp formed by these faults is found across river Kulumsa forming fall of more than 50 m. high. The other scarps of these faults either die out or buried under the thick pyroclastic deposit covering the field bounded by Iteya, Kulumsa and Huruta. Only flexure like ridges exist in morphological continuity with these NE striking older faults (see fig. 6.2.2e). Further south in the study area, the marginal faults propagate as steps displayed in an en echelon style with down thrown west side.

The structural control on the courses of the rivers that start from NE side of the Mt. Chilalo gives evidences for the presence of NW-SE and E-W faults younger than marginal faults and older than the Wonji fault belt.

The courses of rivers Boru, Wedecha and Keleta more or less follow the NE trending marginal fault systems, while that of Shorima, Gonde and Kulumsa rivers, starting from a similar locality are controlled by NNW to NW trending strike slip faults. This spatial relation can be observed on MSS band 7 "12JAN73 C N08-35/E039-50N N08-33/E039-54" (fig.6.2.2a) black and white image. Mayer et al. (1975) and

Mohr (1967) indicated the presence of dextral strike slip fault older than Wonji Fault belt at about the latitude of Asela.

Among the most important outputs of the approach in this study is the ability to reconstruct and map the NW-SE trending strike slip faults in the area from integrated interpretations of aerial photo and satellite images. The synoptic observation of enhanced satellite TM digital data with higher spatial resolution helped in mapping the strike slip faults in two different localities within the study area. One of these faults trends NW-SE along the northern border of lake Ziway, passing through the upper course of the Ketar river after Shatemta marsh, and along the Meki river. Ketar river has changed its course suddenly at Shetemata, following the line of weakness older than the Wonji Fault belt. If this plane of weakness were not present, the river starting from Chilalo would follow the graben further to the north. Therefore, sudden change in the course of the river to the west and the presence of NW to NNW trending minor lineaments mapped from both aerial photo and satellite image over the area suggests the existence of this major strike slip fault.

The strike slip fault is older than the Wonji fault belt because it does not laterally displace any of the fault

scarps formed by the belt.

The other location of the strike slip fault system found in the area is north of Mt. Gorya passing through Mt. Bora. These faults are observed to have similar age relations with the Wonji fault belt like the previously discussed strike slip fault. Its trend is also persistently similar to the southern strike slip fault in the area. Within the study area, south of Tulu Moye, there is also a discordant graben like structure striking NNW and cut by the NNE striking Wonji fault belt. This graben like structure does not continue after the Wonji fault graben system. This means that, the graben forming faults are older than the Wonji faults and probably associated with the tectonism that has produced the southern strike slip fault system. Because, the NNW orientation of the graben and its age relationship with the Wonji fault belt is similar to that of the main strike slip fault cutting across the area and the Wonji Fault Belt.

In general, the geometrical relation between the strike slip faults proposed by this study and the Wonji fault belt is in such a way that, the NNE trending Wonji fault belt starts to biforcate into splay faults and propagates in an en echelon manner within the zones affected by older NNW to NW striking strike slip faults. This structural relation is indicated on the tectonic map of the study area (fig.6.2.2d)

The younger faults are those striking NNE and concordantly intersecting the NE striking faults in the southeastern part of the study area. This angular relation between the NNE striking Wonji fault belt and the NE striking marginal faults was discussed by Mohr (1967b).

These faults are generally NNE to SSW trending, scissor type, normal, step faults with small downthrows (upto 30 m.) to the west as well as to the east. They are mostly curvilinear and show an en echelon style of arrangement.

The faults mainly form rift-in-rift system of structures which result in narrow horsts and grabens that run parallely for tens of kilometeres along the axial trend of the rift. Some of the grabens which are occupied by younger basaltic flows extruded through the fissures have partially turned into swamps and partially being filled by alluvium.

The youngest faults in the area are those cutting pumice domes and scoria cones on the floor of the rift. These faults are found in the axial zone of the rift trending NNE to N-S. They have very small throws but are deep penetrating. Because the youngest basalts and acidic lavas such as rhyolite and obsidian domes have been extruded through these faults. There are also faults cutting through these youngest lavas which are still active. Their activness is suggested by the presence of geysers and recently brecciated lava flows along the faults. It is also possible that there are undetected

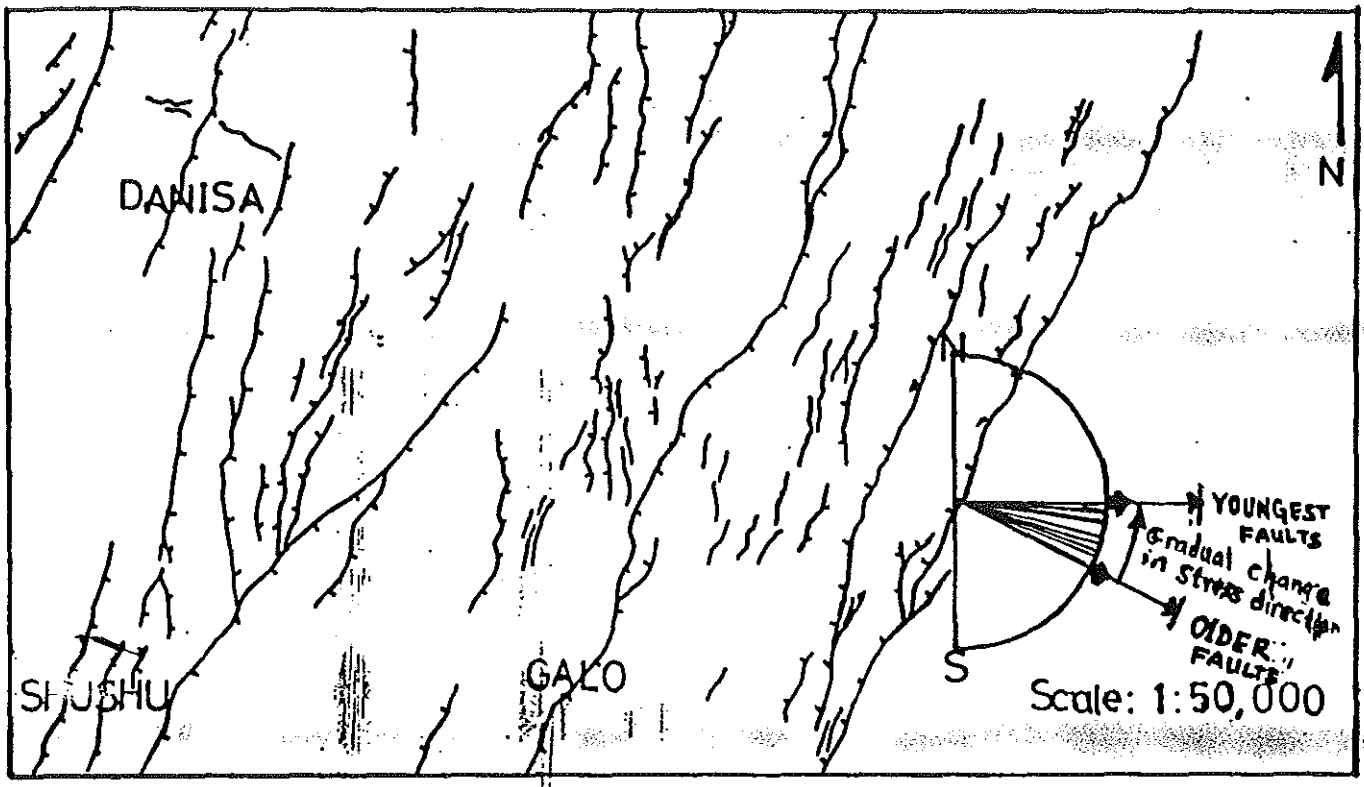

Figure 6.2.2d. Sply faults and the gradual changes in the stress direction.

Figure 6.2.2e. A sketch showing the ridges that are in morphological continuity with the NE - SW striking major normal faults.

faults younger than these. Very few gapping fissures (upto 1m wide) which issued basaltic lavas, or dry openings striking NNE to NE are also present within the area. They show no vertical displacement and resulted from intensive tensioning associated to the normal faulting.

7. EVALUATION OF THE LANDSAT TM DIGITAL IMAGE AND ITS CONTRIBUTION IN LITHOLOGIC AND STRUCTURAL MAPPING.

7.1. Comparison with some of the Previous Works.

The study area is located in the central part of the Main Ethipoan Rift which undoubtedly, has great scientific value for understanding the evolution of continental rift. However, due to its rough topography and hostile climate the most important localities in the Central and Northern sectors of the Rift Valley are either hardly accessible or totally inaccessible. Therefore, despite of its scientific importance there are very few field data supported published geological works.

Eventhough there are no published geological maps particular to the study area, Ethiopian Ministry of Mines and Energy has published a geological map for the Nazereth Sheet with the scale of 1:250,000 in 1987. The geological map of the Nazreth Sheet includes more than 80% of the study area.

According to the reliability map indicated on the geological map of Nazereth Sheet more than 70% of the geological mapping were made only from aerial-photographs interpretation. However, the spatial resolution of the aerial-photographs is the highest, poor radiometric resolution and narrow (0.4 - 0.9um) spectral range limits its potential for detailed lithologic mapping. The reflectance data collected in the reflected infrared region of electromagnetic spectrum (1.1 - 2.35 um) which are mostly usefull for discriminating rock types, tracing variations within and diferences among lavas from the same source. Since aerial-photos do not extend beyond 0.9 um limit they luck such informations as variation tracing and rock discrimination, and the capability of further digital enhancement. Therefore, the accuracy of a map compiled from interpretation of aerial-photographs is highly limited by the accuracy and reliability of aerial - phtographs.

Even though the scale of the map prepared during this study is five times greater than the Nazreth Sheet geological map, larger geologic features which are mappable in both scales were taken for comparison. The features are: 1. Lithologic contacts, 2. Variations within rock bodies and 3. Lineaments.

1. Lithologic Contacts:

In the Nazereth sheet geological map most of the lithologic bounderies mappable at the scale of the map were not precisely mapped. Mainly the trachytic domes at Tirbocha and the obsidian domes at Jano which are completely different in composition were mapped as one and same rock types. In the section for image analyzing, (plates 5.2a, 5.2b, 5.2d and 5.2e) the compositional differences between the obsidian domes (C2) and the trachytic domes (C6) is displayed by the colour differences The obsidian ridge that has connected the two main obsidian domes in the north central part of the study area and the pumice domes and flows at Tulu Moye were also partly mapped as feldspar basalts of Tulu Moye (Di Paola,1978). Some of the pyroclastic falls and alluvial deposits found in the grabens located in the southeastern part of the area were partly mapped as basalt.

2. Tracing Lithologic Variations:

In the grabens found at the southeastern part of the area, some of the pyroclastic falls and alluvial deposits were partly mapped as basalt. The scoriaceous alkali basalt which is the youngest basaltic flow in the area, is further subdivided into two groups based on the amount of phenocrysts, composition, texture and structure. In fact, some of these parameters highly control the reflectance of

the basalt which is obiously sensed by Sensors mounted on Satellites. Therefore, the two subclasses of the scoriaceous alkali basalt are clearly outlined on the Satellite map prepared during this study. In the previous works the basalt was mapped as a homogeneous rock body found in the form of patches of lava flow.

3. Lineament Mapping:

Regarding the structural mapping , the possibility of stretching and filtering using both directional and non-directional filters the digital data (image) has revealed most of the NW and E-W striking geologic structures. These set of structures were not mapped neither in the geological map of Nazreth sheet published in 1978 by the Ethiopian Ministry of Mines and Energy (fig. 7.1) nor in fault trace map compiled by Weldegabriel, et al, 1991, (fig.6.2.1). Especially, the NNE-SSW and N-S striking discernible faults cutting Tulu Moye crater and the obsidian dome at Gnyaro (see figure 7.1) were not mapped in the Nazreth sheet geological map. But using the digital data (see figure 5.2g. The filtered black and white image) and aerial-photo interpretation these faults are pinpointed with their known throw directions.

GEOLOGICAL MAP OF THE AREA WEST OF ITEYA - GONDE ROAD
EXTRACTED FROM NAZRET SHEET GEOLOGICAL MAP 1978.

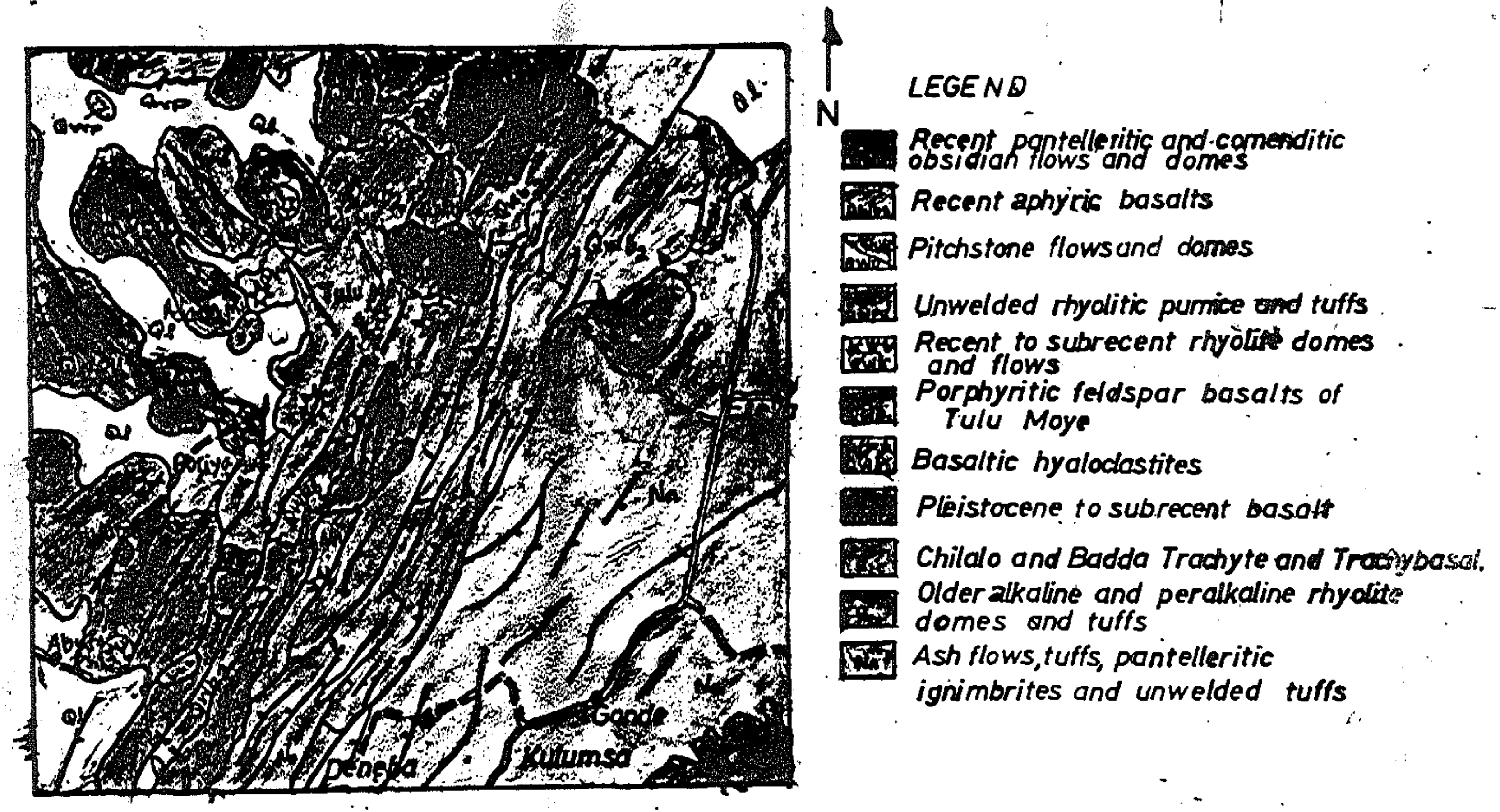

Scale: 1:250,000

8. CONCLUSION

Remote Sensing is the science of gathering information describing distant objects or scenes targets that could not be studied at closer distance. Instruments such as scanners, radars and aerial photo cameras help to collect spectral data for geological, landuse landcover, geomorphological studies and locate hydrothermally active areas which are for some reasons inaccessible or hazardeous.

Sensors also extend the range of human perception from visible light to include most of the spectrum of electromagnetic energy as well as magnetic, gravitational and particle radiation fields. Not only does this permit the geologist to infer the composition of surface materials (from absorption bands in infrared radiation reflected from the surface), but enables them to determine some bulk or body properties, for example, thermal conductivity.

In this study, the lithologies and structures found in the area located within the relatively inaccessible part of the Main Ethiopian Rift is mapped using method of Remote Sensing.

To come up with the final result different types of image enhancement techniques have been applied, out of which principal component analysis, band-ratioing, filtering,

streching, false colour combining and applying some of the GIS programs are the common ones. Principal component and band ratio false colour composite images are found to be most informative for lithologic mapping. The different types of basalts outcroping in the area and variations in texture, structure and composition are traced and carefully mapped using integrated results of Remote Sensing and Conventional methods. Unclassified false colour composites of the original TM bands (Plates 5.2a and 5.2b) and enhanced bands (Plates 5.2c and 5.2d) give most of the evidences for mapping the geology and associated landforms.

TM band 5, principal component-1 and band ratio derived from (band 5 - band 3) / (band 5 + band 3) combined in R G B order is chosen for supervised classification and the classified image is georeferenced and further simplified to the geological map of the area. Supervised classification gave restricted number of classes which do not correspond to the number of lithologic groups found in the area. Seven lithologic classes were established and during field checking all types of rocks grouped under each class were investigated and reclassified into nine stratigraphically significant rock types. The results of field observation and laboratory investigation is summarized in Table 8a. By filtering the TM band-5 digital data using non-directional (7

x 7) both high - pass and low - pass Laplacian filters, all lineaments found in the area were enhanced and mapped. From the interpretation of Landsat MSS band-7 analog image supported by field observations also four sets of extensional structures are mapped. These are: 1. rift margin NE-SW striking normal faults, 2. E-W striking dextral strike - slip faults, 3. NNW-SSE strike slip faults and 4. NNE-SSW to N-S striking youngest faults. The NNW-SSE trending lineaments and some of the youngest N-S striking normal faults identified during this study were not shown in published geological and tectonic maps of the region.

Eventhough lithologic mapping only from satellite imagery has certain drawbacks and inconviniences, integreted Conventional and Remote Sensing methods constitute one of the most powerful and efficient technique in identifying different lithologies, outlining their contacts and delineating regional lineaments that can not be detected by detailed field mapping. For reconaissance mapping of the inaccessible regions in Ethiopia where rocks are well exposed the method of Remote Sensing is utmost importance and in this work it has been shown that geological maps of large areas can be prepared at a scale larger than 1:100,000 in shorter time, minimum expence and better accuracy.

Regarding the volcano - tectonic history much has been said about the evolution of the Rift Valley, the time and

geochemical relation between magmatism and tectonism in the Rift.

The recent geochemical and geochronological data supported detailed work by Weldegabriel, G., et al. (1991) is found to be convincing. In the paper it is stated that, during the inital stages of volcanism and rifting, lithospheric melting predominated, and crustal contamination was significant and led to the generation of transitional basalt with more alkalic character. With time, depleted asthenospheric mantle became an important component, initially as an end member in mantle mixing, and eventually as the dominant mantle reservoir in more attenuated areas (for example the axial zone of MER, Afar) and led to a more tholeiitic transitional basalts (Hart and Others, 1989).

In the northern sector of the MER, Kazmin and Others, (1980) argue that the most definitive evidences as to when rifting began is provided by peralkaline silicic rocks of Nazreth group ($\lesssim$ 9 m.y. old) and volcaniclastic deposits (Miocene) that are present on the rift floor banked against the eastern boarder faults. This demonstrates that the rift margin had formed prior to their eruption and deposition, respectively;

Table 8a. Summary of Volcanic Units of the Study area with TM imagery Characterstics

Spectral class	Representative Lithology for the Class	Petrography		Field Characterstics	TM Imagery Relationships		
		Associated Rock Type	Major Minerals		Dark	Indistinct	Bright
Class-1	Scoriaceous Basalt	Evolved Basalt	-Corroded Plagioclase Phenocrysts	-Scoriaceous (aa-lava) and brown to dark brown in colour, found as sheets of flow or dome like upwellings	T3 B5 PC1	PC2 PC3	PC4 VI
Class-2	Obsidian	-Banded Obsidian -Altered Pumiceous Obsidian (glass) -Pitchstone and perlite -Massive Obsidian	-Phenocrysts of Quartz segregated in certain zones -No mineral observable -No mineral observable	-Banded and layered -Low specific gravity with pumiceous texture at the top and lighter yellowish in colour -Black and massive (without typical textures or structures)	T3 B5 PC1	PC3 PC4	VI PC2
Class-3	Scoriaceous Por. Basalt	-Evolved Basalt with plagioclase phenocrysts	-Corroded plagioclase and few mafic minerals as phenocrysts, microlaths of feldspar in glassy groundmass	-It shows well preserved flow structures with ropy surface and rolled edges, dark to dark brown in colour	T3	B5 PC1 PC3	PC4 PC2 VI
Class-4	Pumice and Ash Group-I	-Tuffs -Pumice Domes -Pumiceous Ignimbrite -Tuff Cones -Pumice and Ash Flows and Falls	-Some free crystals of quartz and alkali feldspars	-As pyroclastic falls and flows with light grey and yellowish colours -As tuff cones and rings, and domes forming continuous ridges	PC3 T3	PC4 PC2	B5 VI PC1
Class-5	Porhpyritic Alkali Basalt	-Porphyritic Scoriaceous Basalt -Few Trachytic Rocks	-Phenocrysts of plagioclase and few titano-augite, olivine and rutile needls in the groundmass -Phenocrysts of plagioclase and few mafic minerals	-Pahoehoe lava flow with bigger plagioclase phenocrysts and few vesicles	T3	B5 VI PC1	PC2 PC3 PC4

Class-6	Trachyte	-Trachytic rocks	-Plagioclase and alkali feldspars, quartz and magnetite as phenocrysts	-As mushroom-shaped lava domes and sheets of flows	T3 PC3	PC2 B5 PC4	VI PC1
		-Ignimbrite	-Alkali feldspars (orthoclase and anorthoclase) and quartz	-Characterized by the presence of fiamme and collapsed pumice fragments			
		-Rhyolite	-Quartz, Chalcedony and very few alkali feldspars in the devetrfied groundmass	-Characterized by flow banding and microfolding in the bands			
Class-7	Pumice and Ash Group-II	-All pumice and ashes that have been converted to soil -Highly weathered tuffs and ignimbrites -Alluvial deposites and soils of different origin	-All are characterized by the presence of free crystals of quartz and alkali feldspars	-Are mainly cultivated and bellow the soil horizon altered ash and pumice fall layers are common -Crystals of secondary carbonates and free crystals of quartz and alkali feldspars are also common	T3	B5 PC2 PC4 PC3	VI PC1

Note: PC1 - Principal component one
PC2 ,, ,, ,, two
PC3 ,, ,, ,, three
PC4 ,, ,, Four

T3 -Texture image derived from band 3 by applying 3 x 3 box-car
VI -Veggetation index derved from band 5 and 3
B5 -TM band five

Continous attenuation of the lithospheric crust in the northern sector is demonstrated by the change of transitional basalt to a more tholeiitic character with time (Barberi and Varet, 1977; Brotzu and others, 1980b).

The different stages of the volcano-tectonic events which took place in the area, can be roughly summarized as follows.

1. Pyroclastic rocks of the plateau are extruded from the first plateau fissures and calderas.
2. The marginal escarpment came into being by a major phase of NE-SW faulting, which exposed the escarpment pyroclastics.
3. Strike - slip (dextral) E-W to NW faulting that has displaced marginal faults.
4. Eruption of Tulu volcano spreading its pyroclastic products on top of the escarpment pyroclastics with prior development of paleosol in between.
5. Outpouring of basaltic lavas through fissures older than the Wonji fault belt. They unconformably overly the Tulu pyroclastics.

   Second phase of cross - rift faulting with NNW-SSE direction.
6. Third major phase of faulting (WFB) forming narrow

rift-in-rift structures within the rift.

7. Extrusion of younger evolved basaltic, rhyolitic, trachyitic and obsidian flows and domes through the deep penetrating fractures and faults of Wonji trend.
8. The youngest phase of faulting that has cut through those younger lava that have been extruded through the fractures associated to Wonji fault belt.

General migration of volcano-tectonic activity from rift margin towards the central zone of the rift is observed. It is indicated by the subparallel belts of step faults and rock units of decreasing ages in this direction. The stratigraphic relation among the structures and rocks suggests that the youngest tectonism and volcanism is found at the axial zone of the MER. The decrease in the age of volcanics towards the rift axial fault belt has been shown for the Afar and MER by Zanettin and Justin-Visentin (1975), but Giday et al (1990) did not find evidences that volcanism has migrated from the plateaus towards the central sector of the Main Ethiopan Rift.

9. REFRENCES

1. Adams, J. B., and others, 1982, Interpretation of weathered surfaces in arid regions using Landsat Multispectral Images; Thematic conference: Remote

Sensing of Arid and Semi-Arid lands: Cairo, Egypt.

2. Mengistu, A., 1975, Grassland condition in Chilalo Awraja. CADU publication No. 112, Asela, 107p.

3. Alexander, F. H. Goetz and Lawrence C. Rowan, 1981, Geologic Remote Sensing. Science Vol. 211, No. 20 February 1981.

4. Bahat, D., 1979, On the African Rift System, theoretical and expermental study. Earth Planetary Sci. Jour. Vol. 45, No. 2.

5. Abebe, B., 1982, The influence of geology and other related soil forming factors on the inherent, fertility of soil in the Asela area, MSc. thesis paper, 131p, February 1982.

6. Berhe, S. M. and Rothary, D. A., 1986, Interactive processing of Satellite images for structural and lithologic mapping in Northeast Africa. Geol. Mag. Vol. 123, No. 4, pp 393 - 403.

7. Berhe, S. M., 1988, A regional tectonic study of NE and E Africa and its implication for mineral exploration: A synoptic view of Satellite Imagery. Proceedings of IGARSS'88 symposium, Edinbourgh, Scotland, 13 - 16 sept.

8. Bizouard, H., Barberi, F. and Varet, J., 1980, Mineralogy and petrology of Erta Ale Boina volcanic series.

Afar Rift, Ethiopia. Jour. Petr. No. 2.

9. Black, R., Morton, W. H. and Varet, J., 1972, New data on Afar tectonics. Nature, physical science, Vol. 240, No. 104, pp 170 - 173.

10. Bocco, G., 1990, Gully erosion analysis using Remote Sensing and GIS. PhD. diss, University of Amesterdam.

11. Bocco, G., J. LPalacio and C. R Valenzula, 1989, Geomorphological mapping using SPOT for gully erosion assessment. Proceedings 11th geomorphological cong, Frankfurt.

12. Bocco, G., Palacio, J. and Valenzuela, C. R., 1991, Gully erosion modelling using GIS and geomorphologic knowledge. ITC Journal 1990 - 3, pp. 253 - 261.

13. Browning, P. and Smewing, J. S., 1981, Processes in magma chambers beneath spreading axes: evidence from magmatic associations in the Oman Ophiolite. Jour. of Geol. Soci., London, Vol. 138, pp 279 - 280.

14. Burrough, P. A., 1986, Principles of Geographical Information Systems for land resources assessment. Claredon press, Oxford.

15. Canas, A. A. D. and Barnett, M. E., 1985, The generation and interpretation of false colour composite principal component images. International journal of Remote Sensing, Vol. 6, pp 867 - 881.

16. Di Paola, G. M., 1972, Geology of Corbetti caldera (Main Ethiopian Rift). Bull. Volc. T35, No. 2.

17. Di Paola, G. M.,1976, Geological map of Tulu Moje area.

18. Drury, S. A., 1987, Image interpretation in geology; digital processing of images in the vissible and near-infrared, pp. 118 - 147.

19. Engel, J. L., and Weinstein, O., 1982, The thematic Mapper - An overview, In International Geoscience and Remote Sensing symposium, Munich 1982, Digest: Institute of Electrical and Electronics Engineers, Vol. 1, PWP 1.1 - 1.7.

20. Folyd, F. Sabins, 1982, Remote Sensing principles and interpretation; Plate tectonic interpretation of Afar Triangle, Ethiopia, pp. 112 - 116.

21. Gibson, I. L., 1967, Preliminary account of the volcanic geology of the Fant - Ale (Shoa). Bull. Geophys. Obs., Addis Ababa, No. 10.

22. Gibson, I. L.,1970, Quaternary pantelleritic volcanism in the Main Ethiopian Rift. Fourteenth annual report of the Research Institute of African Geology, University of Leeds, Department of Earth Science.

23. Greganian, A., Piccirillo, E .M. and Alebachew Endeshaw, 1973, The subdivision of Volcanic Series in the Ethiopian plteau: New geologic interpretation of the

Dessie-Kombolcha area. Bull. Soc. Geo. It. 22.

24. Goetz, A. F. H. and Rowan, L. C, 1981, Geologic Remote Sensing. Science, Vol. 211, pp. 781 - 791.

25. Goetz, A. F. H., Billingsely, F. C., Gillepsie, A.R, Abrams, M. J., Squires, R.L, Shoemaker, E. M., Lucchitta, I., and Elston, D. P., 1975, Application of ERTS Image and Image Processing to Regional Geologic Problems and Geographic mapping in Northern Arizona. JPL Tech. Rept. 32 - 1597, California Inst. of Tech., Pasadena, California, 188p.

26. Goetz, A. F. H, Wellman , J. B. and Barnes, W. L., 1985, Optical remote sensing of the earth, in Institute of Electrical and Electrnics Engineers, Proceedings, Special issue on Earth's Resource from space: New York, Vol.73, pp. 950-969.

27. Ingebritson, S. E and Lyon, R. J. P., 1985, Principal Components Analysis of Multispectral Image Paris. Int. J. Remote sensing, 1985, Vol. 6, No.5, pp. 687 - 696.

28. Joseph, H., Myers and Raloh Bernstein, 1985, Image Processing on the IBM Personal Computer. Proceeding's of the IEEE, Vol. 78, No. 6, June 1985.

29. Kazmin V. and Seifemichael Brehe, 1978, Geology and development of the Nazareth area, Northern Ethiopia Rift, EIGS, Note No. 100, 26p.

30. Kuno, H., 1953, Formation of Calderas, Amer. Geophys. Union, 34, No. 2, pp. 267 - 280.

31. Kunz. K., Kruzer H. and Miller, p., 1975, Potassium Argon age determinations of the Trap Basalt of South-Eastern part of Afar. In: Pilger, A. and Rosler, A. (editors),Afar Depression of Ethiopia, Schwizerbart, Stuttgart, pp 370 -394.

32. Mayer, W., Pilger, A.,Rosler, A. and Stets, J., 1975, Tectonic evolution of the Northern part of the Main Ethiopian Rift in Southern Ethiopia. In: Pilger, A. and Rosler, A. (editors) Afar Depression of Ethiopia. Schweizerbat Stuttgart, pp 352 - 362.

33. MC Donald, R. and Gibson, I. L., 1969, Pantelleretic obsidian from the Volcanic Chabbi (Ethiopia) Contr. Mineral and Petrol. 24.

34. Meijerink, J. L. 1988, Data acquisition and data capture through terrain mapping units. ITC Journal 1988-1, pp 23-44.

35. Miller, J.A. and Mohr, P.A., 1966, Age of the Wachacha Trachyte-carbontite Volcanic center. Bull. Geophys. Obs. Addis Ababa, 9.

36. Mohr, P. A., 1962, The Geology of Ethiopa, Univ. Coll. Addis Ababa Press, Addis Ababa, 26p.

37. Mohr, P. A., 1963, The Ethiopian Cainozoic lavas- a

preliminary study of some trends: Sptial, temporal, and chemical. Bull. Geophys. Obs. Addis Ababa, 3, No. 2, pp 103 -144.

38. Mohr, P. A., 1970, Volcanic composition in relation to tectonics in the Ethiopian Rift system- a preliminary investigation in. Bull. Volc. T34, pp 141-157.

39. Mohr. P. A., 1967, The Ethiopian Rift system, Bull. Geophys. Obs. No. 11, Addis Ababa.

40. Morbidelli, L. and Piccirillo, E. M., 1973, Tectonics and Volcanism in the Main Ethiopian Rift (Preliminary report). Bull .Soc. Geol. It. 92, pp 273 - 286.

41. Morbidelli, L. and Nicolotti, M., Petrucianni,C. and Piccirillo, E.M., 1975, Ethiopian South-Eastern plateau and related escarpment: K/Ar Ages of Main Volcanic events (Main Etiopian Rift from 8o10' to 9o00' lat. North), Afar Depression of Ethiopia. Schweizerbart, Stuttgart.

42. Morgan, W. J., 1971, Convection plums in the lower mantle nature, 230, pp 42 -43.

43. Podwysocki, M ., Gunther, F., Blodgett , A., 1977, discrimination of rock and soil types by digital analysis of Landsat data, Goddard Space Flight Center, Document 923-77-17, Greenbelt, Maryland, 37p.

44. Rothery, D. A. 1982, The Evolution of the Wugbah Block and the applications of remote sensing in the Oman Ophiolite. Phd. thesis, Open University.

45. Rothery, D. A. 1983a, Supervised maximum-likelihood classification and post classification filtering using MSS imagery for lithological mapping in the Oman Ophiolite . In. Proceedings, International Symposium on Rmote Sensing of Environment, 2nd Thematic Conference, Remote Sensing for Eploration Geology . Fort Worth, Texas, 1982, Vol. 1, pp 417 - 426.

46. Rothery, D. A. 1984a, The role of Landsat Multispectral Scanner (MSS) imagery in mapping the Oman Ophiolite. In: Gass, I. G., Lippard, S. J. and Shelton, A. W. (eds) Ophiolites and oceanic lithosphere. Special puplicaton of Geological Society, London, Vol. 13, pp. 405 - 413.

47. Rowan, L. C., Wetlafur, P. W. Goetz, A. F. H., and Stewart, J. H., 1975, Discrimination of rock types and detecton of hydrothermally alterd areas in South-Central Nevada by use of computer-enhanced ERTS images: U.S Geological Survey Proessional paper 883, 35p.

48. Sheffield, C. 1985, Selecting band Combinations from

Multispectraldata, Photogrammetric Engineering and Remote sensing, Vol. 51, pp 681 - 687.

49. Siegal, B.S., and Abrams, M., 1976, Geologic Mapping using Landsat Data. Photogrametric Eng. and Remote Sensing, Vol. 42, No 3, pp 325 - 337.

50. Slatar, P. N., 1980 Remote Sensing- Optics and Optical systems. Reading, MA: Addison - Wesley, 1980.

51. Sultan, M., Arvidson, R., and Struchio, N. C., 1986a, Digital Mapping of opiolite melange zones from Landsat Thematic Mapper (TM) data in arid areas: Meatig dome, Egypt: Geological Society of America Abstracts with programs, Vol. 18 pp. 766

52. Verstappen, H. T, 1989, Satellite remote sensing, geomorphological survey and natural hazard zoning. Some new developments at ITC, The Nethrlands. Suppl Georg. Fis Dinam Quat. 2, pp 103 - 109.

53. Vlodavetz, V. I., 1970, On the terms "Ignimbrite" and "Ignimbritic Deposits" Bull. Vol. T-29, pp 141 - 145.

54. Walsh, S. J., Light and Butler, 1987, Recognition and assessment of error in Geographic information systems. Photogr Eng and Rem. Sens. 53 (10) ,pp 1423 - 1430.

55. Welch, R. Jordan, T. R. and Ehlers, M, 1985, Comparative evaluations of the geodetic accuracy and

cartographic potential of Landsat-4 and Landsat-5 thematic image data. Photogrametric Engineering and Remote Sensing, Vol. 51, No. 9, september 1985, pp. 1249 - 1262.

56. Weldegabriel, G., James, L., Aronson and Robert C. Walter, 1990, Geology, Geochronology, and rift basin development in the central sector of the Main Ethiopian Rift. Geol. Soc. of America Bull., Vol. 102, pp. 439 - 458, April 1990.

57. Zanettin, B., Gregnanin, A., Justin - Visentin, E., Mezzacasa, G. and Piccirillo, E. M., 1974, Petrochemistry of the volcanic series of the central eastern Ethiopian plateau and relationships between tectonics and magmatology; Men. Ist. Min . Univ. Padova, 31, pp. 1 - 35.